# Performance Studies of the Digital Pixel Calorimeter Prototype EPICAL-2

Master Thesis submitted on March 04, 2024 by **Johannes Keul** 

Institut für Kernphysik Goethe-Universität Frankfurt am Main

Supervisor and first assessor: Prof. Dr. Henner Büsching

Second assessor: Prof. Dr. Christoph Blume

# Contents

| In | Introduction |                    |  |    |  |  |  |  |  |
|----|--------------|--------------------|--|----|--|--|--|--|--|
| 1  | Par          | ticle d            | etection with calorimeters                       | 5  |  |  |  |  |  |
|    | 1.1          | Intera             | ction of particles with matter                   | 5  |  |  |  |  |  |
|    |              | 1.1.1              | Electromagnetic interactions                     | 5  |  |  |  |  |  |
|    |              | 1.1.2              | Hadronic interactions                            | 10 |  |  |  |  |  |
|    | 1.2          | Electr             | omagnetic calorimeters                           | 11 |  |  |  |  |  |
|    | 1.3          | Semice             | onductor sensors                                 | 13 |  |  |  |  |  |
|    |              | 1.3.1              | Semiconductors                                   | 14 |  |  |  |  |  |
|    |              | 1.3.2              | Silicon pixel sensors                            | 17 |  |  |  |  |  |
|    |              | 1.3.3              | Digital pixel calorimeters                       | 18 |  |  |  |  |  |
| 2  | Exp          | Experimental setup |  |    |  |  |  |  |  |
| 2  | 2.1          | The E              | PICAL-2 calorimeter                              | 19 |  |  |  |  |  |
|    |              | 2.1.1              | Design and coordinate system                     | 19 |  |  |  |  |  |
|    |              | 2.1.2              | Measurement principle                            | 21 |  |  |  |  |  |
|    |              | 2.1.3              | The ALPIDE sensor                                | 21 |  |  |  |  |  |
|    | 2.2          | Test-b             | eam measurements                                 | 23 |  |  |  |  |  |
|    |              | 2.2.1              | EPICAL-2 setup                                   | 23 |  |  |  |  |  |
|    |              | 2.2.2              | DESY   | 24 |  |  |  |  |  |
|    |              | 2.2.3              | CERN-SPS   | 25 |  |  |  |  |  |
| 3  | Sim          | ulatio             | n  | 27 |  |  |  |  |  |
|    | 3.1          | Implei             | mentation of the EPICAL-2 in Allpix <sup>2</sup> | 27 |  |  |  |  |  |
|    | 3.2          | Model              | Modeling the test-beam data                      |    |  |  |  |  |  |
|    |              | 3.2.1              | Influence of $t_{\text{int}}$                    | 33 |  |  |  |  |  |
|    |              | 3.2.2              | Tuning of $t_{\text{int}}$                       | 34 |  |  |  |  |  |
|    | 3.3          | Simula             | ation compared to test-beam data                 | 36 |  |  |  |  |  |
|    |              | 3.3.1              | Cluster size                                     | 36 |  |  |  |  |  |
|    |              | 3.3.2              | Detector response                                | 37 |  |  |  |  |  |
|    |              | 3.3.3              | Energy resolution                                | 38 |  |  |  |  |  |
|    | 3 4          | Simula             | ation of an enlarged EPICAL-2                    | 39 |  |  |  |  |  |

| 4                | Dat   | a analysis   | 41 |  |
|------------------|-------|--|----|--|
|                  | 4.1   | Data sets  | 41 |  |
|                  | 4.2   | Clustering   | 43 |  |
|                  | 4.3   | Corrections  | 43 |  |
|                  |       | 4.3.1 Pixel masking                                    | 43 |  |
|                  |       | 4.3.2 Alignment and inclination                        | 44 |  |
|                  |       | 4.3.3 Calibration                                      | 46 |  |
|                  | 4.4   | Selections   | 47 |  |
|                  |       | 4.4.1 Event selection for DESY data                    | 47 |  |
|                  |       | 4.4.2 Event selection for CERN-SPS data                | 49 |  |
|                  | 4.5   | Run quality analysis                                   | 54 |  |
|                  |       | 4.5.1 Cluster size                                     | 54 |  |
|                  |       | 4.5.2 Detector response                                | 55 |  |
|                  |       | 4.5.3 Longitudinal shower maximum                      | 55 |  |
| 5                | Res   | ılts   | 57 |  |
|                  | 5.1   | Saturation and angular cluster-enlargement             | 57 |  |
|                  | 5.2   | Measure of linearity                                   | 58 |  |
|                  | 5.3   | Back-bias voltage variations                           | 58 |  |
|                  |       | 5.3.1 Average cluster size                             | 59 |  |
|                  |       | 5.3.2 Detector response and linearity                  | 60 |  |
|                  |       | 5.3.3 Energy resolution                                | 62 |  |
|                  | 5.4   | Radial cuts  | 63 |  |
|                  |       | 5.4.1 Outer radial cut                                 | 64 |  |
|                  |       | 5.4.2 Inner radial cut                                 | 68 |  |
|                  | 5.5   | Leakage  | 71 |  |
|                  |       | 5.5.1 Pixel-hit profiles of the EPICAL-2 and EPICAL-2L | 72 |  |
|                  |       | 5.5.2 Average cluster size                             | 75 |  |
|                  |       | 5.5.3 Detector response and linearity                  | 76 |  |
|                  |       | 5.5.4 Energy resolution                                | 78 |  |
| Sı               | ımma  | ary and outlook  | 81 |  |
| $\mathbf{A}_{]}$ | ppen  | dix  | 83 |  |
| Bibliography     |       |  |    |  |
| Δ                | cknov | vledgements  | 90 |  |

## Introduction

Calorimeters are vital components for energy measurements in high-energy physics experiments. Their design has experienced conceptual developments in recent years: Among newer technologies are so-called monolithic active pixel sensors (MAPS), commonly used in high-energy physics experiments for tracking charged particles. The use of MAPS in calorimetry as a novel concept is under current exploration. Such a calorimeter based on MAPS, called a digital pixel calorimeter, has unique features setting it apart from other calorimeter architectures: As an example, the separation of two electromagnetic showers in close proximity and higher position resolution compared to other calorimeter designs. Due to these unique features, the inclusion of fully or partially digital calorimeters in high-energy physics experiments is foreseen. A partially digital calorimeter under current development is the forward calorimeter (FoCal), which is outlined to be operational as part of the ALICE experiment at CERN in 2027. Digital pixel calorimeters have various potential applications even beyond high-energy physics experiments, as in medical applications: In a system for proton computed tomography, digital pixel calorimeters could be implemented for simultaneously measuring the energy and reconstructing the tracks of particles [Alm20]. The wide range of applications and unique characteristics of digital pixel calorimeters foster the need to study the potentials and limits of the technology and to improve its performance.

This thesis focuses on a digital pixel calorimeter prototype named EPICAL-2. The performance of the EPICAL-2 is investigated under three different aspects: the influence of back-bias voltage, radial cuts, and leakage. Test-beam data recorded with the EPICAL-2 at the DESY and CERN-SPS test-beam facilities is analyzed. In addition to the test-beam data, a Monte Carlo simulation of the EPICAL-2 is performed and studied: The EPICAL-2 is implemented in the state-of-the-art pixel detector simulation framework Allpix<sup>2</sup>. Analyses of the simulation allow examining the behavior of digital pixel calorimeters beyond the test-beam measurements with the EPICAL-2. One goal of the studies presented in this thesis is the exploration of methods to improve the performance of the EPICAL-2 via modifications in the hardware (back-bias voltage) and software (radial cuts). A further goal of this work is to gain knowledge about the impact of leakage on the performance of the EPICAL-2.

The first chapter of this thesis introduces physical and technological concepts relevant to digital pixel calorimeters. The second chapter outlines the EPICAL-2 and test-beam fa-

cilities DESY and CERN-SPS. The third chapter presents the implementation and results of the EPICAL-2 simulation in the Allpix<sup>2</sup> framework. The fourth chapter presents the recorded data sets and details essential data analysis steps such as clustering, corrections, selection, and data quality analysis. The fifth chapter presents the results of the three distinct studies of the EPICAL-2's performance, which were carried out in the scope of this thesis.

## Chapter 1

## Particle detection with calorimeters

Particle detectors are an important tool to study particles like high-energy photons, leptons, or hadrons. Particle detectors generate signals from the interaction of particles with matter. Electromagnetic interactions are often exploited for particle detection, e.g., in the energy measurement of photons and electrons or the tracking of charged particles. The energy measurement of hadrons relies on the strong interaction, and the weak interaction is exploited for the measurement of neutrinos. A type of particle detector dedicated to the measurement of a particle's energy is called a calorimeter. This thesis focuses on a so-called digital pixel calorimeter that facilitates sensors based on silicon for the generation of signals.

To introduce the physical processes present and the technology employed in the calorimeter studied in this work, this chapter presents a selection of processes in which particles interact with matter and introduces several characteristics of calorimeter performance. Furthermore, particle detection and calorimetry with semiconductor sensors are discussed.

## 1.1 Interaction of particles with matter

This section presents a selection of electromagnetic and hadronic interaction processes relevant to the measurements analyzed in this thesis.

## 1.1.1 Electromagnetic interactions

The particles participating in electromagnetic interactions are photons and charged particles like electrons, positrons, and certain hadrons.

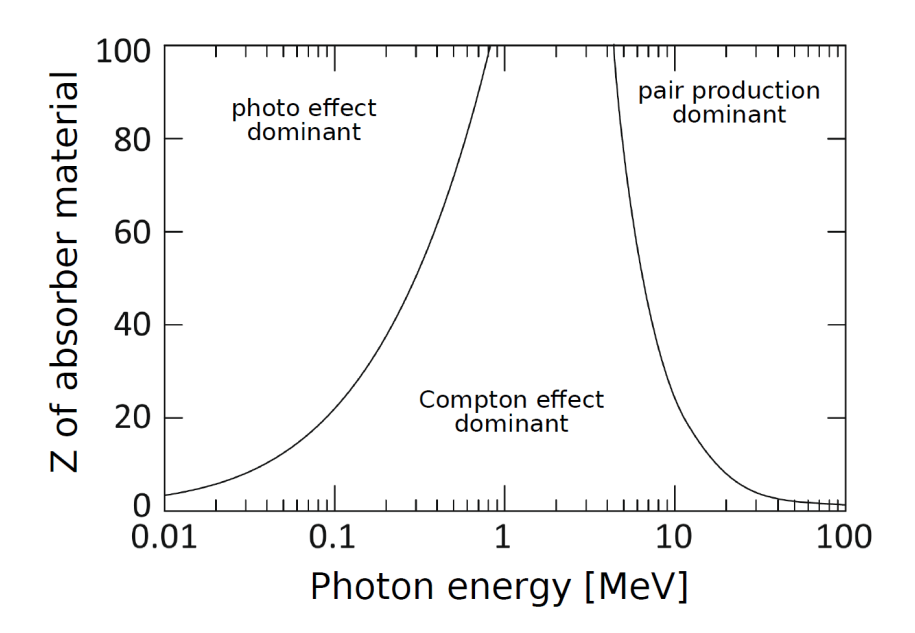


Figure 1.1: Regions on the  $(E_{\gamma}, Z)$  plane in which different photon interaction processes are dominant [Krö21].

### **Photons:**

Amongst the multiple ways a photon can interact with matter, three interactions are particularly important in the context of particle detectors: the photoelectric effect, the Compton scattering, and pair production.

During a photoelectric effect, the participating photon transfers its entire energy to an electron in the shell of an atom. If the energy  $E_{\gamma}$  of the photon is larger than the binding energy  $E_{\rm B}$  of the electron, the transfer of energy results in the emission of the electron with the kinetic energy T, which is referred to as ionization. T is calculated via the following equation [KW20]:

$$T = E_{\gamma} - E_{\rm B} \tag{1.1}$$

During Compton scattering, a photon with the energy  $E_{\gamma}$  is scattered elastically on a free or quasi-free electron in a material. Electrons in an atom's shell are treated as quasi-free when  $E_{\gamma} \gg E_{\rm B}$  applies. The energy  $E'_{\gamma}$  of the photon after the Compton scattering depends on the scattering angle  $\theta_{\gamma}$  and is given by [KW20]:

$$E_{\gamma}' = \frac{E_{\gamma}}{1 + \epsilon \left(1 - \cos \theta_{\gamma}\right)} \tag{1.2}$$

with  $\epsilon = E_{\gamma} / m_{\rm e} c^2$ , where  $m_{\rm e}$  denotes the electron mass and c the speed of light in a vacuum. The kinetic energy T of the emitted electron is given by [KW20]:

$$T = E_{\gamma} - E_{\gamma}' \tag{1.3}$$

The conversion of a photon into an electron e<sup>-</sup> and a positron e<sup>+</sup> in the electric field of a nucleus is referred to as pair production. The photon's energy is converted into

the mass  $2m_e$  and kinetic energy of the generated e<sup>+</sup>-e<sup>-</sup>-pair and kinetic energy of the nucleus. However, the kinetic energy of the nucleus can usually be neglected since the nucleus is much heavier than the e<sup>+</sup> and e<sup>-</sup>. The minimum photon energy required for pair production is calculated as [KW20]:

$$E_{\gamma} > 2m_{\rm e}c^2 = 1.022\,{\rm MeV}$$
 (1.4)

Which of these three interaction processes occurs most likely when a photon traverses a material depends on the charge number Z of the material and on the energy  $E_{\gamma}$  of the photon. Figure 1.1 shows the regions in the  $E_{\gamma}$ -Z-plane in which a certain interaction process of photons with matter occure more likely than other interaction processes. For the measurements presented in this thesis, pair production is the most relevant interaction process of photons with matter.

### Charged particles:

The two largest contributors to the energy loss of charged particles in matter are ionization and bremsstrahlung. Both processes are relevant to the measurements presented in this thesis.

A charged particle traversing a medium will interact with the shell electrons of the atoms in a medium via the Coulomb force. In these interactions, the charged particle transfers part of its kinetic energy to a shell electron, which leads to ionization or excitation of the atoms in the medium. In case the medium is a semiconductor, the generation of electron-hole-pairs (e-h-pairs) also contributes to the energy loss of the traversing charged particle and can be treated like ionization. The number and energy transfer of ionizations, excitations, and e-h-pair creations of a particle traversing a medium are statistical. For a sufficiently high number of interactions, typically, the mean energy loss per path length  $-\left\langle \frac{dE}{dx} \right\rangle$  can be calculated with the Bethe-Bloch-equation [KW20]:

$$-\left\langle \frac{dE}{dx} \right\rangle = K \frac{Z}{A} \rho \frac{z^2}{\beta^2} \left[ \frac{1}{2} \ln \frac{2m_e c^2 \beta^2 \gamma^2 T_{\text{max}}}{I^2} - \beta^2 - \frac{\delta(\beta \gamma)}{2} - \frac{C(\beta \gamma, I)}{Z} \right]$$
(1.5)

z,  $\beta$ , and  $\gamma$  are the charge, velocity, and the Lorenz factor of the traversing particle, Z, A, and  $\rho$  are the charge, mass number, and density of the medium,  $m_{\rm e}$  is the mass of an electron, I is the mean excitation energy of an electron in an atom in the medium,  $T_{\rm max}$  is the maximum energy transfer per collision with a shell electron,  $\delta$  is the so-called density correction relevant at large values of  $\beta$ , C is the so-called shell correction relevant at small values of  $\beta$  and  $K=0.307 \, \frac{{\rm MeV \, cm^2}}{{
m mol}}$  is a constant.

The energy of a charged particle traversing the electric field of a nucleus decreases due to the emission of photons from the particle. This process is called bremsstrahlung. The energy per time dW/dt which is emitted from the particle through bremsstrahlung has

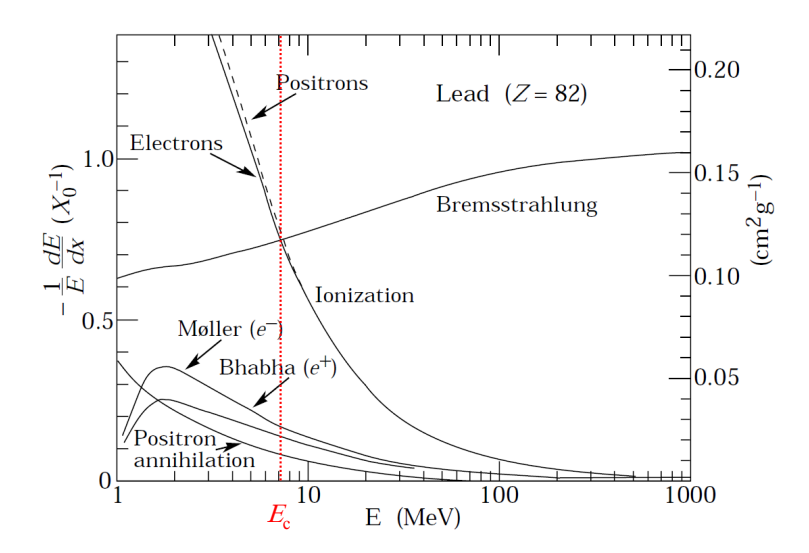


Figure 1.2: Fractional energy loss per radiation length as a function of electron or positron energy in lead [Win18].

the following proportionality [KW20]:

$$\frac{dW}{dt} \propto \frac{Z^2 E}{m^2} \tag{1.6}$$

E and m describe the energy and mass of the traversing particle and Z describes the charge number of the nucleus. Because of the inverse proportionality to the square of the particle mass, bremsstrahlung is most important for low-mass particles like  $e^-$  and  $e^+$ . Bremsstrahlung decreases the particle's energy E(x) exponentially as follows [KW20]:

$$E(x) = E_0 e^{\frac{x}{X_0}} \tag{1.7}$$

 $E_0$  describes the initial particle energy, x denotes the thickness of the material the particle traverses, and  $X_0$  is the so-called radiation length.  $X_0$  is material specific and describes the length after which an electron has lost, on average, 1 - 1/e of its initial energy through bremsstrahlung.  $X_0$  is also equal to 7/9 of the mean free path after which a photon undergoes pair production. With an accuracy of around 2.5 %,  $X_0$  can be approximated as follows [KW20]:

$$X_0 = \frac{716.408A}{\rho Z(Z+1) \ln \frac{287}{\sqrt{Z}}} \frac{\text{mol}}{\text{cm}^2}$$
 (1.8)

A, Z, and  $\rho$  describe the mass number, charge number, and density of the material. Figure 1.2 shows the energy loss of charged particles traversing lead as a function of the particle's energy for different processes. Because the energy loss via ionization has a different energy dependence than the energy loss via bremsstrahlung, the two curves intersect at a material-specific energy  $E_c$ .  $E_c$  is called critical energy and defines the point

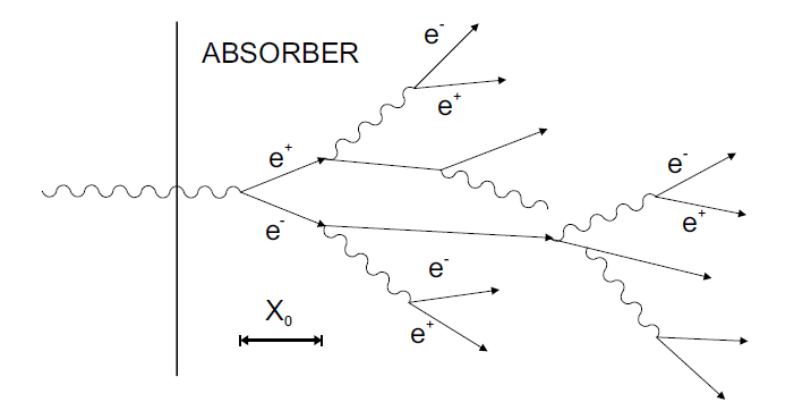


Figure 1.3: Graphic of an electromagnetic shower [RL01].

at which energy loss via ionization and energy loss via bremsstrahlung are equal [KW20]:

$$\left(\frac{dE}{dx}(E_{c})\right)_{\text{ionization}} = \left(\frac{dE}{dx}(E_{c})\right)_{\text{bremsstrahlung}}$$
(1.9)

For energies smaller than  $E_c$ , energy loss through ionization is larger than the energy loss through bremsstrahlung. For energies larger than  $E_{\rm c}$ , the opposite is the case.

#### Electromagnetic showers:

When a photon, electron, or positron with an energy above a few MeV enters a medium, an electromagnetic shower develops. Figure 1.3 depicts the development of an electromagnetic shower in a medium. The processes through which electromagnetic shower development is driven are pair production for photons and bremsstrahlung for leptons. Both processes require an electric field of a nucleus with charge number Z, and their cross-sections are proportional to  $\mathbb{Z}^2$ . Thus, a shower develops faster in a material with a high Z, like lead or tungsten, compared to a material with a low Z. The properties of an electromagnetic shower can be described by a model, which assumes that photons only interact via pair production and leptons only interact via bremsstrahlung, as long as their energy is above the critical energy  $E_{\rm c}$ . Under these assumptions, the maximum number  $N_{\text{max}}$  of particles in an electromagnetic shower induced by a primary particle with energy E and the depth  $t_{\text{max}}$  in units of  $X_0$  where the electromagnetic shower reaches its maximum can be calculated as [KW20]:

$$N_{\text{max}} = \frac{E}{E_{\text{c}}}$$

$$t_{\text{max}} = \frac{\ln(E/E_{\text{c}})}{\ln(2)}$$

$$(1.10)$$

$$t_{\text{max}} = \frac{\ln(E/E_{\text{c}})}{\ln(2)} \tag{1.11}$$

In the lateral direction, an electromagnetic shower is characterized by the Molière radius  $R_{\rm M}$ , which is defined as the radius of a cylinder centered at the shower axis in which 90 % of the total energy of an electromagnetic shower is deposited.  $R_{\rm M}$  can be calculated as follows [KW20]:

$$R_{\rm M} = \frac{22.1 \,\text{MeV}}{E_{\rm c}} X_0 \tag{1.12}$$

 $E_{\rm c}$  and  $X_0$  are the critical energy and the radiation length of the medium. For example, tungsten (W) has a Moliere radius of 9.327 mm [Wor22].<sup>1</sup>

## 1.1.2 Hadronic interactions

Hadrons interact with matter mainly via hadronic interaction and, if they are charged, ionization and bremsstrahlung. Since many different hadronic interactions are possible, their theoretical description is more difficult than that of electromagnetic processes. The hadronic absorption length  $\lambda_a$  is defined similarly to the radiation length as follows [KW20]:

$$N(x) = N_0 e^{-\frac{x}{\lambda_a}} \tag{1.13}$$

 $N_0$  is the initial number of hadrons and N(x) is the number of hadrons left after they traverse a material of thickness x.  $\lambda_a$  can be approximated as follows [KW20]:

$$\lambda_{\rm a} \approx \frac{A}{N_{\rm A}\rho\sigma_{\rm inel}}$$
 (1.14)

 $\sigma_{\rm inel}$  describes the cross-section for inelastic hadronic processes,  $N_{\rm A}$  is the Avogadro number, and  $\rho$  refers to the particle density of the traversed material. For materials with high Z, the hadronic absorption length is typically much larger than the radiation length [KW20]. For example, the hadronic absorption length for tungsten (W) is 99.46 mm [Wor22].

#### Hadronic showers:

Hadronic showers are generated by a hadron with sufficiently high energy traversing a medium. While two different processes dominate the development of electromagnetic showers, hadronic-shower development is influenced by many different interaction processes. This makes hadronic showers much more difficult to model than electromagnetic showers. Figure 1.4 depicts a graphic of an inelastic interaction of a hadron with a nucleus of a medium. During the interaction, the nucleus gets excited and releases most of the energy from the excitation by emitting hadrons, which are mostly neutrons and protons. This process is called spallation and happens at a timescale of  $10^{-22}$  s. After the interaction, most protons lose their energy by ionization. Neutrons can travel further through the medium since they do not ionize and have a high probability of interacting with another nucleus, repeating the previously described spallation processes and contributing to the development of a hadronic shower. After the spallation, the nucleus is still in an excited state and loses the remaining excitation energy by a process called evaporation.

<sup>&</sup>lt;sup>1</sup>The descriptions in section 1.1.1 are based on [KW20].

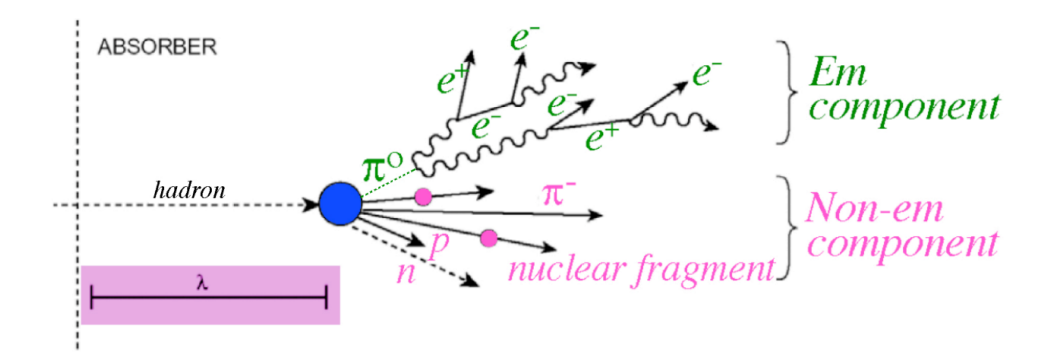


Figure 1.4: Graphic of a hadronic interaction [Lee18].

During evaporation, the nucleus emits nucleons and nuclear fragments at timescales of about  $10^{-18}$  s. The energy of the evaporated nucleons is about two orders of magnitude lower than that of the nucleons emitted during spallation. Therefore, neutrons from evaporation usually do not induce further spallation reactions and instead are slowed down and absorbed. During inelastic interactions between hadrons and nucleons, many light mesons are produced, of which pions are the most frequent. One third of pions are  $\pi^0$  of which 98.8% decay into two photons with a lifetime of  $\tau_{\pi^0} = 8.43 \cdot 10^{-17}$  s [Wor22]. The photons from the pion decays initiate electromagnetic showers that overlap with the hadronic shower.<sup>2</sup>

## 1.2 Electromagnetic calorimeters

In nuclear and particle physics, electromagnetic calorimeters measure the kinetic energy of electrons, positrons, or photons. In the following, the particle whose energy is measured is called the primary particle. The measurement of the energy of a particle usually requires the deposition of all of the primary particle's energy inside the volume of the calorimeter. Thus, the primary particle does not exit the calorimeter and is no longer available for further measurements. In electromagnetic calorimetry, the formation of electromagnetic showers is utilized. The particles in an electromagnetic shower induce a signal in the calorimeter. The shower particles are called secondary particles. The precise measurement of the energy of the primary particle requires that all secondary particles are confined inside the calorimeter's volume.

#### Electromagnetic calorimeter types:

For the measurement of the energy of a particle with a calorimeter, two steps are performed: the induction of an electromagnetic shower from an incoming primary particle and the generation of a signal from the secondary particles that is proportional to the primary particle's energy. Depending on how these two steps are accomplished, calorimeters

<sup>&</sup>lt;sup>2</sup>The descriptions in section 1.1.2 are based on [KW20].

can be classified as one of two types: homogeneous calorimeters and sampling calorimeters.

In a homogeneous calorimeter, both steps take place in a single material. This material needs to be dense enough to induce an electromagnetic shower while simultaneously being able to create a signal from the secondary particles of the electromagnetic shower. In most cases, the signal is created in the form of scintillation light. Therefore, the material must be able to create and conduct scintillation light from charged particles. Lead tungstate (PbWO<sub>4</sub>) is widely used for homogeneous calorimeters. Homogeneous calorimeters usually feature a better energy resolution than other types of electromagnetic calorimeters. In sampling calorimeters, the induction of an electromagnetic shower and the measurement of secondary particles take place in different components. A passive medium with a high Z and low  $X_0$  is used to generate the electromagnetic shower. This allows the calorimeter to feature a small depth while still containing the electromagnetic shower. Materials such as lead (Pb) or tungsten (W) are most commonly employed for this task. An active medium with usually a lower Z than the passive medium is required to measure the secondary particles. A wide variety of different technologies are employed for the detection of secondary particles in calorimeters. These include scintillators, ionization chambers, proportional chambers, and, recently, silicon pixel sensors. Sampling calorimeters can be designed in multiple ways: in a sandwich design, active and passive layers are arranged alternately in a stack. Other design options are shashlik and spaghetti designs. The shashlik design is similar to the sandwich design but features a light-conducting fiber that runs perpendicular to the absorber and scintillator plates. The spaghetti design features a block of absorber material through which fibers of scintillating material pass through. The advantage of most sampling calorimeter designs over homogeneous calorimeters is the ability to measure the shower shape in the longitudinal or lateral direction, which allows one to distinguish between electromagnetic and hadronic showers.

### Performance of electromagnetic calorimeters:

A calorimeter's three most important performance characteristics are linearity, energy resolution, and position resolution. The Linearity and energy resolution are most relevant for this thesis. The performance characteristics are introduced in the following.

In a perfect electromagnetic calorimeter, i.e. an infinitely large calorimeter with 100% detection efficiency and no saturation effects, one expects the amplitude S of the signal the calorimeter produces to be proportional to the energy E of the primary particle as S and E are linked via the following linear dependencies:

$$E \propto N_{\rm sec} \propto N_{\rm sec,ch} \propto S$$
 (1.15)

 $N_{\rm sec}$  is the number of secondary particles in the shower and  $N_{\rm sec,ch}$  is the number of charged secondary particles. The linear dependence between S and E is not exactly met

in a real calorimeter, caused by, for example, the leakage of secondary particles outside of the calorimeter volume and the saturation of large signals. The degree to which S depends linearly on E is called linearity and is an important performance characteristic of an electromagnetic calorimeter.

The energy resolution is defined as  $\sigma_{\rm E}/E$ , where  $\sigma_{\rm E}$  is the uncertainty on the energy measurement of the primary particle. Usually, calorimeters with a low energy resolution are desirable as they feature a more precise energy measurement than calorimeters with high energy-resolution values. In the above-mentioned perfect calorimeter, the energy resolution is determined only by statistical fluctuations of the number of secondary particles and can be calculated as follows [KW20]:

$$\frac{\sigma_{\rm E}}{E} \propto \frac{\sqrt{N_{\rm sec}}}{N_{\rm sec}} = \frac{1}{\sqrt{N_{\rm sec}}} \propto \frac{1}{\sqrt{E}}$$
 (1.16)

In a realistic calorimeter, additional effects with different energy dependencies increase the energy resolution. The dependence of the energy resolution on E is generally expressed as follows [KW20]:

$$\frac{\sigma_{\rm E}}{E} = \sqrt{\frac{a^2}{E} + \frac{b^2}{E^2} + c^2} \tag{1.17}$$

a is a parameter describing the influence of stochastic fluctuations in the shower development, b describes the influence of electronic noise on the energy resolution, and c describes the influence of electronic and mechanical imperfections and leakage on the energy resolution. While the noise term becomes most important at low energies, the constant term becomes most important at high energies.

Besides the energy measurement, with most calorimeters, the position where the primary particle hits the calorimeter can be measured. The degree to which the position of the primary particle can be resolved is called position resolution. For a calorimeter to deliver information about the primary particle's position, it has to be segmented laterally. The position resolution depends mainly on the size of each segment. A more accurate position measurement can be achieved when the electromagnetic shower spreads over multiple segments compared to when it is confined to a single segment. Electromagnetic calorimeters can usually achieve position resolutions of a few mm. However, with the application of silicon pixel sensors in calorimeters, position resolutions of a few µm can be reached.<sup>3</sup>

## 1.3 Semiconductor sensors

This thesis focuses on a calorimeter that facilitates semiconductor sensors for the generation of signals induced by charged particles. This section presents the general physics principles of semiconductors and introduces silicon pixel sensors, a type of semiconductor sensor. Finally, digital pixel calorimeters are described.

<sup>&</sup>lt;sup>3</sup>The descriptions in section 1.2 are based on [KW20].

## 1.3.1 Semiconductors

Solid materials can be categorized into three types according to their conductivity: conductors, semiconductors, and isolators.

Due to most solids' dense and periodic structure, some energy levels occupyable by electrons group so closely that they can be combined into energy bands, which are separated by a band gap. The two highest bands are called the valence band (VB) and the conduction band (CB). The conductivity of a solid depends on the gap between VB and CB.

Conductors feature overlapping VB and CB; isolators have band gaps  $> 9 \,\mathrm{eV}$ , and semi-conductors typically feature a band gap of a few eV (1.12 eV for silicon [KW20]).

Semiconductors typically feature a resistivity between  $10^{-3}$  and  $10^{8} \Omega \text{cm}$  [KW20]. Semiconductors can either be made of a single element, e.g., silicon (Si) or germanium (Ge), or of a compound of different elements, e.g., gallium arsenide (GaAs) or cadmium telluride (CdTe). Of these, silicon is the most widely used.

In semiconductors, the so-called Fermi level, defined as the energy at which a hypothetical energy state would be occupied with a probability of 50%, is usually between the VB and CB. The excitation of electrons from the VB to the CB is possible either thermally or through an external electric field. The latter case applies when a charged particle traverses a semiconductor. Through the excitation of an electron into the CB, a free electron and a hole (e-h-pair) are created, which can both be treated as free charge carriers. The e-h-pairs contribute to the conductivity of the semiconductor.

### Doping:

The process of altering the physical properties of a semiconductor by introducing impurities is known as doping. By doping a semiconductor, its properties can be changed. Impurities in the form of pentavalent atoms, such as Phosphorus (P), Nitrogen (N), or Arsenic (As), are called n-type doping. If pentavalent atoms are introduced into a tetravalent semiconductor, they occupy spots in the crystal lattice that atoms of the semiconductor would have filled in an undoped case. Four of the five valence electrons of the introduced pentavalent atom bond with the four surrounding semiconductor atoms, and the fifth valence electron remains bound to the pentavalent atom. Therefore, the fifth valence electron can be excited into the CB, which results in the pentavalent atom being an electron donor. Therefore, in n-type semiconductors, the Fermi level is shifted towards the CB. On the other hand, doping with trivalent atoms such as Boron (B), Gallium (G), or Indium (In) is called p-type doping and has the opposite effect to n-type doping. When a trivalent atom is introduced into the crystal lattice of a semiconductor, its three valence electrons bond with three of the four surrounding semiconductor atoms. Thus, a hole is left between the trivalent atom and one of the neighboring semiconductor atoms. Therefore, p-type doping introduces electron acceptors into the semiconductor, which shifts the Fermi level towards the VB.

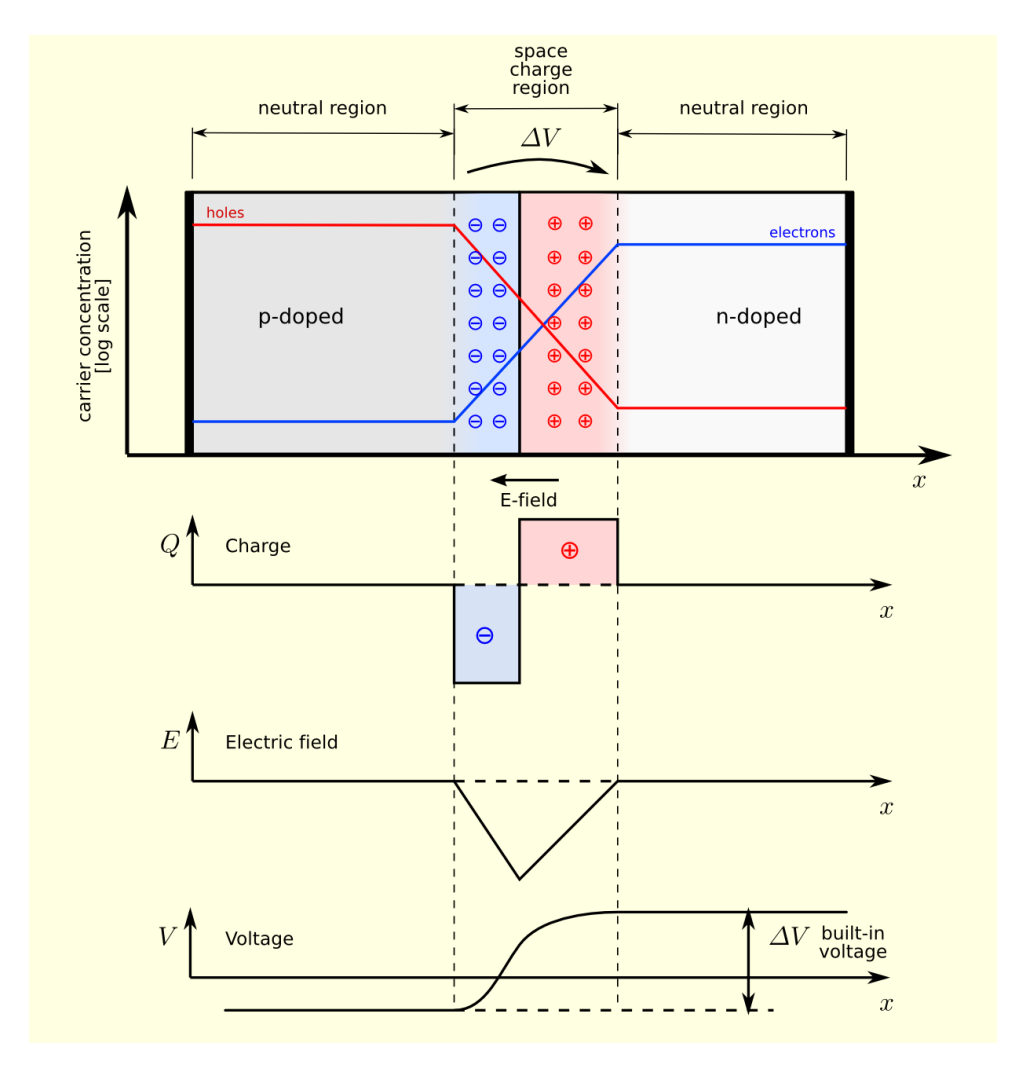


Figure 1.5: Graphic of a p-n junction and the distributions of the charge carrier concentrations, charge, electric field, and built-in voltage [Wik23c].

#### **Junctions:**

Many junctions with unique physical properties are possible between semiconductors and other solids. The junction between a p-type and a n-type semiconductor (p-n junction) is most interesting for detector applications. When a p-type and a n-type semiconductor are in contact with each other with an undisturbed crystal lattice at the contact surface, the abundance of electrons in the n-type region compared to the p-type region leads to a diffusion of electrons from the n-type region towards the p-type region, where the electrons combine with holes. Simultaneously, holes travel from the p-type region to the n-type region, where they combine with electrons.

Figure 1.5 shows the distributions of the charge, the electric field, and the voltage of a p-n junction. The diffusion of electrons and holes leads to the formation of a zone without charge carriers called depletion region. Inside the depletion region, the semiconductor is no longer neutrally charged. Instead, in the n-type region of the depletion region, a positive charge accumulates, and in the p-type region, a negative charge builds up.

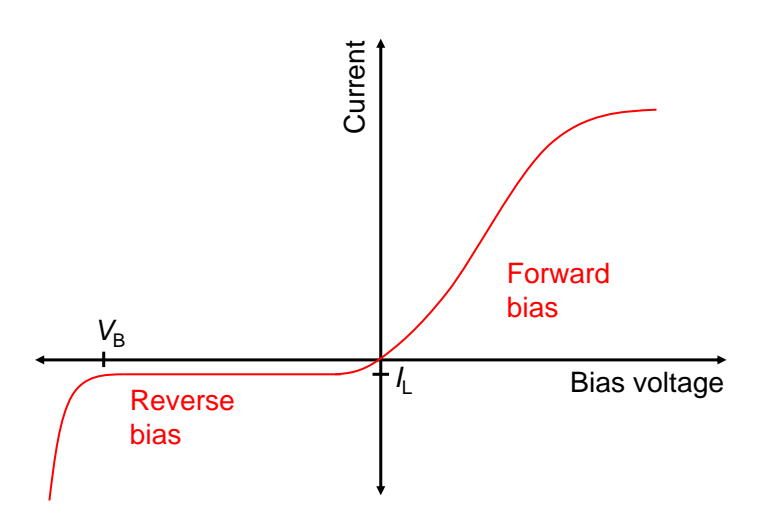


Figure 1.6: Illustration of the current dependence on the bias voltage of a p-n junction, based on [Wik23a].

Therefore, the depletion region is also called the space charge region. Due to the non-zero space charge inside the depletion region, an electric field is generated, and a voltage  $V_{\rm Bi}$ , called the built-in voltage, is present. The size  $x_{\rm p}$  of the depletion region inside the p-type region can be calculated as follows [KW20]:

$$x_{\rm p} = \sqrt{\frac{2\epsilon\epsilon_0}{e} V_{\rm bi} \frac{N_{\rm D}}{N_{\rm A}(N_{\rm D} + N_{\rm A})}}$$
 (1.18)

 $x_{\rm p}$  depends on the doping concentrations  $N_{\rm D}$  and  $N_{\rm A}$  of the n-type and p-type regions, the permittivity  $\epsilon$  of the semiconductor and the built-in voltage. The size  $x_{\rm n}$  of the depletion region inside the n-type region can be calculated as follows [KW20]:

$$x_{\rm n} = \sqrt{\frac{2\epsilon\epsilon_0}{e} V_{\rm bi} \frac{N_{\rm A}}{N_{\rm D}(N_{\rm D} + N_{\rm A})}}$$
 (1.19)

### Bias voltage:

An external voltage  $V_{\text{Bias}}$ , applied to a p-n junction, is called bias voltage. Figure 1.6 shows the current flowing through a p-n junction as a function of the bias voltage. If the external voltage is positive in the p-type region relative to the n-type region, it is called forward-bias voltage. Under a forward-bias voltage, more electrons diffuse from the n-type region to the p-type region and more holes from the p-type region to the n-type region than without external voltage. This decreases the size of the depletion region. A forward-bias voltage will induce a current flow through the p-n junction. An external voltage in the opposite direction than the forward-bias voltage is called reverse-bias voltage or

back-bias voltage. It has the opposite effect as the forward-bias voltage and extends the depletion region. If the back-bias voltage is larger than the breakdown voltage  $V_{\rm B}$ , which is a parameter specific to a p-n junction, no current except for the constant leakage current  $I_{\rm L}$  flows. For  $V_{\rm Bias} < V_{\rm B}$ , a current larger than  $I_{\rm L}$  flows. Most p-n junctions are not designed to operate below  $V_{\rm B}$  and would be damaged in that case. The behavior of a p-n junction under an external voltage implies, that for  $V_{\rm Bias} > V_{\rm B}$  current can only flow in one direction, except for the leakage current. Therefore, a p-n junction represents a diode.

To calculate the depth of the depletion region under an external voltage, one can use equation 1.19 and 1.18 and substitute  $V_{\rm bi}$  with  $V_{\rm bi} - V_{\rm bias}$ . In that case,  $V_{\rm bias}$  must be defined in a way that it has positive values under forward-bias voltage and negative values under back-bias voltage.<sup>4</sup>

## 1.3.2 Silicon pixel sensors

Silicon pixel sensors are widely used to detect particles. Their most common application is the reconstruction of particle tracks. However, other use cases of silicon pixel sensors, e.g., calorimetry, are possible. The use of silicon pixel sensors in a calorimeter is explored in this work.

Silicon pixel sensors contain a plane with a matrix of rectangular or, in some cases, hexagonal pixels, of which each usually contains one diode. A silicon pixel sensor delivers information about the location of a particle traversing the sensor in the form of pixel hits. To achieve this, silicon pixel sensors utilize the generation of e-h-pairs by a charged particle traversing the silicon. In most silicon sensors, e-h-pairs are generated inside or near the depletion region of one or more of the pixel's diodes. The diodes collect the charge carriers liberated by the passing particle and generate an analog voltage signal. This analog signal is then transformed into a digital signal.

The most common types of silicon pixel sensors are hybrid pixel sensors and monolithic active pixel sensors.

Hybrid pixel sensors have two components: A sensor part, made of silicon, containing the pixel matrix, and a readout part containing the electronics to transform and store the signals generated by the pixel's diodes. The readout part usually has the same grid structure as the pixel matrix and is bonded on top of the sensor part.

Pixel sensors where the sensor part and readout part are located on the same piece of silicon are called monolithic active pixel sensors (MAPS). MAPS have several advantages compared to hybrid pixel sensors: MAPS require up to one order of magnitude less material than hybrid pixel sensors, improving the position resolution in tracking applications due to reduced particle scattering on the sensors. In most cases, MAPS are cheaper than hybrid pixel sensors since the time-consuming and expensive process of bonding the read-

<sup>&</sup>lt;sup>4</sup>The descriptions in section 1.3.1 are based on [KW20], [Wik23c], and [Wik23a].

out part to the sensor part is not required to manufacture MAPS. The functionality of a specific model of MAPS will be discussed in detail in section 2.1.3 on the example of the so-called ALPIDE sensor.<sup>5</sup>

## 1.3.3 Digital pixel calorimeters

Although MAPS are usually used for tracking, applying MAPS in calorimeters is also possible. The possibility of including partial or fully digital calorimeters that rely on MAPS for signal generation in large-scale experiments is currently being explored [Pei18]: One example is the proposed ALICE FoCal detector [Pei18]. In preparation for the inclusion of digital pixel calorimeters in large-scale experiments, several prototypes of digital pixel calorimeters are studied. Studies with these prototypes already proved that energy measurements with a digital pixel calorimeter are possible. Two examples of such prototypes are the so-called EPICAL-1 [Pei18] and EPICAL-2 [Alm23]. This thesis focuses on the EPICAL-2. A detailed description of this particular digital pixel calorimeter prototype is presented in the next chapter.

Digital pixel calorimeters often have better position resolution compared to most other calorimeters due to the pixel size in MAPS being smaller than the lateral segmentation of most other calorimeters. Furthermore, in most digital pixel calorimeters, it is possible to study the development of particle showers and to distinguish electromagnetic showers from hadronic showers. This is further discussed in section 4.4.2. Another unique ability of digital pixel calorimeters is the separation of two electromagnetic showers down to distances smaller than the Molière radius of the absorber material utilized in the digital pixel calorimeter.<sup>6</sup>

<sup>&</sup>lt;sup>5</sup>The descriptions in section 1.3.2 are based on [KW20].

<sup>&</sup>lt;sup>6</sup>The descriptions in section 1.3.3 are based on [KW20], [Pei18], and [Alm23].

## Chapter 2

# Experimental setup

This work focuses on studies with a digital pixel calorimeter prototype named EPICAL-2. Specifically, data recorded with the EPICAL-2 during two test-beam campaigns and simulations of the EPICAL-2 are analyzed in the scope of this thesis. This chapter describes the pixel calorimeter, the setup of the EPICAL-2 during data taking, and the test-beam facilities where the data was recorded. Measurements with the EPICAL-2 have been performed primarily in the context of [Alm23] and [Rog23a].

## 2.1 The EPICAL-2 calorimeter

The EPICAL-2 was developed and tested with the goal of studying the performance of MAPS in the context of calorimetry. Research on this topic has already been done with the predecessor of the EPICAL-2 called EPICAL-1. Compared to its predecessor, the EPICAL-2 features improved readout time and fewer faulty pixels.

## 2.1.1 Design and coordinate system

The EPICAL-2 has a sandwich design that consists of 24 identical layers. Figure 2.1 shows a graphic (left) and a photo (right) of one layer of the EPICAL-2. Each layer is composed of one  $40 \times 40 \times 3 \,\mathrm{mm}^3$  tungsten absorber. The absorber enables electrons and photons to interact via bremsstrahlung and pair production and, in the following, contribute to the development of an electromagnetic shower. On two opposing edges of the tungsten absorber 4 mm wide and 0.5 mm thick tungsten spacers are located. They are necessary to generate a 0.5 mm thick space between the absorbers of two consecutive layers. Inside this space, two MAPS, which are used for signal generation inside the EPICAL-2, are placed. The sensors cover an area of  $30 \times 30 \,\mathrm{mm}^2$ , of which  $27.6 \times 29.9 \,\mathrm{mm}^2$  is sensitive. Between the two sensors in the same layer, an approximately  $100 \,\mathrm{\mu m}$  wide gap in the active surface is present. Each sensor is bonded to a so-called sensor cable. Both sensor cables of one layer are bonded to a so-called layer cable, which allows communication between the two sensors in a layer and the readout electronics.

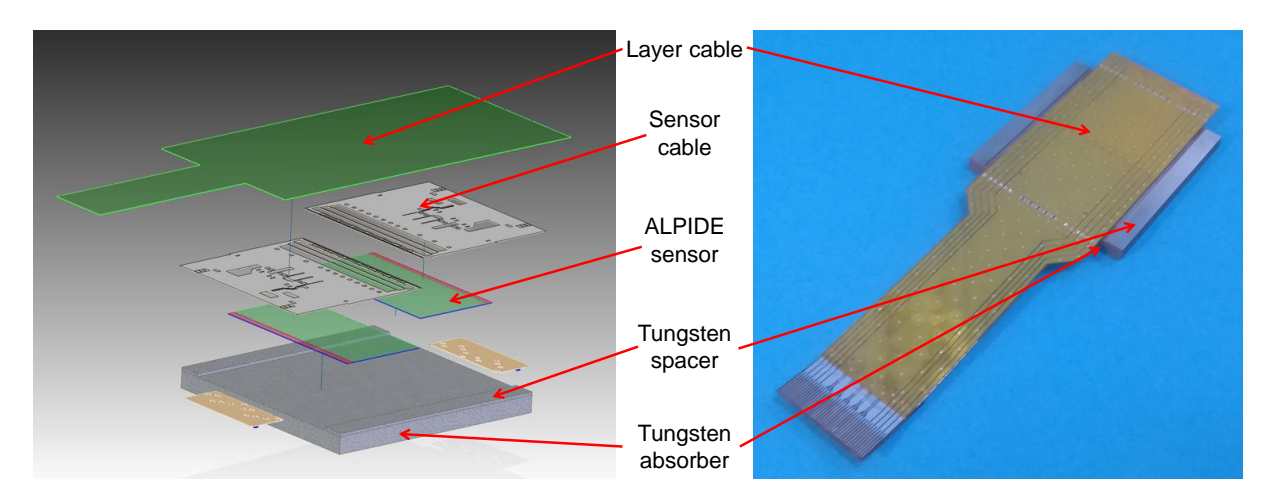


Figure 2.1: Graphic (left) and photo (right) of one layer of the EPICAL-2 [Alm23].

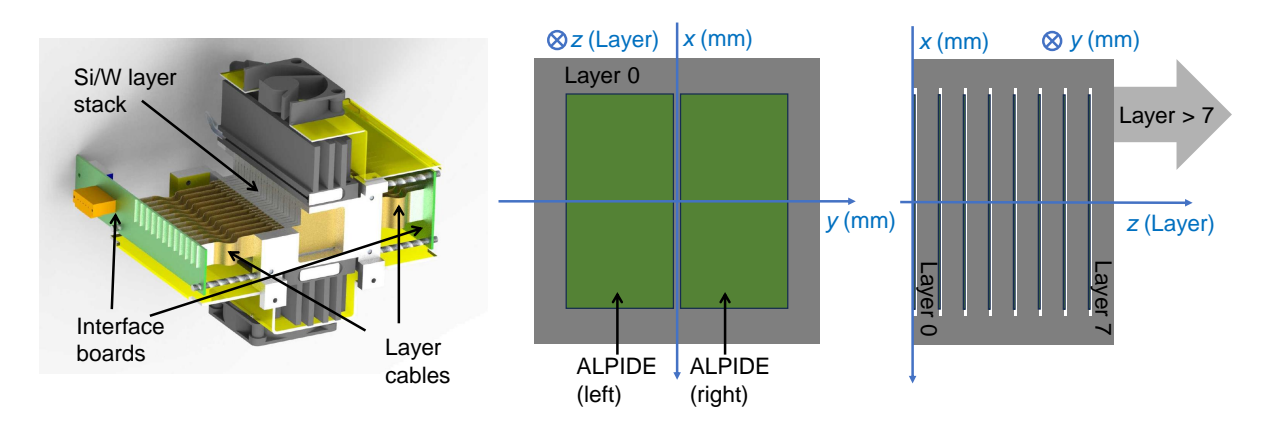


Figure 2.2: Graphic of the EPICAL-2 (left) [Alm23], illustration of the EPICAL-2 coordinate system in the lateral plane (center), and illustration of the EPICAL-2 coordinate system in the longitudinal direction (right).

Figure 2.2 (left) presents a graphic of the EPICAL-2. The 24 layers are stacked on each other and numbered consecutively from 0 to 23, with layer 0 standing out as the only layer with no absorber in front of the sensors. The direction in which the layer cables protrude from the layer stack alternates between the layers. Therefore, all layer cables from even-numbered layers connect to a so-called interface board on the left side of the EPCIAL-2, and all layer cables from odd-numbered layers connect to another interface board on the right side of the EPCIAL-2. Each interface board houses the electronics necessary to power the 24 sensors connected to it and communicate with them. The layer stack is mounted inside an aluminum structure to stabilize it mechanically. The aluminum structure also supports a cooling system to keep the temperature of the sensors stable. This is necessary for consistent measurements as the behavior of the sensors is temperature dependent.

Figures 2.2 (center) and (right) illustrate the coordinate system used throughout this thesis to refer to positions inside the volume of the EPICAL-2. The x-y-plane of the coordinate system, also referred to as the lateral plane, lies parallel to the active surfaces of the sensors in one layer. The origin of the x-y-plane is located in the center of each

layer. Locations in this plane are measured in mm. The z-axis, also referred to as the longitudinal direction, is orthogonal to the x-y-plane. Its origin is the location of the sensors in layer 0. Measurements along the z-axis are given as layer numbers, with one layer corresponding to  $3.5 \, \text{mm}$ .

## 2.1.2 Measurement principle

The energy-measurement principle of the EPICAL-2 is based on the counting of charged particles in an electromagnetic shower induced by a primary particle. A charged particle traversing a sensor usually results in a group of adjacent pixel hits called a cluster, as will be discussed in section 2.1.3. Therefore, counting the number  $N_{\rm Hit}$  of pixel hits or the number  $N_{\rm Clus}$  of clusters are both viable to gain the number of charged particles in an electromagnetic shower inside the EPICAL-2. The number of charged particles in an electromagnetic shower is proportional to the energy of the primary particle as described in section 1.2. Given the assumption that the density of charged particles in an electromagnetic shower is sufficiently low that neither pixel hits nor clusters induced by different charged particles merge into a single pixel hit or cluster,  $N_{\rm Hit}$  and  $N_{\rm Clus}$  are both proportional to the energy of a primary particle inducing an electromagnetic shower. Therefore, in this thesis, both  $N_{\rm Hit}$  and  $N_{\rm Clus}$  are considered for the detector response of the EPICAL-2, which contains information about a primary particle's energy.

## 2.1.3 The ALPIDE sensor

The EPICAL-2 utilizes one of the most advanced MAPS available today, the so-called ALPIDE sensor, which was developed for the upgrade of the inner tracking system of the ALICE experiment at CERN [Mag16]. The sensor combines a spatial resolution of approximately 5  $\mu$ m with a detection efficiency of more than 99% and a fake hit rate of  $10^{-5}$  per pixel readout [Mag16]. The sensor is composed of a pixel matrix with 512 rows and 1024 columns of pixels with a pixel pitch of  $26.88 \,\mu$ m between rows and  $29.24 \,\mu$ m between columns, leading to a total pixel matrix size of  $13.763 \,\mathrm{x}\,29.942 \,\mathrm{mm}^2$ . A guard ring surrounds the pixel matrix, and one of the long edges of the sensor has approximately 1 mm of silicon excess besides the active area housing electronics for the sensor's readout. Due to the guard ring and the silicon excess, with  $15 \,\mathrm{x}\,30 \,\mathrm{mm}^2$ , the complete sensor is larger than the pixel matrix.

Figure 2.3 illustrates a segment of two pixels viewed parallel to the pixel matrix. The  $25\,\mu m$  thick active layer of a sensor, called the epitaxial layer, is located on top of a  $14\,\mu m$  thick substrate layer. Above the epitaxial layer, several metal layers with a total thickness of  $11\,\mu m$  are located. The metal layers contain the pixel's front-end electronics comprising of approximately 200 transistors per pixel.

Figure 2.3 also illustrates the signal generation in a sensor: A charged particle traversing the silicon of a sensor liberates charge carriers in the form of electron-hole-pairs (e-h-pairs).

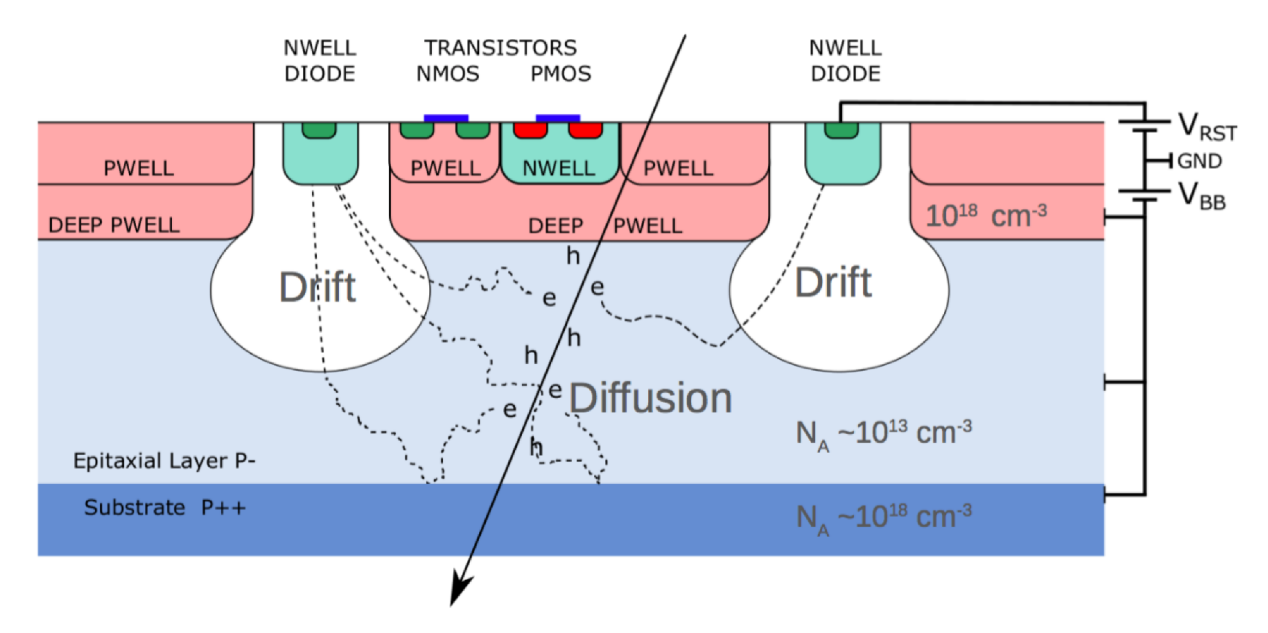


Figure 2.3: Illustration of the analog-signal generation in an ALPIDE sensor [RK19].

The charge carriers diffuse inside the p-type doped epitaxial layer. The deep p-well and substrate feature stronger p-type doping compared to the epitaxial layer. Therefore, an electric field develops on the junction between the deep p-well and the epitaxial layer and on the junction between the substrate and the epitaxial layer. These electric fields confine the diffusing charge carriers inside the epitaxial layer. Each pixel has an approximately  $2 \mu m$  tall and  $2 \mu m$  wide structure with n-type doping called n-well or collection implant. The collection implant and the epitaxial layer form a p-n junction with the built-in voltage  $V_{\rm RST}$ , which generates an electric field inside the depletion region surrounding the collection implant. When electrons diffusing in the epitaxial layer reach this electric field, they drift toward the collection implant and are eventually collected by it. This leads to an accumulation of negative charge on the collection implant. Since the collection implant has a capacitance C, the collected charge Q generates a signal in the form of a negative voltage  $V_{\text{Sig}} = Q/C$ . A noteworthy feature of the sensor is the so-called charge sharing, which describes the generation of signals in multiple adjacent pixels by one charged particle traversing the sensor. Charge sharing occurs because one charged particle traversing a sensor liberates in the order of 10<sup>3</sup> charge carriers, which, due to their ability to diffuse inside the epitaxial layer, usually spread over multiple adjacent pixels.

The sensors support the application of a back-bias voltage  $V_{\rm BB}$ . As described in section 1.3.1,  $V_{\rm BB}$  enlarges the depletion region and thus the electric field surrounding the collection implant. Therefore, the region where the electrons drift increases with  $V_{\rm BB}$ , leading to reduced charge sharing. A study on the influence of back-bias voltage on the performance of the EPICAL-2 is conducted in the scope of this thesis and presented in section 5.3.

For completeness, the processing of the signal from a pixel's collection implant in the frontend electronics of the pixel is described in the following. Figure 2.4 illustrates the front-end

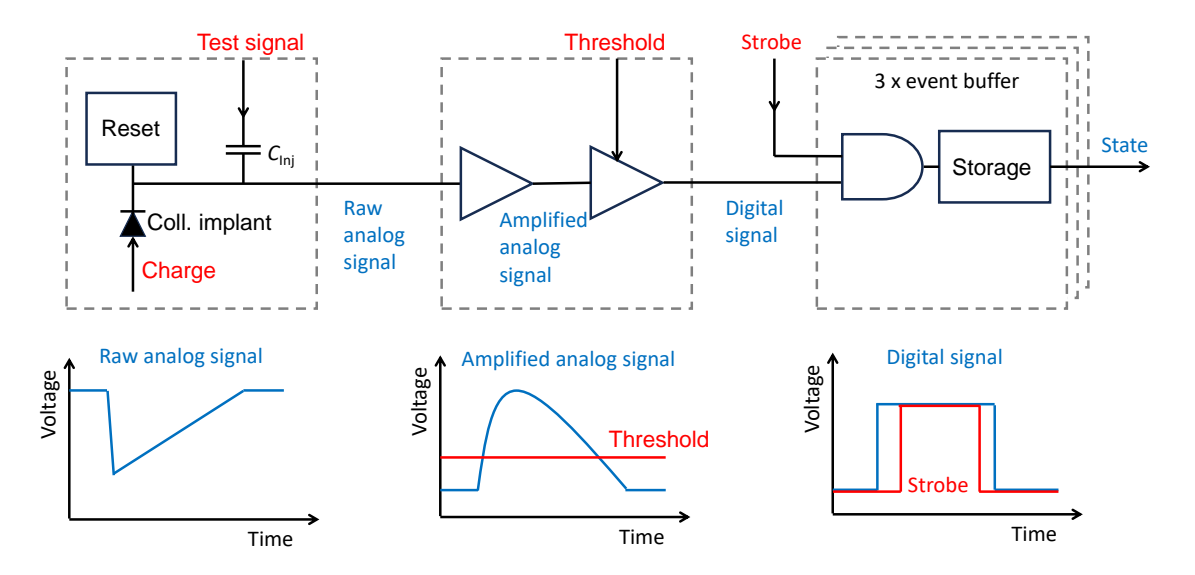


Figure 2.4: Illustration of the sensor's front-end electronics and signal processing, based on [Mag16].

electronics of a sensor, which amplifies, digitizes, and stores pixel signals generated at the collection implant. The first stage of the front-end electronics continuously resets the pixel signal. The decrease of the pixel signal from the collected charge takes place over approximately 10 ns, which is a shorter timescale than the reset of the pixel signal, which takes more than 100  $\mu$ s. In the second stage, the signal gets amplified and reshaped, and a digitization threshold is applied. In a sensor, the time  $t_{\rm Sig}$  in which a signal generated by a charged particle is over the digitization threshold is optimized to 5  $\mu$ s  $< t_{\rm Sig} < 10~\mu$ s. In the third stage, the digitized pixel signal is compared to an external strobe signal. Data is acquired by the sensor when it receives a strobe signal. If the strobe signal overlaps with a digitized pixel signal, the pixel registers and stores a hit. The pixel hits are stored in a so-called event buffer until the sensor is read out.<sup>1</sup>

## 2.2 Test-beam measurements

Test-beam measurements with the EPICAL-2 were performed at the DESY and the CERN-SPS test-beam facilities in the context of [Alm23] and [Rog23a]. Data from these test-beam measurements is analyzed in the context of this thesis. First, this section describes the setup of the EPICAL-2 at the test-beam facilities. Second, the DESY and the CERN-SPS test-beam facilities are introduced in this section.

## 2.2.1 EPICAL-2 setup

At both test-beam facilities, the EPICAL-2 was aligned in the beamline so that the test beam was parallel to the z-axis of the EPICAL-2. The temperature of the sensors in

<sup>&</sup>lt;sup>1</sup>The descriptions in section 2.1.3 are based on [RK19], [Mag16], and [Yua21].

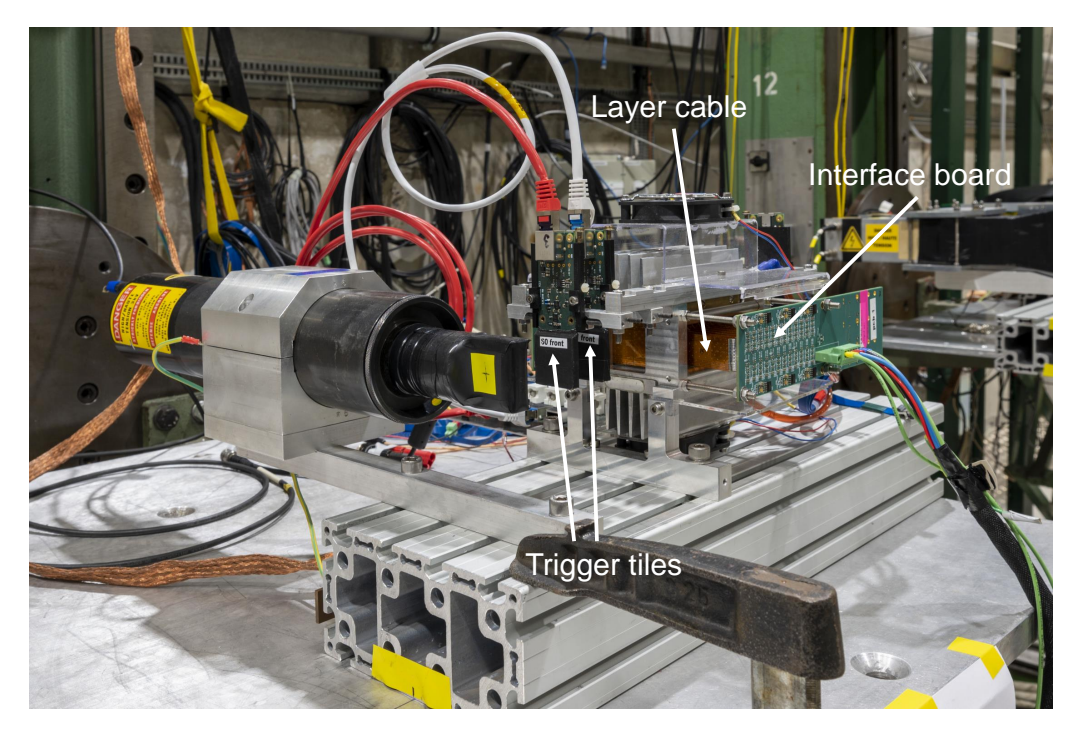


Figure 2.5: Photography of the EPICAL-2's setup at the CERN-SPS test-beam facility [Twi21].

the EPICAL-2 was stabilized at 20 °C with a water-cooling system. Figure 2.5 depicts a photograph of the EPICAL-2's setup at the CERN-SPS test-beam facility. During both test-beam campaigns, two scintillator-trigger tiles were placed approximately 35 mm in front and parallel to the active surface of layer 0 of the EPICAL-2. Each trigger tile features a surface area of  $3 \times 3 \, \mathrm{cm}^2$ , therefore covering the active surface of layer 0 of the EPICAL-2. When a particle traverses both trigger tiles, it induces coincident signals in them. When coincident signals are measured with the trigger tiles, the sensors in the EPICAL-2 receive a 2  $\mu s$  long strobe signal.

## 2.2.2 DESY

Data with the EPICAL-2 was recorded in February 2020 at the test-beam line TB22 of the DESY II facility in Hamburg (Germany). The beam of TB22 at DESY II is created as depicted in figure 2.6: Electrons or positrons of the DESY II beam hit a primary target composed of six  $7 \,\mu m$  thick and 30 mm long carbon fibers. At the primary target, photons within an energy range from 0.45 GeV to 6.3 GeV are created via bremsstrahlung. These photons travel tangentially to the beam orbit of the DESY II and leave the beam pipe through a 0.5 mm thick aluminum exit window. The photons travel 22 m through air before they hit a secondary target made from copper or aluminum. At the secondary target,  $e^+$ - $e^-$ -pairs are created from the photons via pair production. The  $e^+$  and  $e^-$  travel through an evacuated beam pipe until they reach a dipole magnet located 60 cm behind the secondary target. Via the configurable strength and polarity of the dipole magnet,

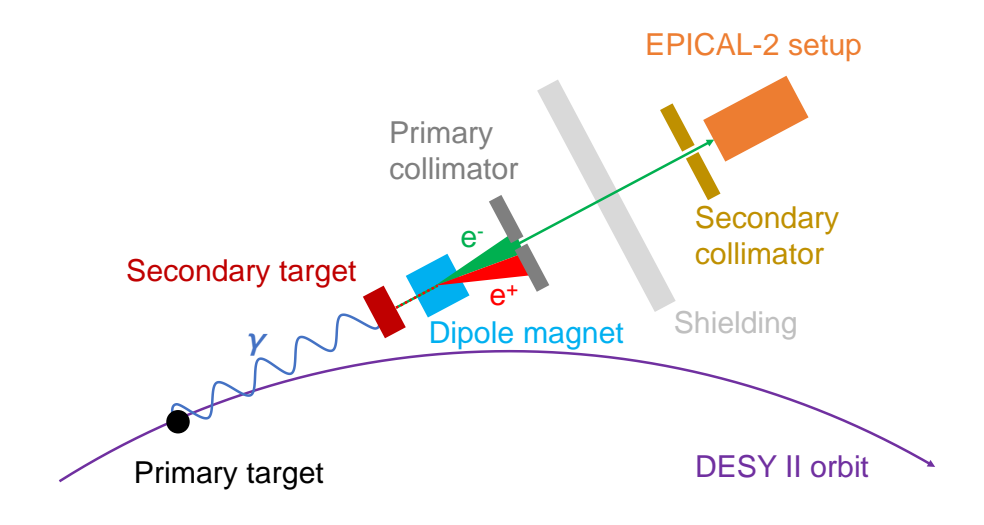


Figure 2.6: Graphic of the test-beam generation at DESY, based on [Die19].

momentum and particle type of the test beam are selected. After passing the dipole magnet, the selected test beam traverses a primary and a secondary collimator, which both narrow the test beam. Finally, the test beam enters the EPICAL-2. During the test-beam campaign with the EPICAL-2 at DESY, the primary collimator was set to  $14 \times 14 \text{ mm}^2$ , and the secondary collimator was set to  $12 \times 12 \text{ mm}^2$ . Electrons were measured at energies ranging from 1 GeV to 5.8 GeV with an energy uncertainty of 158 MeV independent of the beam energy [Die19].<sup>2</sup>

## 2.2.3 **CERN-SPS**

Data was recorded with the EPICAL-2 in September and October 2021 at the beam line H6 of the CERN-SPS facility near Prévessin (France). The test beam of H6 at CERN-SPS is generated as depicted in figure 2.7: A proton beam with an energy  $E_{\rm SPS,prim}=120\,{\rm GeV}$  hits a primary target made from beryllium. In reactions between the proton beam and the beryllium target, a secondary beam composed of electrons, muons, and hadrons is created. The secondary beam traverses a secondary target made from either 1 radiation length  $X_0$  of lead or  $30\,X_0$  of copper. In the case of a copper target, a tertiary beam composed purely of hadrons is created. In the case of a lead target, the particles from the secondary beam lose part of their energy by interacting with the lead target. Therefore, a tertiary beam composed of electrons, muons, and hadrons with an energy spectrum is generated. Usually, electrons lose more energy than hadrons when traversing the lead target. A dipole magnet bends the tertiary beam, which allows the selection of the momentum of

<sup>&</sup>lt;sup>2</sup>The descriptions in section 2.2.2 are based on [Die19].

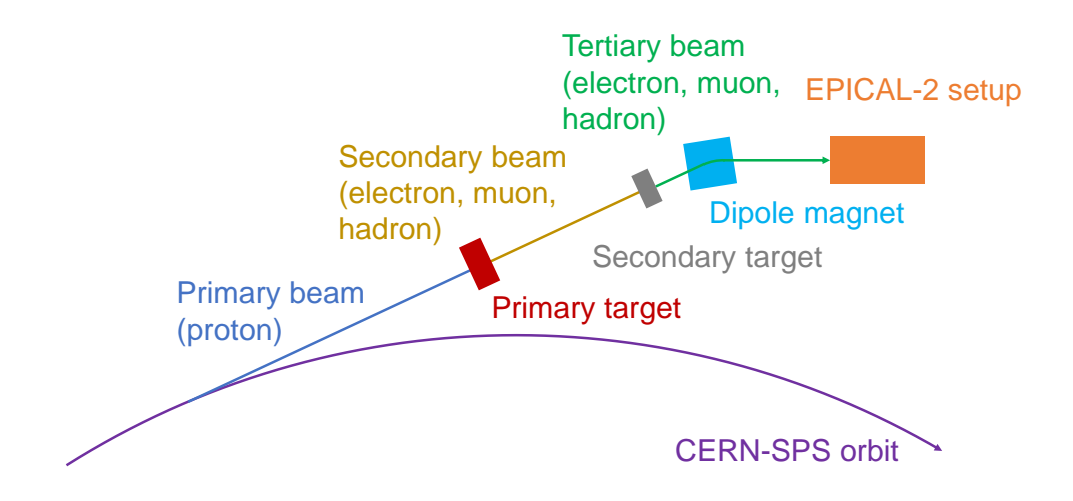


Figure 2.7: Graphic of the test-beam generation at CERN-SPS, based on descriptions in [Rog23a].

the beam. Due to the different behavior of electrons and hadrons in the secondary target, the fraction of electrons to hadrons decreases with increasing energy. Finally, the tertiary beam hits the EPICAL-2.

During the test-beam campaign with the EPICAL-2 at CERN-SPS, a secondary target made of lead was used, resulting in a test beam composed of electrons, muons, and hadrons. These particles were measured at energies ranging from  $20\,\mathrm{GeV}$  to  $80\,\mathrm{GeV}$  with an energy uncertainty of  $1.5\,\%$  of the beam energy [GR19].

<sup>&</sup>lt;sup>3</sup>The descriptions in section 2.2.3 are based on [Rog23a], and [GR19].

# Chapter 3

## Simulation

To compare the test-beam data with a Monte Carlo simulation and conduct studies of the leakage of the EPICAL-2, the EPICAL-2 and an enlarged version of EPICAL-2 are implemented in the Allpix<sup>2</sup> (v3.0.2) [Spa18] pixel detector simulation framework. The implementation of the EPICAL-2 in Allpix<sup>2</sup> in the context of this work is based on a previous implementation of the EPICAL-2 in Allpix<sup>2</sup> (v1.6.0) presented in [Rog23a]. The reimplementation in Allpix<sup>2</sup> (v3.0.2) is performed since Allpix<sup>2</sup> (v3.0.2) has several new functionalities, e.g. multithreading, compared to Allpix<sup>2</sup> (v1.6.0). Furthermore, the implementation is necessary since the original implementation in Allpix<sup>2</sup> (v1.6.0) is not compatible with Allpix<sup>2</sup> (v3.0.2) due to several changes in the framework.

This chapter presents the implementation of the EPICAL-2 simulation and tuning to model the test-beam data based on [Rog23a]. Furthermore, a comparison between the test-beam data and the simulation and the simulation of the enlarged calorimeter are described.

## 3.1 Implementation of the EPICAL-2 in Allpix<sup>2</sup>

The Allpix<sup>2</sup> framework is based on GEANT4 [Ago03] and ROOT [BR97] and is dedicated to the simulation of silicon pixel sensors. The design of Allpix<sup>2</sup> features several modules that fulfill specific tasks. A simulation chain in Allpix<sup>2</sup> can be constructed by combining multiple modules.

In the following, the modules used for the simulation of the EPICAL-2 and the implementation of the EPICAL-2 in each module are described. Although most of the EPICAL-2's implementation in Allpix<sup>2</sup> (v3.0.2) is identical to the implementation in Allpix<sup>2</sup> (v1.6.0), several changes were made. These changes are highlighted in the following.

#### GeometryBuilderGeant4:

The GeometryBuilderGeant4 module generates a 3-dimensional model of a detector inside a so-called world frame. Therefore, this module requires the input of the type, material,

| C             | Material | $x_{\text{pos}} (\text{mm})$ $y_{\text{pos}} (\text{mm})$ |                                   | $z_{\rm pos}({\rm mm})$ |  |
|---------------|----------|---|-----------------------------------|-------------------------|--|
| Component     | Type     | $x_{\rm size}$  | $y_{ m size}$                     | $z_{ m size}$           |  |
| Sensor A      | Silicon  | 0   | 0                                 | 0                       |  |
| Sensor A      | Active   | $1024 \times 29.24  \mu \text{m}$                         | $512 \times 26.88  \mu\mathrm{m}$ | 55 μm                   |  |
| Sensor B      | Silicon  | 0   | -13.86256                         | 0                       |  |
| Sensor D      | Active   | $1024 \times 29.24  \mu \text{m}$                         | $512 \times 26.88  \mu\mathrm{m}$ | 55 μm                   |  |
| Gap           | Silicon  | 0   | -6.93128                          | 0                       |  |
| Gap           | Passive  | $1024 \times 29.24  \mu \mathrm{m}$                       | 100 μm                            | $55\mu\mathrm{m}$       |  |
| Excess left   | Silicon  | 0   | -21.34784                         | 0                       |  |
| Excess left   | Passive  | $1024 \times 29.24  \mu \text{m}$                         | $1208\mu\mathrm{m}$               | 55 μm                   |  |
| Evenes right  | Silicon  | 0   | 7.48528                           | 0                       |  |
| Excess right  | Passive  | $1024 \times 29.24  \mu m$                                | $1208\mu\mathrm{m}$               | 55 μm                   |  |
| Evenes top    | Silicon  | 14.98588  | -6.93128                          | 0                       |  |
| Excess top    | Passive  | 30 μm   | $30.04112\mathrm{mm}$             | $55\mu\mathrm{m}$       |  |
| Excess bottom | Silicon  | -14.98588   | -6.93128                          | 0                       |  |
| Excess bottom | Passive  | 30 μm   | 30.04112 mm                       | $55\mu\mathrm{m}$       |  |
| Chip cable A  | Kapton   | 0   | -6.93128                          | -0.0425                 |  |
| Chip cable A  | Passive  | 31 mm   | $32\mathrm{mm}$                   | 30 μm                   |  |
| Chip cable B  | Aluminum | 0   | -6.93128                          | -0.0725                 |  |
| Chip cable b  | Passive  | 31 mm   | $32\mathrm{mm}$                   | 30 μm                   |  |
| Layer cable   | Kapton   | 0   | -6.93128                          | -0.2175                 |  |
| Layer cable   | Passive  | 31 mm   | $40\mathrm{mm}$                   | $145\mu\mathrm{m}$      |  |
| Absorber      | Tungsten | 0   | -6.93128                          | 1.53                    |  |
| Ansorner      | Passive  | $40\mathrm{mm}$   | $35\mathrm{mm}$                   | $3  \mu \mathrm{m}$     |  |
| Spacer A      | Tungsten | 18  | -6.93128                          | -0.22                   |  |
| Spacer A      | Passive  | $4\mathrm{mm}$  | $35\mathrm{mm}$                   | $0.5\mu\mathrm{m}$      |  |
| Spacer B      | Tungsten | -18   | -6.93128                          | -0.22                   |  |
| Spacer D      | Passive  | 4 mm  | $35\mathrm{mm}$                   | $0.5\mathrm{\mu m}$     |  |

Table 3.1: Overwiev of the implementation of the components of the EPICAL-2 in GeometryBuilderGeant4, exemplary for layer 0.

size, and location of every detector component. GeometryBuilderGeant4 also requires the specification of a world-frame material.

Since the test beam measurements with the EPICAL-2 were performed in air, the world-frame material is defined as air in this simulation. As mentioned in section 2.1, the EPICAL-2 consists of 24 identical layers, each composed of two ALPIDE sensors, cabling, a tungsten absorber, and two tungsten spacers. The implementation of these components in GeometryBuilderGeant4 exemplary for layer 0 is shown in Table 3.1. For every consecutive layer, the z-coordinate is increased by 3.5 mm. Both simulated sensors are implemented as a 50  $\mu$ m thick layer of active silicon representing the epitaxial layer and substrate with 5  $\mu$ m of passive silicon on top representing the front-end electronics. Each simulated sensor contains a matrix of  $1024 \times 512$  pixels. The pixel pitch is  $29.24 \times 26.88 \,\mu$ m<sup>2</sup> corresponding to the pixel pitch in a real sensor. To simulate the guard ring and read-out electronics of the sensor, the simulated sensor is surrounded by

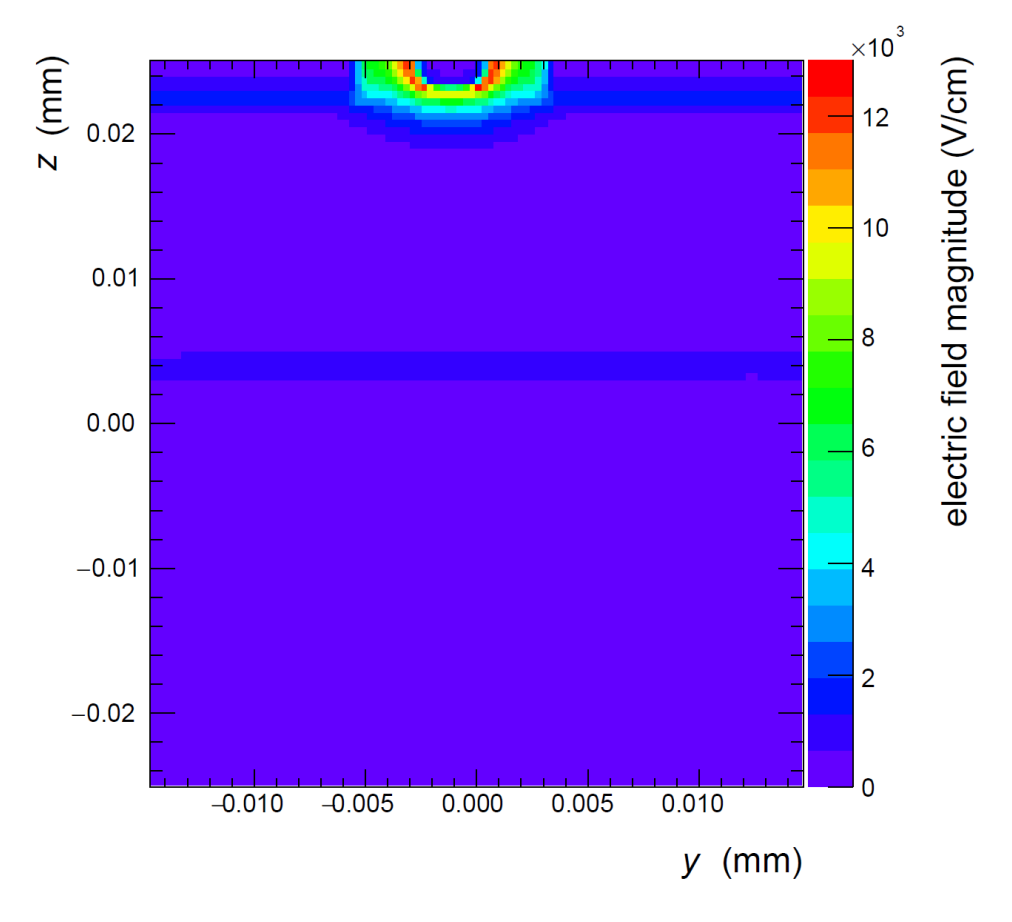


Figure 3.1: Projection on the x-axis of the electric-field map of a single pixel in the EPICAL-2 simulation [Rog23a].

passive silicon volumes referred to in table 3.1 as gap and excess. The cabling, absorber, and spacer are represented in the simulation by passive volumes of the corresponding material. Each simulated pixel contains a cylindrical collection volume with a diameter of  $2\,\mu m$  and a depth of  $2\,\mu m$  representing the collection implants of the sensors.

In the previous implementation of the EPICAL-2 in Allpix<sup>2</sup> (v1.6.0), the collection implants of the sensors are represented by two-dimensional  $3 \times 3 \mu m^2$  collection surfaces instead of three-dimensional collection volumes.

#### ElectricFieldReader:

Usually, in pixel sensors, an electric field is present in the pixels. The correct simulation of the electric field is vital for reliable simulation results because it influences the motion of charge carriers in the sensor. Therefore, the electric field in each pixel can be included in an Allpix<sup>2</sup> simulation via the so-called ElectricFieldReader module.

In this simulation, a 3-dimensional electric-field map is provided as input to the ElectricFieldReader module to describe the electric field in the volume of one pixel of the sensor at a back-bias voltage of 0. The electric-field map is adopted from [Sch23] and [Rog23b], and it was generated by so-called Technology Computer-Aided Design (TCAD)

simulations. The default size of the electric-field map is  $27 \times 27 \times 50 \ \mu\text{m}^3$  which is scaled to fit the  $29.24 \times 26.88 \times 50 \ \mu\text{m}^3$  volume of one pixel. Figure 3.1 shows the projection of the electric-field map on the x-axis. The electric field magnitude increases towards the collection volume.

### DopingProfileReader:

In order to model the recombination of e-h-pairs inside the active volume of a simulated sensor, the doping concentrations of the silicon in the sensor must be known. Therefore, the doping concentrations are used as input for the DopingProfileReader module. The doping concentrations can either be provided as a doping-concentration map similar to the electric-field map, or regions with a constant doping concentration can be specified. The doping concentrations in the sensors of the EPICAL-2 are  $N_{\rm A}=10^{13}\,{\rm cm}^{-3}$  in the epitaxial layer and  $N_{\rm A}=10^{18}\,{\rm cm}^{-3}$  in the substrate, as mentioned in section 2.1.3. To simulate this, two regions in the simulated sensor, each with the corresponding doping concentration, have been used as input for the DopingProfileReader in this simulation. Since the simulation of e-h-pair recombination is a new feature that was not available in Allpix<sup>2</sup> (v1.6.0), this module is only used in the implementation of the EPICAL-2 in Allpix<sup>2</sup> (v3.0.2).

#### DepositionGeant4:

The DepositionGeant4 module utilizes Geant4 to model the propagation and interaction of particles in the material of a simulated detector. The physical processes taken into account by Geant4 are specified in a so-called physics list. An important task of the DepositionGeant4 module is to generate e-h-pairs from the energy  $E_{\rm d}$  a charged particle deposits in a simulated sensor. For that purpose, the mean pair creation energy  $E_{\rm e-h} \approx 3.6\,{\rm eV}$  in silicon, and the so-called Fano factor F=-0.115, which takes into account fluctuations of the energy deposition due to lattice excitations, are used. The number of generated e-h-pairs is drawn from a Gaussian distribution with the mean  $E_{\rm d}/E_{\rm e-h}$  and the width  $\sqrt{F \cdot E_{\rm d}/E_{\rm e-h}}$ .

For this simulation, the physics list FTFP\_BERT\_EMZ is used. FTFP\_BERT is the default of Geant4, and the extension \_EMZ ensures that the most accurate modeling of electromagnetic physics processes available is used.

The source of primary particles is also specified as an input for the DepositionGeant4 module. For this simulation, the primary particles are generated inside a  $16 \times 16 \text{ mm}^2$  square centered 5 mm in front of the center of the active sensor area in layer 0. At the time of their generation, all primary particles travel parallel to the z-axis.

Several simulations have been performed of different particle types, energy E, and energy spread  $\sigma_{\rm E}$ . Table 3.2 provides an overview of all performed EPICAL-2 simulations in Allpix<sup>2</sup> (v3.0.2) with the corresponding simulated particles, primary-particle energy E, primary-particle energy spread  $\sigma_{\rm E}$ , and number  $N_{\rm Evt}$  of events.

| Particles             | E(GeV) | $\sigma_{ m E}$   | Events | Particles       | E  (GeV) | $\sigma_{ m E}$   | $N_{ m Evt}$ |
|-----------------------|--------|-------------------|--------|-----------------|----------|-------------------|--------------|
| e <sup>-</sup>        | 0.2    | 0                 | 20000  | e <sup>-</sup>  | 0.5      | 0                 | 20000        |
| $e^{-} \pi^{+} K^{+}$ | 1      | 0                 | 20000  | $e^- \pi^+ K^+$ | 2        | 0                 | 20000        |
| $p^+ \mu^+$           |        |                   |        | $p^+ \mu^+$     |          |                   |              |
| $e^-\pi^+K^+$         | 3      | 0                 | 20000  | $e^- \pi^+ K^+$ | 4        | 0                 | 20000        |
| $p^+ \mu^+$           |        |                   |        | $p^+ \mu^+$     |          |                   |              |
| $e^-\pi^+K^+$         | 5      | 0                 | 20000  | $e^- \pi^+ K^+$ | 5.8      | 0                 | 20000        |
| $p^+ \mu^+$           |        |                   |        | $p^+ \mu^+$     |          |                   |              |
| $e^-\pi^+K^+$         | 20     | 0                 | 10000  | $e^- \pi^+ K^+$ | 40       | 0                 | 10000        |
| $p^+ \mu^+$           |        |                   |        | $p^+ \mu^+$     |          |                   |              |
| $e^-\pi^+K^+$         | 60     | 0                 | 10000  | $e^- \pi^+ K^+$ | 80       | 0                 | 10000        |
| $p^+ \mu^+$           |        |                   |        | $p^+ \mu^+$     |          |                   |              |
| e <sup>-</sup>        | 200    | 0                 | 5000   | e <sup>-</sup>  | 500      | 0                 | 2000         |
| e <sup>-</sup>        | 1000   | 0                 | 1000   |                 |          |                   |              |
| e <sup>-</sup>        | 1      | $158\mathrm{MeV}$ | 20000  | e <sup>-</sup>  | 2        | $158\mathrm{MeV}$ | 20000        |
| e <sup>-</sup>        | 3      | $158\mathrm{MeV}$ | 20000  | e <sup>-</sup>  | 4        | $158\mathrm{MeV}$ | 20000        |
| e <sup>-</sup>        | 5      | $158\mathrm{MeV}$ | 20000  | e <sup>-</sup>  | 5.8      | $158\mathrm{MeV}$ | 20000        |
| e <sup>-</sup>        | 20     | $0.015 \cdot E$   | 10000  | e <sup>-</sup>  | 40       | $0.015 \cdot E$   | 10000        |
| e <sup>-</sup>        | 60     | $0.015 \cdot E$   | 10000  | e <sup>-</sup>  | 80       | $0.015 \cdot E$   | 10000        |

Table 3.2: Overview of the different primary particles, energies, energy spreads, and number of events simulated.

## GenericPropagation:

The GenericPropagation module models the movement of charge carriers generated via the DepositionGeant4 module through a simulated sensor. In this module, the movement of charge carriers is implemented as a superposition of random diffusion and drift according to the electric field provided by the ElectricFieldReader module. Since the movement of charge carriers is temperature-dependent, the temperature of the simulated sensor needs to be specified. The GenericPropagation module also models the recombination of e-h-pairs. Therefore, the doping concentrations provided by the DopingProfileReader module are utilized, and a specified recombination model simulates the e-h-pair recombination. The time span  $t_{\rm int}$  during which charge carriers are propagated inside the simulated sensor needs to be specified in the GenericPropagation module. The propagation of charge carriers either stops by e-h-pair recombination, reaching the surface of the sensor, or exceeding  $t_{\rm int}$ .

The time during which charge carriers propagate through the sensors in the EPICAL-2 is not known. Therefore,  $t_{\text{int}}$  is a simulation parameter that must be tuned for the simulation to accurately model the test-beam data. The tuning of  $t_{\text{int}}$  is discussed in section 3.2.

Since the sensors in the EPICAL-2 were kept at a stable temperature of  $20\,^{\circ}C$  during data taking, this temperature is also used in the simulation. For the simulation, the recombination model srh\_auger is used to achieve the most accurate simulation of e-h-pair

recombination available. To save computing resources, instead of single e-h-pairs, groups of 50 e-h-pairs are propagated.

In the previous implementation of the EPICAL-2 in Allpix<sup>2</sup> (v1.6.0), e-h-pair recombination is not modeled.

#### SimpleTransfer:

The SimpleTransfer module simulates the charge collection at the collection implants of a sensor. All charge carriers reaching a collection volume of the simulated sensor within the time period  $t_{\rm int}$  are assigned to the corresponding pixel. The charge carriers assigned to a pixel are summed up, and the value of the accumulated charge for each pixel is processed by the DefaultDigitizer module discussed next.

### DefaultDigitizer:

The DefaultDigitizer module simulates the front-end electronics of a sensor by translating the value of the accumulated charge in each pixel provided by the SimpleTransfer module into a digital signal. This works as follows: To simulate electronic noise in the front-end electronics, a noise level is drawn for each pixel from a Gaussian distribution with a standard deviation of  $\sigma_{\text{noise}}$ , and added to the accumulated charge. When the sum of accumulated charge and noise level is greater than a certain threshold level, a pixel hit is registered in the simulation. The threshold level in the simulation is drawn from a Gaussian distribution with the mean  $\mu_{\text{thr}}$  and a standard deviation  $\sigma_{\text{thr}}$  for each pixel. For this simulation, the following values, given in units of the electron charge e, are used:

$$\sigma_{\text{noise}} = 20 \,\mathrm{e}$$
 (3.1)

$$\sigma_{\rm thr} = 20 \,\mathrm{e} \tag{3.2}$$

$$\mu_{\text{thr}} = 82 \,\text{e} \tag{3.3}$$

These values are chosen since they are expected to correspond to the mean and standard deviation of the threshold of the pixels in the EPICAL-2.

## CaloOutputWriter:

The CaloOutputWriter module is specifically designed for the EPICAL-2 simulation. Via the CaloOutputWriter module, the pixel-hit information from the DefaultDigitizer module is stored in the same format as the data from the test-beam campaigns. For each pixel hit, three coordinates are stored: The sensor on which the pixel hit is located and the column and row coordinates, which refer to the position of a pixel hit on a sensor. In addition to the pixel-hit coordinates, in the simulation, it is also possible to store information about the energy, type, entering point, and exit point of particles traversing a simulated sensor. This additional particle information is stored for all simulations of primary electrons with an energy of  $1 \, \text{GeV} \leq E \leq 80 \, \text{GeV}$  and discarded for all other simulations to save disc

space.

In the reimplementation of the EPICAL-2 in Allpix<sup>2</sup> (v3.0.2), the CaloOutputWriter module is designed to support multithreading, which makes the EPICAL-2 simulation in Allpix<sup>2</sup> (v3.0.2) multithreading capable. Multithreading is not supported in the original implementation of the EPICAL-2 in Allpix<sup>2</sup> (v1.6.0).

## 3.2 Modeling the test-beam data

As mentioned in section 3.1, the simulation parameter  $t_{\text{int}}$  must be tuned for the simulation to model the test-beam data correctly. The simulation is tuned to the test-beam data at a primary-electron energy of 5 GeV since most events have been measured during data taking at this energy.

The tuning process for this Allpix<sup>2</sup> (v3.0.2) simulation is performed analog to the tuning process of the previous implementation of the EPICAL-2 in Allpix<sup>2</sup> (v1.6.0): First, the influence of  $t_{\rm int}$  on the following simulation performance characterizing observables is studied: the mean detector response, the standard deviation of the detector response, and the energy resolution. Second, the value of  $t_{\rm int}$  at which the simulation best describes the test-beam data is determined by several tests.

## 3.2.1 Influence of $t_{\text{int}}$

Figure 3.2 (top left) shows the mean  $\mu_{\rm Hit}$  ( $\mu_{\rm Clus}$ ) of the detector response, corresponding to the arithmetic mean value of the number  $N_{\rm Hit}$  of pixel hit distribution and number  $N_{\rm Clus}$  of cluster distribution, as a function of  $t_{\rm int}$ .  $\mu_{\rm Hit}$  increases approximately linearly with  $t_{\rm int}$  with a slope of approximately  $26\,{\rm ns}^{-1}$ , which corresponds to an increase of approximately  $46\,\%$  over the tested  $t_{\rm int}$  range.  $\mu_{\rm Clus}$  stayes constant within its statistical uncertainties at a value of  $\mu_{\rm Clus} \approx 334$  for  $25\,{\rm ns} < t_{\rm int} < 35\,{\rm ns}$ . From  $35\,{\rm ns} < t_{\rm int} < 43\,{\rm ns}$   $\mu_{\rm Clus}$  decreases to  $\mu_{\rm Clus} \approx 332$ , which corresponds to a decrease of approximately  $0.6\,\%$ . It is worth noting that the influence of  $t_{\rm int}$  on  $\mu_{\rm Hit}$  is approximately two orders of magnitude greater than its influence on  $\mu_{\rm Clus}$ .

Figure 3.2 (top right) shows the standard deviation  $\sigma_{\rm Hit}$  ( $\sigma_{\rm Clus}$ ) of the detector response, corresponding to the standard deviation of the  $N_{\rm Hit}$  ( $N_{\rm Clus}$ ) distribution, as a function of  $t_{\rm int}$ .  $\sigma_{\rm Hit}$  increases approximately linearly with  $t_{\rm int}$  with a slope of approximately 2.5 ns<sup>-1</sup>, which corresponds to an increase of approximately 41% over the tested  $t_{\rm int}$  range. Therefore,  $\sigma_{\rm Hit}$  behaves similarly to  $\mu_{\rm Hit}$  when variating  $t_{\rm int}$ .  $\sigma_{\rm Clus}$  stays constant within its statistical uncertainties at a value of  $\sigma_{\rm Clus} \approx 25$  for all tested  $t_{\rm int}$ . Therefore, variating  $t_{\rm int}$  influences  $\sigma_{\rm Hit}$  similarly to  $\mu_{\rm Hit}$  while  $t_{\rm int}$  has no significant influence on  $\sigma_{\rm Clus}$ .

Figure 3.2 (bottom) shows the energy resolution  $\sigma_{\rm Hit}/\mu_{\rm Hit}$  ( $\sigma_{\rm Clus}/\mu_{\rm Clus}$ ) as a function of  $t_{\rm int}$ . For pixel hits, the energy resolution decreases from  $\sigma_{\rm Hit}/\mu_{\rm Hit} \approx 10.6\,\%$  at  $t_{\rm int} = 25\,{\rm ns}$  to  $\sigma_{\rm Hit}/\mu_{\rm Hit} \approx 10.3\,\%$  at  $t_{\rm int} = 43\,{\rm ns}$ , which corresponds to a relative decrease of ap-

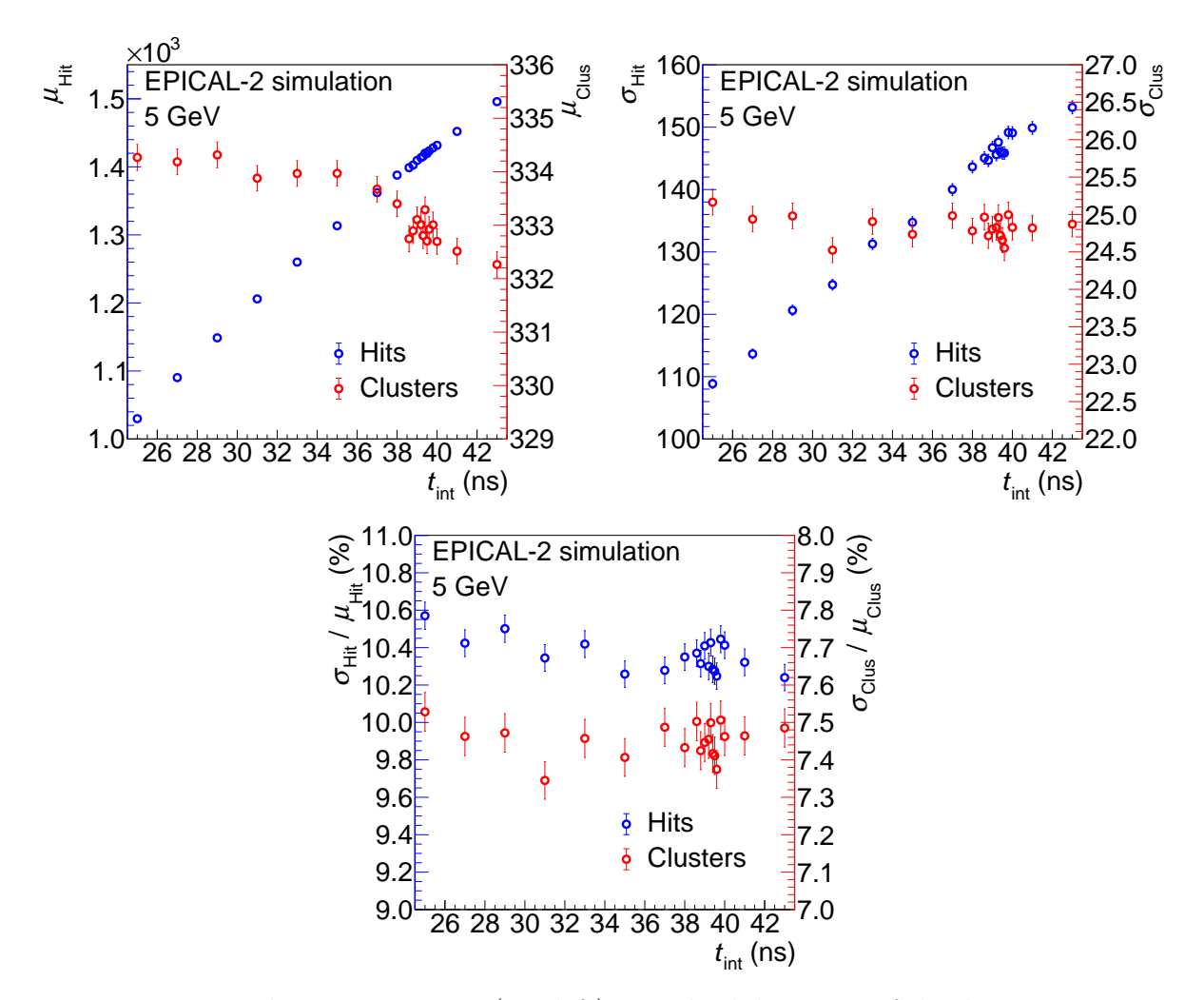


Figure 3.2: Mean detector response (top left), standard deviation of the detector response (top left), and energy resolution (bottom) as a function of  $t_{\text{int}}$  for the simulation at a primary-electron energy of 5 GeV.

proximately 3%. For clusters, the energy resolution stays constant within its statistical uncertainties at a value of  $\sigma_{\rm Clus}/\mu_{\rm Clus} \approx 7.45\%$  for all tested  $t_{\rm int}$ . Thus,  $t_{\rm int}$  has no significant influence on the energy resolution for clusters.

 $t_{\rm int}$  influences observables based on pixel hits but has almost no effect on observables based on clusters. Therefore, in this simulation,  $t_{\rm int}$  is tuned so that pixel-hit based observables are best described.

## 3.2.2 Tuning of $t_{int}$

To determine the value of  $t_{\rm int}$ , at which the simulation models the test-beam data most accurately, the  $N_{\rm Hit}$  distributions of the simulation and the test-beam data are compared via three comparison parameters: A  $\chi^2$  test yields the comparison parameter  $\chi^2_{\rm Hit}/{\rm NDF}$  and a Kolmogorov-Smirnov test yields the maximum Kolmogorov distance  $d_{\rm max,Hit}$  as a comparison parameter. The difference  $\mu_{\rm Hit,Sim.} - \mu_{\rm Hit,Data}$  of the mean number of pixel hits in the simulation and the test-beam data is used as the third comparison parameter.

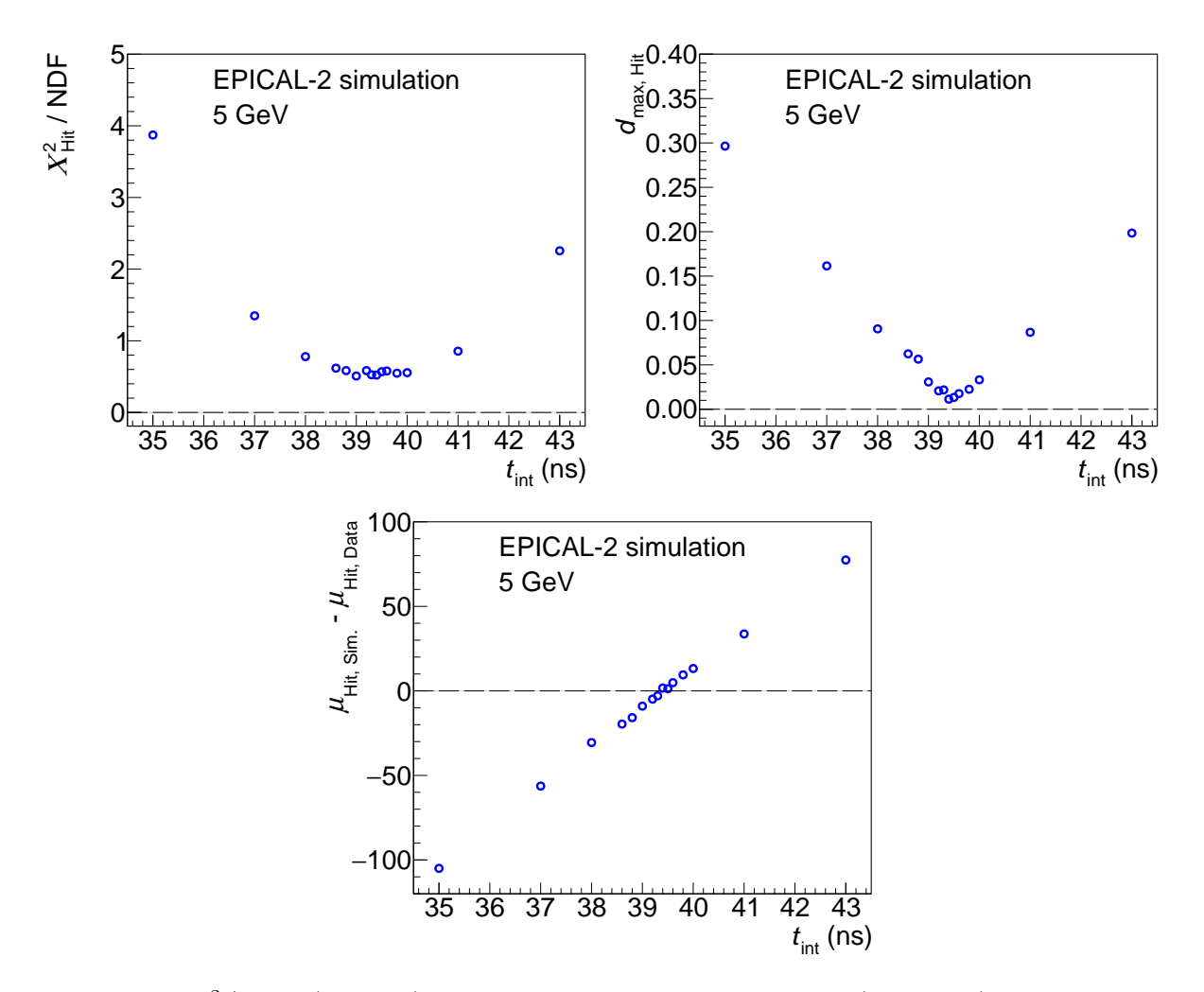


Figure 3.3:  $\chi^2/\text{NDF}$  (top left), maximum Kolmogorov distance (top right), and difference of the means (bottom) for the comparison of the  $N_{\text{Hit}}$  distributions of the test-beam data and simulation as a function of  $t_{\text{int}}$  at a primary-electron energy of 5 GeV.

Figure 3.3 (top left) shows  $\chi^2_{\rm Hit}/{\rm NDF}$  as a function of  $t_{\rm int}$ .  $\chi^2_{\rm Hit}/{\rm NDF}$  decreases by a factor of approximately 8 for 35 ns  $< t_{\rm int} < 39$  ns. For 39 ns  $< t_{\rm int} < 40$  ns the value of  $\chi^2_{\rm Hit}/{\rm NDF}$  stays constant at approximately 0.5. For 40 ns  $< t_{\rm int} < 43$  ns an increase of  $\chi^2_{\rm Hit}/{\rm NDF}$  by a factor of approximately 4 is observed.

Figure 3.3 (top right) shows the comparison parameter  $d_{\text{max,Hit}}$  as a function of  $t_{\text{int}}$ .  $d_{\text{max,Hit}}$  decreases linearly with a slope of approximately  $-0.066 \,\text{ns}^{-1}$  until a minimum of  $d_{\text{max,Hit}} \approx 0.01$  is reached at  $t_{\text{int}} = 39.4 \,\text{ns}$ . After reaching the minimum,  $d_{\text{max,Hit}}$  increases linearly with a slope of approximately  $0.056 \,\text{ns}^{-1}$ .

Figure 3.3 (bottom) shows the comparison parameter  $\mu_{\text{Hit,Sim.}} - \mu_{\text{Hit,Data}}$  as a function of  $t_{\text{int.}}$   $\mu_{\text{Hit,Sim.}} - \mu_{\text{Hit,Data}}$  increases linearly with a slope of approximately  $23 \, \text{ns}^{-1}$ . A value of  $\mu_{\text{Hit,Sim.}} - \mu_{\text{Hit,Data}} \approx 0$  is reached at  $t_{\text{int}} = 39.4 \, \text{ns}$ .

 $\chi^2_{\rm Hit}/{\rm NDF},\ d_{\rm max,Hit},\ {\rm and}\ |\mu_{\rm Hit,Sim.}-\mu_{\rm Hit,Data}|$  are minimal when the simulation models the test-beam data most accurately.  $\chi^2_{\rm Hit}/{\rm NDF}$  is minimal for 39 ns  $< t_{\rm int} < 40$  ns and both  $d_{\rm max,Hit}$  and  $|\mu_{\rm Hit,Sim.}-\mu_{\rm Hit,Data}|$  are minimal at  $t_{\rm int}=39.4$  ns. Therefore, a value of  $t_{\rm int}=39.4$  ns is used in the simulation.

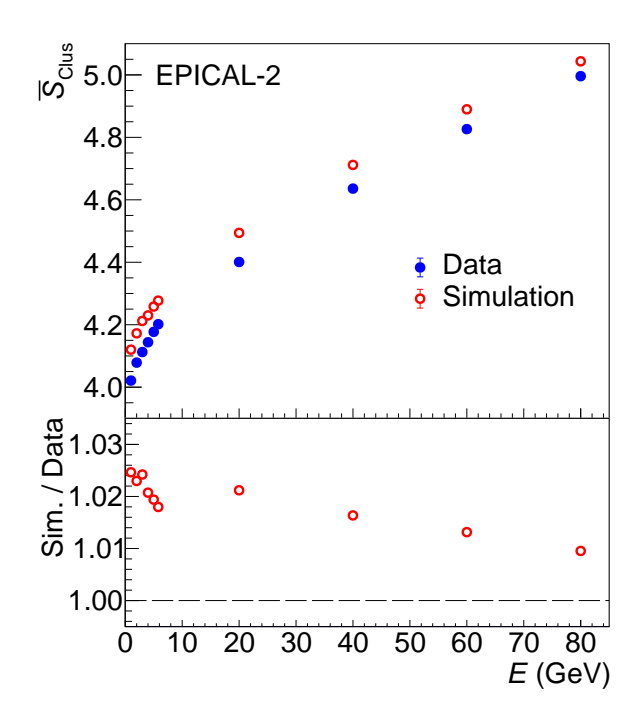


Figure 3.4: Average cluster size as a function of the primary-electron energy for the test-beam data and the simulation.

# 3.3 Simulation compared to test-beam data

To verify the correct modeling of the test-beam data by the simulation, the following calorimeter performance characterizing observables are compared between simulation and test-beam data: The mean number of pixels hits in a cluster, referred to as the mean cluster size  $\bar{S}_{\text{Clus}}$ , the mean detector response  $\mu_{\text{Hit}}$  ( $\mu_{\text{Clus}}$ ) for pixel hits and clusters, and the energy resolution  $\sigma_{\text{Hit}}/\mu_{\text{Hit}}$  ( $\sigma_{\text{Clus}}/\mu_{\text{Clus}}$ ) for pixel hits and clusters.

# 3.3.1 Cluster size

Figure 3.4 shows the mean cluster size  $\bar{S}_{\text{Clus}}$  for simulation and test-beam data as a function of the primary-electron energy E. For both simulation and test-beam data,  $\bar{S}_{\text{Clus}}$  increases with E from  $\bar{S}_{\text{Clus}} \approx 4$  at  $E=1\,\text{GeV}$  to  $\bar{S}_{\text{Clus}} \approx 5$  at  $E=80\,\text{GeV}$ . The energy-dependent increase of  $\bar{S}_{\text{Clus}}$  can be explained as follows: With increasing energy, the probability of two clusters merging into a larger cluster increases since the density of charged shower particles per sensor area rises. This effect is called cluster merging and is further discussed in sections 4.2. Compared to the test-beam data, the simulation overestimates  $\bar{S}_{\text{Clus}}$ . The deviation of  $\bar{S}_{\text{Clus}}$  in the simulation compared to the test-beam data decreases with E from approximately 2.5% at  $E=1\,\text{GeV}$  to approximately 1% at  $E=80\,\text{GeV}$ .

It is inferred that the simulation models  $\bar{S}_{\text{Clus}}$  of the test-beam data correctly within a margin of up to 2.5 %.

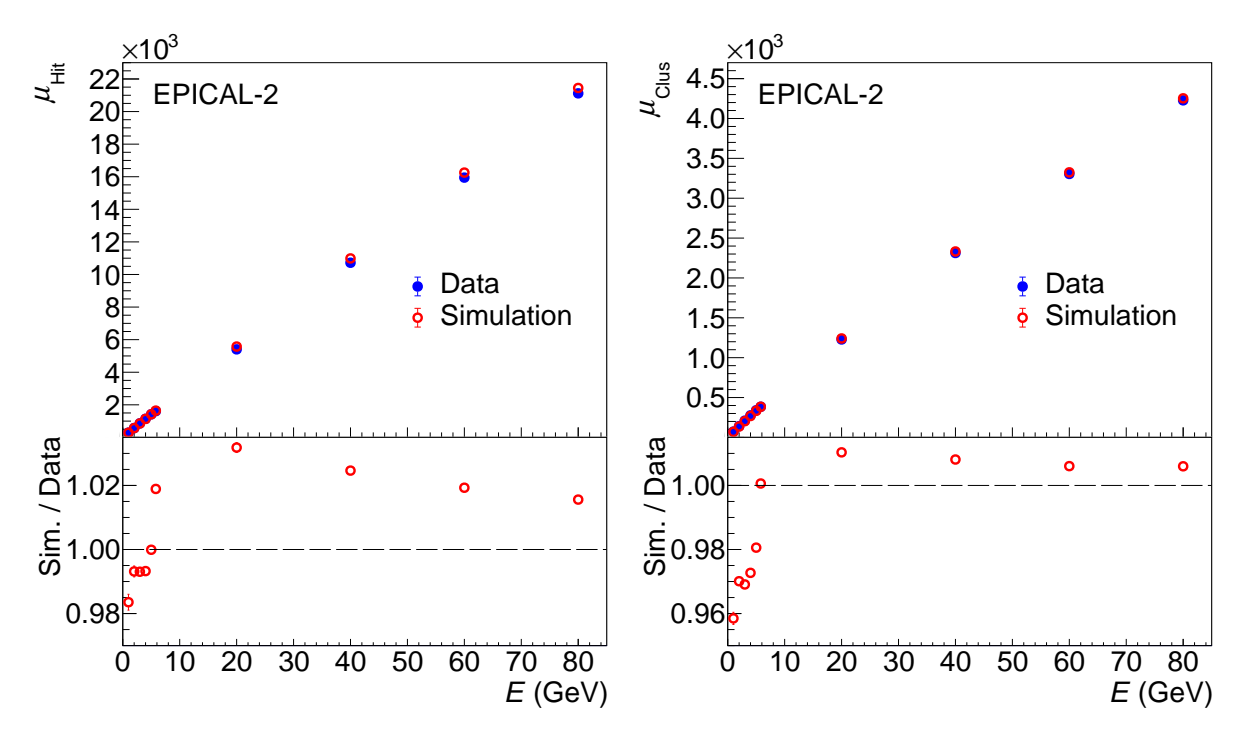


Figure 3.5: Mean detector response for pixel hits (left) and clusters (right) as a function of the primary-electron energy for the test-beam data and the simulation.

# 3.3.2 Detector response

Figure 3.5 (left) shows the mean detector response  $\mu_{\rm Hit}$  for pixel hits in the test-beam data and simulation as a function of the primary-electron energy E.  $\mu_{\rm Hit}$  increases, for both test-beam data and simulation, approximately linearly with a slope of approximately  $262\,{\rm GeV}^{-1}$ . For  $1\,{\rm GeV} \leq E \leq 4\,{\rm GeV}$  the simulation underestimates  $\mu_{\rm Hit}$  by up to  $2\,\%$ . At  $E=5\,{\rm GeV}$   $\mu_{\rm Hit}$  of the simulation and test-beam data are approximately equal since the  $N_{\rm Hit}$  distributions at  $E=5\,{\rm GeV}$  are used to tune the simulation. For  $5.8\,{\rm GeV} \leq E \leq 80\,{\rm GeV}$  the simulation overestimates  $\mu_{\rm Hit}$  by up to  $3\,\%$ .

Figure 3.5 (right) shows the mean detector response  $\mu_{\text{Clus}}$  for clusters in the simulation and test-beam data as a function of the primary-electron energy E. Similar to  $\mu_{\text{Hit}}$ ,  $\mu_{\text{Clus}}$  increases, for both test-beam data and simulation, approximately linearly with a slope of approximately  $52\,\text{GeV}^{-1}$ . For  $1\,\text{GeV} \leq E \leq 5\,\text{GeV}$  the simulation underestimates  $\mu_{\text{Clus}}$  by up to  $4\,\%$ . For  $5.8\,\text{GeV} \leq E \leq 80\,\text{GeV}$  the simulation overestimates  $\mu_{\text{Clus}}$  by up to  $1\,\%$ .

It is found that the simulation correctly models the test-beam data regarding the observable  $\mu_{\text{Hit}}$  within a margin from  $-2\,\%$  to  $3\,\%$  and the observable  $\mu_{\text{Clus}}$  within a margin from  $-4\,\%$  to  $1\,\%$ .

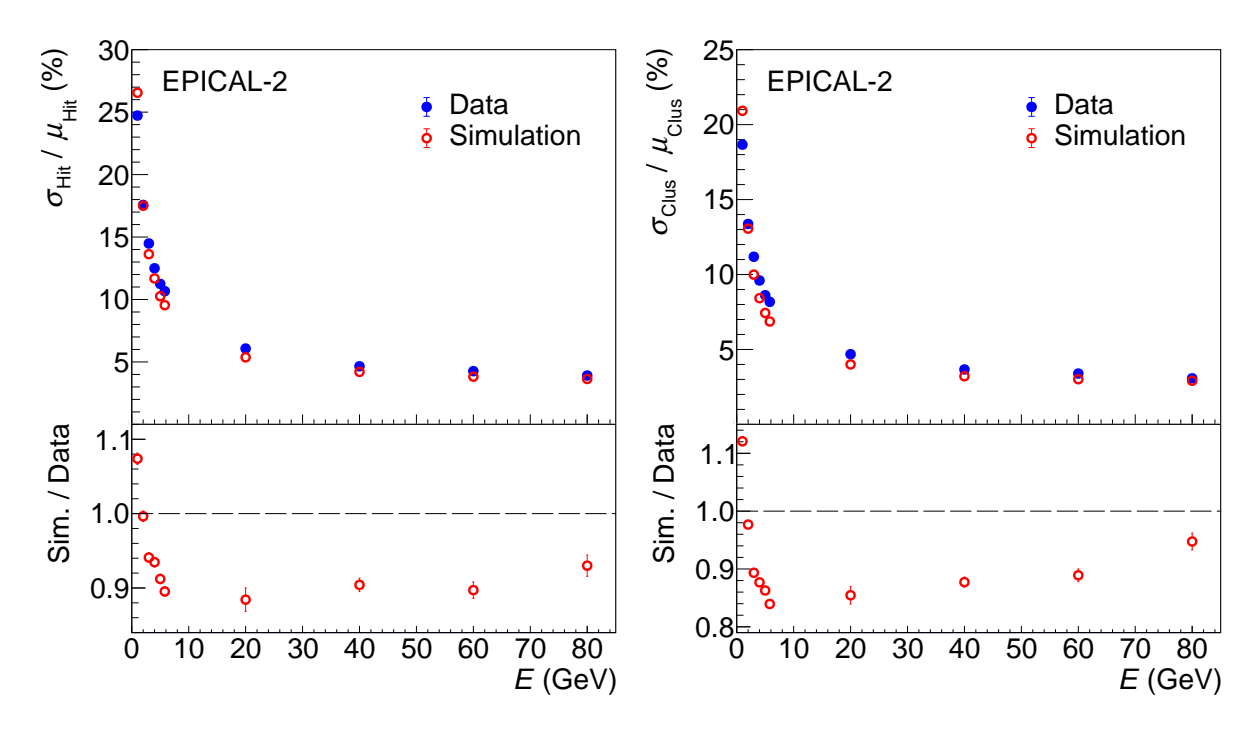


Figure 3.6: Energy resolution for pixel hits (left) and clusters (right) as a function of the primary-electron energy for the test-beam data and the simulation.

# 3.3.3 Energy resolution

Figure 3.6 (left) shows the energy resolution for pixel hits in the test-beam data and simulation as a function of the primary-electron energy E. In both test-beam data and simulation, the energy resolution for pixel hits decreases with E. This behavior is expected for an electromagnetic calorimeter since the statistical fluctuations of the number of charged shower particles decrease with the primary-electron energy. The simulation overestimates the energy resolution for pixel hits at  $E = 1 \,\text{GeV}$  by approximately 8%. For  $2 \,\text{GeV} \le E \le 80 \,\text{GeV}$  the simulation underestimates the energy resolution for pixel hits by up to 12%.

Figure 3.6 (right) shows the energy resolution for clusters in the test-beam data and simulation as a function of the primary-electron energy E. In both test-beam data and simulation, the energy resolution for clusters decreases with E, similar to the energy resolution for pixel hits. Also similar to pixel hits, the simulation overestimates the energy resolution for clusters at  $E = 1 \,\text{GeV}$  by approximately 11%. At all other mean primary-electron energies, the simulation underestimates the energy resolution for pixel hits by up to 16%.

The simulation is found to accurately replicate the energy resolution of pixel hits from the test-beam data within a range of -12% to 8%, and the energy resolution of clusters within a range of -16% to 11%.

| Observable                       | relative deviation $\Delta_{\text{Sim}}$ (%) |                           |     |  |  |
|----------------------------------|--|---------------------------|-----|--|--|
| $\bar{S}_{ m Clus}$              | 1  | $<\Delta_{\mathrm{Sim}}<$ | 2.5 |  |  |
| $\mu_{ m Hit}$                   | -2   | $<\Delta_{\mathrm{Sim}}<$ | 3   |  |  |
| $\mu_{	ext{Clus}}$               | -4   | $<\Delta_{\mathrm{Sim}}<$ | 1   |  |  |
| $\sigma_{ m Hit}/\mu_{ m Hit}$   | -12  | $<\Delta_{\mathrm{Sim}}<$ | 8   |  |  |
| $\sigma_{ m Clus}/\mu_{ m Clus}$ | -16  | $<\Delta_{\rm Sim}<$      | 11  |  |  |

Table 3.3: Overview of deviations of the simulation from the test-beam data of the EPICAL-2 for several observables.

Table 3.3 summarizes the simulation's relative deviations to the test-beam data for different observables. The simulation models, the observables  $\bar{S}_{\text{Clus}}$ ,  $\mu_{\text{Hit}}$ , and  $\mu_{\text{Clus}}$  with maximum deviation to the corresponding observables in the test-beam data of 4%. The deviations between the simulation and the test-beam data regarding the resolution for pixel hits and clusters are in the order of 10%.

# 3.4 Simulation of an enlarged EPICAL-2

In the context of this thesis, a simulation of an enlarged version of the EPICAL-2, called EPICAL-2L, is implemented in Allpix<sup>2</sup>. The scope of analyses with the EPICAL-2L simulation is the study of the influence of leakage effects on the performance of the EPICAL-2, by comparing the EPICAL-2 simulation to the EPICAL-2L simulation, which is presented in section 5.5. This section describes the implementation of the EPICAL-2L.

For the simulation of the EPICAL-2L, the simulation chain of the EPICAL-2 is used as a basis. In most modules of Allpix<sup>2</sup>, no changes are made when transitioning from the EPICAL-2 to the EPICAL-2L simulation. Exceptions are the GeometryBuilderGeant4 module and the CaloOutputWriter module.

In the GeometryBuilderGeant4 module, the geometry of the EPICAL-2L is defined. Table 3.4 presents an overview of the components of the EPICAL-2L, exemplary for layer 0. For every consecutive layer the coordinate  $z_{\rm pos}$  increases by 3.5 mm. Other than the EPICAL-2, which features 24 identical layers, the EPICAL-2L features 96 identical layers, increasing depth by a factor of 4. In the z-direction, every layer of the EPICAL-2L is constructed the same as the EPICAL-2. In the lateral plane, every component of the EPICAL-2L is increased in size by a factor of 4 compared to the EPICAL-2, with the exception of the gap between the two simulated sensors in a layer, which is kept at a width of 100  $\mu$ m. The total volume of the EPICAL-2L is increased by a factor of 64 compared to the EPICAL-2.

On each simulated sensor of the EPICAL-2L, the pixel pitch is the same as in the EPICAL-2. The number of pixels of the simulated sensors in the EPICAL-2L is increased by a factor of 4 in each direction compared to the sensors of the EPICAL-2, leading to 4096 columns and 2048 rows of pixels.

| Component     | Material | $x_{\rm pos}({\rm mm})$             | $y_{\rm pos}({\rm mm})$             | $z_{\rm pos}({\rm mm})$ |  |
|---------------|----------|-------------------------------------|-------------------------------------|-------------------------|--|
| Component     | Type     | $x_{\rm size}$                      | $y_{ m size}$                       | $z_{ m size}$           |  |
| Sensor A      | Silicon  | 0                                   | 0                                   | 0                       |  |
| Selisor A     | Active   | $4096 \times 29.24  \mu \text{m}$   | $2048 \times 26.88  \mu \mathrm{m}$ | 55 μm                   |  |
| Sensor B      | Silicon  | 0                                   | -55.15024                           | 0                       |  |
| Selisor D     | Active   | $4096 \times 29.24  \mu \mathrm{m}$ | $2048 \times 26.88  \mu \text{m}$   | 55 μm                   |  |
| Can           | Silicon  | 0                                   | -27.57512                           | 0                       |  |
| Gap           | Passive  | $4096 \times 29.24  \mu \text{m}$   | 100 μm                              | $55\mu\mathrm{m}$       |  |
| Excess left   | Silicon  | 0                                   | -85.09136                           | 0                       |  |
| Excess leit   | Passive  | $4096 \times 29.24  \mu \mathrm{m}$ | $4832\mu\mathrm{m}$                 | 55 μm                   |  |
| Evenes right  | Silicon  | 0                                   | 29.94112                            | 0                       |  |
| Excess right  | Passive  | $4096 \times 29.24  \mu \mathrm{m}$ | $4832\mu\mathrm{m}$                 | 55 μm                   |  |
| Evenes top    | Silicon  | 59.94352                            | -27.57512                           | 0                       |  |
| Excess top    | Passive  | 120 μm                              | 119.86448 mm                        | 55 μm                   |  |
| Excess bottom | Silicon  | -59.94352                           | -27.57512                           | 0                       |  |
| Excess bottom | Passive  | 120 μm                              | 119.86448 mm                        | $55\mu\mathrm{m}$       |  |
| Chip cable A  | Kapton   | 0                                   | -27.57512                           | -0.0425                 |  |
| Chip cable A  | Passive  | 124 mm                              | 128 mm                              | 30 μm                   |  |
| Chin sabla D  | Aluminum | 0                                   | -27.57512                           | -0.0725                 |  |
| Chip cable B  | Passive  | 124 mm                              | 128 mm                              | 30 μm                   |  |
| Layer cable   | Kapton   | 0                                   | -27.57512                           | -0.2175                 |  |
| Layer cable   | Passive  | 124 mm                              | 160 mm                              | 145 μm                  |  |
| Absorber      | Tungsten | 0                                   | -27.57512                           | 1.53                    |  |
|               | Passive  | 160 mm                              | 140 mm                              | $3  \mu \mathrm{m}$     |  |
| Spacer A      | Tungsten | 72                                  | -27.57512                           | -0.22                   |  |
|               | Passive  | 16 mm                               | $140\mathrm{mm}$                    | $0.5\mu\mathrm{m}$      |  |
| Spacer B      | Tungsten | -72                                 | -27.57512                           | -0.22                   |  |
| Spacer D      | Passive  | 16 mm                               | 140 mm                              | $0.5\mathrm{\mu m}$     |  |

Table 3.4: Overwiev of the implementation of the components of the EPICAL-2L in GeometryBuilderGeant4, exemplary for layer 0.

The CaloOutputWriter module is modified for the simulation of the EPICAL-2L to accommodate the storage of pixel-hit information on larger simulated sensors and additional layers.

# Chapter 4

# Data analysis

The EPICAL-2's performance is influenced by several effects. Therefore, multiple corrections and selections are applied to the data sets in this analysis to address these performance-influencing effects. Furthermore, a clustering algorithm is necessary to reconstruct clusters of pixel hits. In addition, the behavior of the EPICAL-2 may vary over one data-taking campaign. To verify the uniform behavior of the EPICAL-2 between runs taken at a given primary-electron energy, a run quality analysis is performed in this analysis, which is crucial to avoid an influence on the EPICAL-2's performance from inconsistencies between runs. This chapter presents the data sets, clustering, corrections, selections, and run-quality analysis. For clustering, corrections, and selections, a framework dedicated to the analysis of EPICAL-2 data was developed in the scope of [Alm23] and [Rog23a], which is utilized in this thesis.

# 4.1 Data sets

During the measurement campaigns with the EPICAL-2 at the DESY and CERN-SPS test-beam facilities, several so-called runs were recorded. A run refers to a period of consecutive data-taking with constant detector and beam settings.

Table 4.1 presents all runs recorded with the EPICAL-2 that are relevant to this thesis. Additionally, table 4.1 gives an overview of the energy of the test beam and the number of events in each run. Except for changing the test-beam energy, all runs were recorded with the same settings of the EPICAL-2, except the back-bias voltage setting. Most runs were recorded with no back-bias voltage  $V_{\rm BB}=0\,\rm V$  applied to the sensors in the EPICAL-2. An exception are the runs highlighted in blue in table 4.1, during which the back-bias voltage was set to  $V_{\rm BB}=3\,\rm V$  for the sensors in even-numbered layers of the EPICAL-2 and  $V_{\rm BB}=0\,\rm V$  for the sensors in odd-numbered layers of the EPICAL-2. The changes in the back-bias voltage of the sensors were performed to compare the performance of the EPICAL-2 with and without back-bias voltage, which is presented in section 5.3. During the data taking, the right-side sensor in layer 21 of the EPICAL-2 was defective

| DESY | measurement                  | campagin | CERN-SPS | 3 measuremen                 | t campagin |
|------|------------------------------|----------|----------|------------------------------|------------|
| Run  | $E\left(\mathrm{GeV}\right)$ | Events   | Run      | $E\left(\mathrm{GeV}\right)$ | Events     |
| 1250 | 5                            | 522000   | 2951     | 20                           | 401        |
| 1251 | 3                            | 522000   | 2956     | 20                           | 375        |
| 1252 | 1                            | 522000   | 2960     | 20                           | 2666       |
| 1253 | 4                            | 82500    | 2963     | 20                           | 5748       |
| 1257 | 4                            | 522000   | 2964     | 80                           | 25800      |
| 1260 | 2                            | 522000   | 2965     | 80                           | 25625      |
| 1261 | 5                            | 522000   | 2966     | 80                           | 64388      |
| 1262 | 3                            | 244501   | 2967     | 80                           | 41081      |
| 1263 | 1                            | 522000   | 2970     | 80                           | 52397      |
| 1274 | 4                            | 522000   | 2971     | 80                           | 47640      |
| 1276 | 2                            | 522000   | 2972     | 80                           | 54000      |
| 1308 | 5                            | 294000   | 2973     | 80                           | 67266      |
| 1309 | 5.8                          | 141527   | 2974     | 60                           | 21437      |
| 1310 | 5.8                          | 277880   | 2975     | 60                           | 6271       |
| 1333 | 5                            | 295500   | 2977     | 60                           | 33976      |
| 1335 | 3                            | 297000   | 2978     | 60                           | 50200      |
| 1336 | 1                            | 594000   | 2979     | 40                           | 58354      |
| 1337 | 2                            | 594000   | 2980     | 40                           | 77447      |
| 1338 | 4                            | 297000   | 2983     | 40                           | 7698       |
| 1339 | 5                            | 747000   | 2985     | 40                           | 34384      |
| 1341 | 3                            | 747000   | 2988     | 40                           | 59461      |
| 1343 | 1                            | 744000   | 2992     | 80                           | 92952      |
| 1344 | 2                            | 735000   | 2993     | 80                           | 85001      |
| 1345 | 4                            | 744000   | 2995     | 60                           | 42639      |
| 1346 | 5.8                          | 617749   | 2997     | 20                           | 514        |
| 1375 | 5.8                          | 391733   | 2998     | 20                           | 3720       |
| 1376 | 5.8                          | 89798    | 2999     | 20                           | 2925       |
| 1413 | 5                            | 1103742  | 3000     | 20                           | 3625       |
|      |                              |          | 3001     | 20                           | 3516       |
|      |                              |          | 3007     | 20                           | 55         |
|      |                              |          | 3118     | 60                           | 22209      |
|      |                              |          | 3123     | 20                           | 18618      |
|      |                              |          | 3124     | 20                           | 5175       |
|      |                              |          | 3125     | 40                           | 19621      |

Table 4.1: Overview of the data recorded with the EPICAL-2 during the DESY and CERN-SPS measurement campaigns. The runs highlighted in blue were recorded with different settings.

and, therefore, disabled in all runs. Additionally, in the runs highlighted in blue in table 4.1, the left-side sensor in layer 2 of the EPICAL-2 was excluded due to errors occurring during readout.

# 4.2 Clustering

The number  $N_{\text{Hit}}$  of pixel hits and the number  $N_{\text{Clus}}$  of pixel-hit clusters is studied in this work. Therefore, a clustering of pixel hits is performed in test-beam data and simulation. A charged particle traversing a sensor usually generates multiple adjacent pixel hits due to charge sharing between pixels. To gain accurate information on the location of the particle traversing a sensor from the location of the pixel hits, a clustering of adjacent pixel hits is performed in this analysis. The cluster information is used for multiple corrections, event selection, and quantifying the detector response.

In this analysis, a cluster is defined as an ensemble of pixel hits that are adjacent to each other along their edges or corners. For the purpose of reconstructing clusters, in this thesis, a so-called DBSCAN clustering algorithm [Est96] is adopted from [Alm23], which works as follows: An arbitrary pixel hit is defined as a starting point for a cluster. Then, all pixel hits adjacent to this cluster are successively added to the cluster until no further adjacent pixel hit exists. After that, the cluster is complete, and all the pixel hits contained in the cluster are excluded from the further clustering processes. These algorithm steps are repeated with a new arbitrary pixel hit as a cluster starting point until all pixel hits in an event have been assigned to a cluster. The clustering algorithm is applied sensor-by-sensor; i.e., a cluster is never formed across the gap between the two sensors per layer.

Typically, a single charged particle traversing the sensor results in a single cluster. In the case of a sufficiently high charged-particle density per sensor area, multiple particles may result in a single cluster. This effect is called cluster merging.

# 4.3 Corrections

Performance-influencing effects are addressed by several corrections in the following way and are presented in this section:

Faulty pixels  $\rightarrow$  Pixel masking

Sensor-placement deviations  $\rightarrow$  Alignment correction

Placement deviations of the EPICAL-2  $\rightarrow$  Inclination correction

Non uniform sensor sensitivity  $\rightarrow$  Calibration

# 4.3.1 Pixel masking

Over 99% of the sensor's pixels in the EPICAL-2 operate normally. Despite that, two types of faulty pixels may be observed: dead and noisy. Dead pixels show no hits or significantly fewer hits than functional pixels under the same circumstances. Noisy pixels

generate more hits compared to functional pixels under the same conditions. To ensure optimal performance results of the EPICAL-2, a pixel mask is adopted from [Alm23], which masks faulty pixels in this analysis.

To generate the pixel mask, in [Alm23], faulty pixels are identified in three steps: First, an internal testing function of the sensor is utilized, where test signals are injected directly into the front-end electronics of each pixel in a row of pixels, and then the entire sensor is read out. This is repeated for all rows in a sensor. Pixels that do not respond to the test signal are classified as dead, and pixels that register hits even without a test signal injected are classified as noisy. Second, pedestal runs of the EPCIAL-2, which are measurements without any beam, are used to further identify noisy pixels. As there is no beam, every pixel hit in a pedestal run results from noise. If a pixel generates a hit in more than every thousandth event in a pedestal run, it is classified as noisy. Third, test-beam measurements are used to further identify dead pixels. If a pixel shows, on average over all events, significantly fewer hits than the average number of pixel hits in its 32 by 32 matrix of neighboring pixels, it is classified as dead. Furthermore, entire columns of pixels that show, on average over all events, significantly fewer hits than neighboring columns are classified as dead.

Besides dead and noisy pixels, each sensor's outermost columns and rows have been masked because they show significantly fewer hits than the rest of the sensor. This is due to a guard ring that surrounds the pixel matrix. In total, 0.95% of all pixels in the EPICAL-2 are masked in this analysis.

The pixel masking is performed before the clustering and, therefore, has an influence on the number and size of reconstructed clusters: The presence of masked pixels can lead to multiple clusters induced by a single charged particle.

# 4.3.2 Alignment and inclination

To fully utilize the excellent position resolution of the sensors in the EPICAL-2, any effects that distort the position of pixel hits or clusters must be corrected. The alignment correction and the inclination correction achieve this.

## Alignment correction:

The accuracy of the sensor placement in the EPICAL-2 is larger than the pixel pitch of the sensors. To determine the precise location of pixel hits or clusters, the position of every sensor must be known with an accuracy comparable to the pixel pitch of the sensor. Each sensor can be assigned six degrees of freedom: three spatial coordinates and three rotation angles. The tungsten absorbers of the EPICAL-2 constrain the position of the sensors in the z-direction; i.e., it is assumed that no correction along the z-axis and the two angles, opening in the x-z and y-z directions, are needed. Three degrees of freedom in which a sensor can be displaced from its nominal position are left: a displacement along the x- and y-axis and a rotation around the z-axis. Displacements along these degrees

of freedom are corrected in this analysis by shifting each pixel hit by  $\Delta x$  and  $\Delta y$  on the x-y-plane and rotating each pixel-hit position by  $\Delta \Theta$  around the z-axis.  $\Delta x$ ,  $\Delta y$ , and  $\Delta \Theta$  are refferred to as alignment parameters.

The alignment parameters are unique for every sensor in the EPICAL-2 and are adopted from [Alm23] to be used in this thesis. In [Alm23],  $\Delta x$ ,  $\Delta y$ , and  $\Delta \Theta$  are determined by a data-driven approach that uses cosmic-muon events. Muons traverse the EPICAL-2 in a straight line, typically generating a cluster in each layer. Therefore, the cluster positions are parameterized in each cosmic-muon event by a straight line, and the mean over all cosmic-muon events of the parameterization's  $\chi^2$  is calculated. The alignment parameters for each sensor are varied iteratively until a minimum mean  $\chi^2$  and stable alignment parameters are reached.

This  $\chi^2$  minimization procedure is performed in three steps. First, the sensors on the left and right sides of the EPICAL-2 are aligned separately. Second, the alignment parameters of the sensors on one side of the EPICAL-2 are fixed. The sensors on the other side of the EPICAL-2 are aligned relative to the sensors with fixed alignment parameters using events where a muon crosses the gap in the x-direction between the sensors in the EPICAL-2. Third, all sensors are aligned simultaneously using all cosmic-muon events. When the alignment corrections are applied, the deviations from cluster positions in cosmic-muon events to a straight-line parameterization are reduced from several 100  $\mu$ m to below 5  $\mu$ m [Alm23].

## Inclination correction:

Besides the positioning of the sensors in the EPICAL-2, the orientation of the EPICAL-2 in the beam line must be known. In this thesis, the beam angle  $\phi_0$  is defined as the angle between the test beam and the z-axis of the EPICAL-2. Although the EPICAL-2 was carefully aligned in the beam line,  $\phi_0$  deviates from 0°. The results of the event selection and the analysis presented in 5.4 are sensitive to deviations from  $\phi_0$ . These deviations are corrected in this analysis by shifting the position of all pixel hits and clusters along the x- and y-axis according to so-called inclination functions [Rog23a]:

$$f_{\text{incl,x,y}}(z) = m \cdot (z - 0.028 \,\text{mm})$$
 (4.1)

For each setup at a test-beam facility, two inclination functions are used: one that shifts pixel hits in the x-direction and one that shifts pixel hits in the y-direction. The inclination functions for the DESY data have been adopted from [Alm23]. They are determined by parametrizing the 2D distribution of pixel hits in the x-y-plane in every layer with  $f_{\text{lat}}(x, y)$ , defined in the following way [Rog23a]:

$$f_{\text{lat}}(x,y) = \frac{A}{r} \cdot exp(B \cdot r)$$
 (4.2)

$$r = \sqrt{C + (x - \mu_{\rm x})^2 + (y - \mu_{\rm y})^2}$$
 (4.3)

| E  (GeV) | m (x-direction) | m (y-direction) |
|----------|-----------------|-----------------|
| 1        | -0.0064427      | 0.0033934       |
| 2        | -0.0064427      | 0.0033934       |
| 3        | -0.0064427      | 0.0033934       |
| 4        | -0.0064427      | 0.0033934       |
| 5        | -0.0064427      | 0.0033934       |
| 5.8      | -0.0064427      | 0.0033934       |
| 20       | -0.0067649      | 0.0011863       |
| 40       | -0.0067349      | 0.0011785       |
| 60       | -0.0067286      | 0.0011876       |
| 80       | -0.0067199      | 0.0012692       |

Table 4.2: Overview of parameter m of the inclination function used in this analysis to correct the data.

 $A, B, C, \mu_x$  and  $\mu_y$  are free parameters.  $\mu_x$  and  $\mu_y$  correspond to the x-y-position of the maximum of  $f_{\text{lat}}(x, y)$ . Both  $\mu_x$  and  $\mu_y$  as a function of the layer number are then parametrized each with  $f_{\text{incl},x,y}(z)$ . The inclination functions for the CERN-SPS data have been adopted from [Rog23a]. They are determined by studying events from the CERN-SPS data, where hadrons or muons have crossed the EPICAL-2 in a straight line without showering. For these events, the position differences  $\Delta_x$  and  $\Delta_y$  in x and y direction of all pixel hits in a layer from the beam impact position, defined as the position of a single cluster in layer 0, is calculated. The distributions of  $\Delta_x$  and  $\Delta_y$  are parametrized each with  $f_{\text{Gauss},x,y}(\Delta_{x,y})$ , defined as follows:

$$f_{\text{Gauss,x,y}}(\Delta_{\text{x,y}}) = A_{\text{x,y}} + B_{\text{x,y}} \cdot \exp\left[-\frac{1}{2}\left(\frac{\Delta_{\text{x,y}} - \mu_{\text{x,y}}}{\sigma_{\text{x,y}}}\right)^{2}\right]$$
(4.4)

 $A_{x,y}$ ,  $B_{x,y}$ ,  $\mu_{x,y}$ , and  $\sigma_{x,y}$  are free parameters. The parameter  $\mu_{x,y}$  corresponds to the maximum value of  $f_{Gauss,x,y}(\Delta_{x,y})$ . The values  $\mu_x$  and  $\mu_y$  as functions of the layer are then parametrized each with  $f_{incl,x,y}(z)$ . Table 4.2 presents the parameters of  $f_{incl,x,y}(z)$ .

# 4.3.3 Calibration

The amount of collected charge necessary to induce a signal over the digitization threshold is unique for every sensor. Therefore, the sensitivity differs between the sensors in the EPICAL-2, resulting in fluctuations in the number of pixel hits induced by a single charged particle traversing different sensors in the EPICAL-2. These fluctuations influence the EPICAL-2's performance. Therefore, all sensors are calibrated in this analysis to achieve a uniform sensitivity across sensors. The calibration is performed by weighting every pixel hit with a sensor-specific calibration factor  $C_{\rm s}$ . The calibration factors used in this analysis are adopted from [Alm23]. They are determined by analyzing cosmic-muon events based on the assumption that the number of charge carriers liberated by a cosmic muon is the same in all sensors the muon traverses. In each cosmic-muon event, straight-line

parameterizations of the cluster positions are performed 24 times, each time excluding a different layer of the EPICAL-2. The response  $N_{\rm Hit,S}^{\rm Cos}$  of a single sensor S to a cosmic muon is defined as the number of pixel hits inside a 3 mm radius around the straight-line parameterization that excludes sensor S. The calibration factors are calculated in the following way:

$$C_{\rm s} = \frac{\bar{\mu}_{\rm Hit}^{\rm Cos}}{\mu_{\rm Hit.S}^{\rm Cos}} \tag{4.5}$$

where  $\mu_{\rm Hit,S}^{\rm Cos}$  is the mean over all cosmic-muon events of  $N_{\rm Hit,S}^{\rm Cos}$  and  $\bar{\mu}_{\rm Hit}^{\rm Cos}$  is the mean over all sensors of  $\mu_{\rm Hit,S}^{\rm Cos}$ .

# 4.4 Selections

To ensure that the calorimeter performance is not impacted by contamination of the data set with multi-electron- and hadron-events, in this analysis, a clean sample of single-electron events is selected from the test-beam data. Several algorithms described in this section accomplish the single-electron-event selection.

# 4.4.1 Event selection for DESY data

Due to the high beam rate at DESY, it is possible that more than one electron enters the EPICAL-2 during one strobe length. In such events, the detector response is increased compared to single-electron events. It is also possible that electrons hit the EPICAL-2 at the edges of the active sensor area in layer 0. In such events, a significant part of the electromagnetic shower leaks out of the EPICAL-2 in the lateral direction, and the detector response is decreased compared to events of electrons hitting the center of the active sensor area in layer 0.

For this analysis, only events where a single electron enters the EPICAL-2 in a fiducial region, corresponding to a  $16 \times 16 \,\mathrm{mm^2}$  square centered in the active sensor area in layer 0, are selected. This ensures that only one electromagnetic shower is contained inside the EPICAL-2 in every event.

For the DESY data, the event selection in this analysis is adopted from [Alm23], where it is accomplished by an anti- $k_t$  jet clustering algorithm explained in detail in [Cac08]. The algorithm works as follows: The EPICAL-2 is divided in the x-y-projection into cells of size  $0.5 \times 0.5 \,\mathrm{mm}^2$  in the center of the EPICAL-2 ( $|x| < 12 \,\mathrm{mm}$  and  $|y| < 12 \,\mathrm{mm}$ ) and  $1 \times 1 \,\mathrm{mm}^2$  in the outer region ( $|x| > 12 \,\mathrm{mm}$  and  $|y| > 12 \,\mathrm{mm}$ ). Then, the clusters in an event are assigned to the cells according to their x-y-position, and so-called pseudo-jets are formed from cells containing clusters from at least three layers. The parameters from

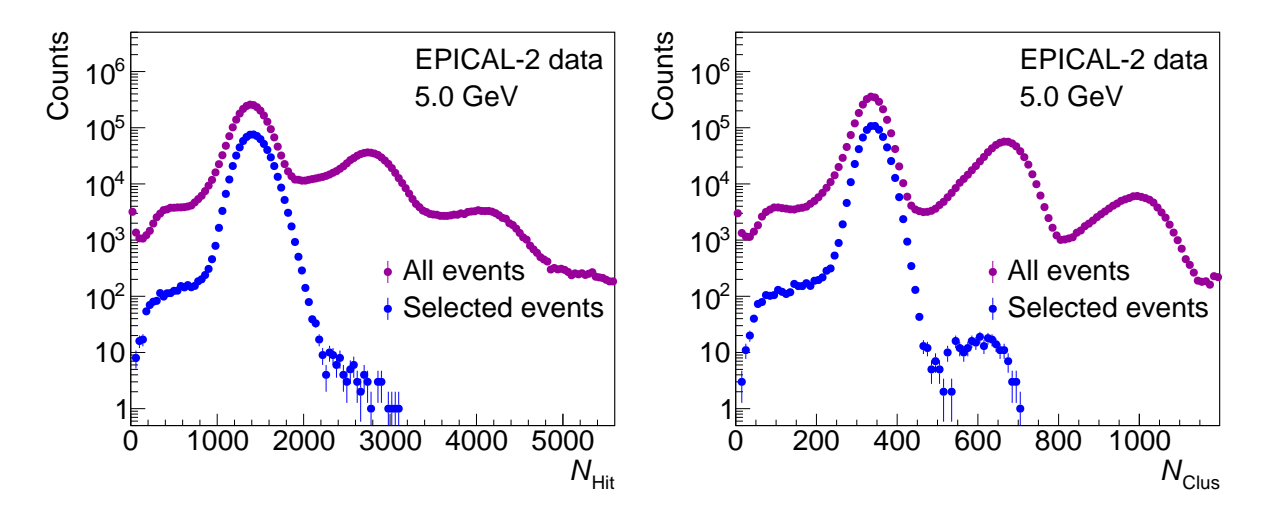


Figure 4.1: Distributions of  $N_{\text{Hit}}$  (left) and  $N_{\text{Clus}}$  (right) for all events and selected events of electrons with an average energy of 5 GeV.

the cell c correspond to the parameters of the pseudo-jet i in the following way:

$$N_{\text{Clus}}^c \rightarrow k_{\text{t}}^{\text{i}} \text{ (transverse momentum)}$$
 (4.6)

$$x^{c} \rightarrow y^{i} \text{ (rapidity)}$$
 (4.7)

$$y^{c} \rightarrow \phi^{i} \text{ (azimuth)}$$
 (4.8)

 $N_{\text{Clus}}^c$ ,  $x^c$  and  $y^c$  denote the number of clusters and the lateral position of the cell c. The anti- $k_t$  algorithm is then applied to the pseudo-jets. Apart from certain exceptions, each jet reconstructed by the anti- $k_t$  algorithm corresponds to an electromagnetic shower inside the EPICAL-2. The exceptions are jets consisting of only one pseudo-jet, which are unlikely to correspond to an electromagnetic shower, and jets reconstructed in events with overlapping electromagnetic showers. Only events where a single jet is reconstructed from multiple pseudo-jets inside the fiducial region are selected in this analysis. Additionally, further conditions need to be met for an event to be selected to reduce the number of selected events with overlapping electromagnetic showers:

- 1. No cluster in layers 0 and 1 more than 1 mm away from the jet must be present.
- 2. All clusters in layers 0 and 1 must be less than 0.5 mm apart from each other.
- 3. At least one cluster in layer 0 must contribute to the jet.

Figure 4.1 shows the  $N_{\rm Hit}$  distribution (left) and the  $N_{\rm Clus}$  distribution (right) for all events and selected events. The distributions of all events show a peak at  $N_{\rm Hit} \approx 1500$  and  $N_{\rm Clus} \approx 370$  and further peaks at multiples of the first peak position. Single electron events generate the first peak, and the peaks to its right correspond to two and three electron events. The first peak has a shoulder towards low  $N_{\rm Hit}$  ( $N_{\rm Clus}$ ) values, which is generated by events with partially contained showers and events of electrons with energies

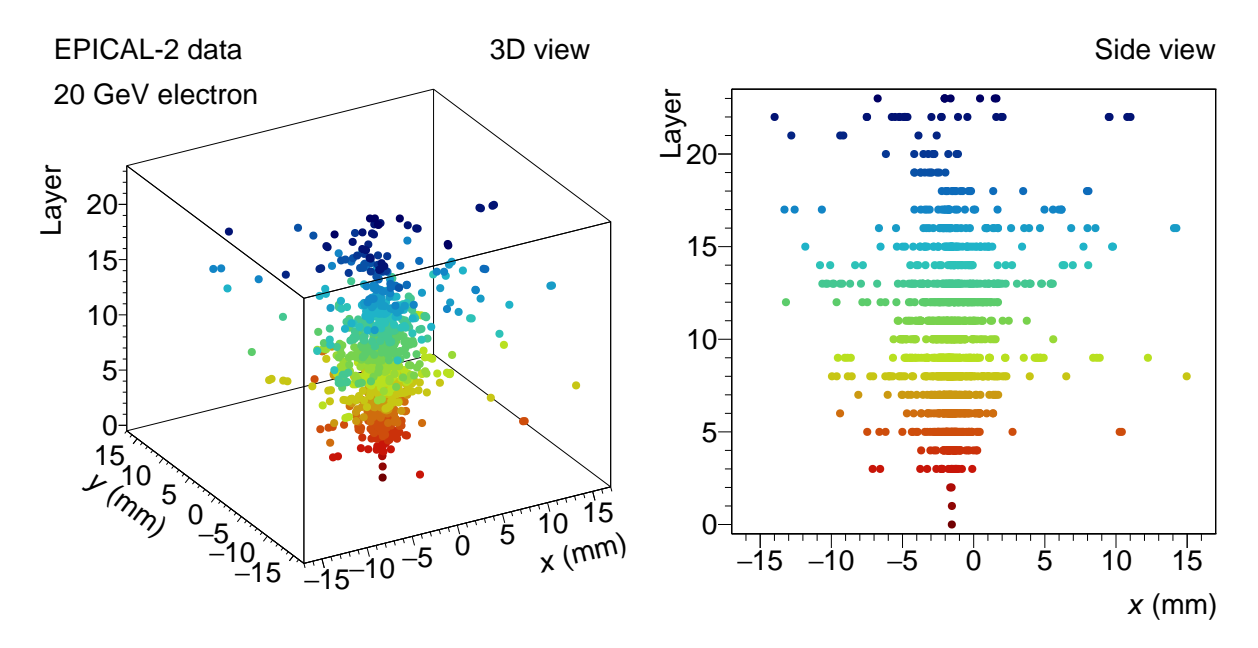


Figure 4.2: 3D view (left) and y-axis projection (right) of an event display, where a single electron with an energy of 20 GeV entered the EPICAL-2.

below the nominal beam energy. These are likely electrons from the test beam that lost energy by interacting with the beam collimators. The distributions of selected events show a single peak from single-electron events. The peak has a tail towards high  $N_{\rm Hit}$  ( $N_{\rm Clus}$ ) values, which is most likely generated by two-electron events with overlapping showers. However, in the selected data sample, the number of multi-electron events is around four orders of magnitude smaller than the number of single-electron events, which results in a single-electron event data sample which is sufficiently clean for this work. The shoulder towards low  $N_{\rm Hit}$  ( $N_{\rm Clus}$ ) values present in the distributions of all events are suppressed by a factor of 10 in the distributions of selected events. Most events with significant lateral leakage are rejected, but those with electrons below the nominal beam energy are not. However, the number of these events is at least three orders of magnitude lower than the number of events in the central peak of the distribution. Therefore, low-energy electrons are expected to have a negligible influence on the EPICAL-2's performance.

# 4.4.2 Event selection for CERN-SPS data

As discussed in section 2.2.3, the CERN-SPS test beam contains electrons, muons, and hadrons. Almost all muons traverse through the EPICAL-2 without showering. Hadrons either induce a hadronic shower or traverse the EPICAL-2 without showering like muons. Similar to the DESY data, in this work, only single-electron events inside the fiducial region are selected from the CERN-SPS data. Therefore, hadron- and muon-events are rejected since they would distort the detector response to electrons. To illustrate the difference between electron events and hadron events, both are presented in the following.

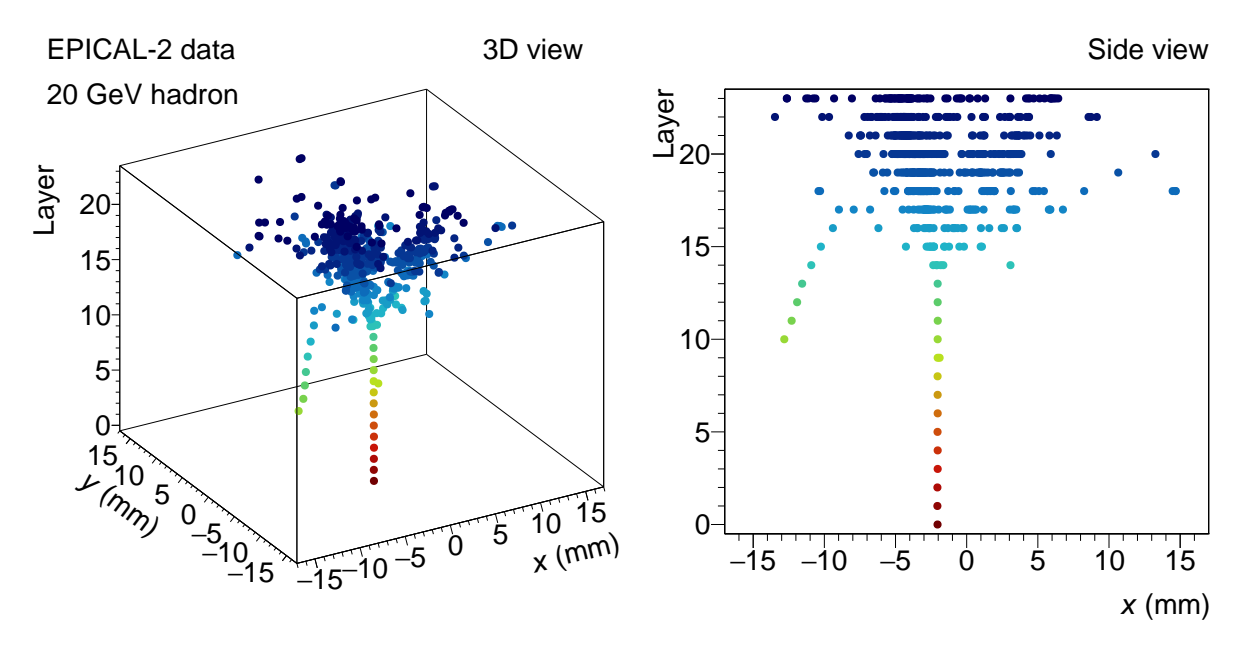


Figure 4.3: 3D view (left) and y-axis projection (right) of an event display, where a single hadron with an energy of 20 GeV entered the EPICAL-2.

## Difference between electron- and hadron-events:

Figure 4.2 shows an event display of a single-electron event. Each dot represents one cluster, and the color coding denotes the layer where the cluster is situated. The electron in Figure 4.2 enters the EPICAL-2 inside the fiducial region and starts an electromagnetic shower between layers 1 and 2. As visible in Figure 4.2, the shower is contained in the volume of the EPICAL-2, except for some minor leakage.

Figure 4.3 shows an event display of a single-hadron event, presented in the same fashion as figure 4.2. In the presented hadron event, the particle enters the EPICAL-2 inside the fiducial region and generates a track of clusters along its trajectory until layer 13. An interaction occurs between layers 13 and 14, causing a hadronic shower. As visible in Figure 4.3, the majority of the shower leaves the back of the EPICAL-2 and is thus not contained in the EPICAL-2's volume. Another noteworthy feature of this hadron event is the track-like structure covering layers 10 to 17 and  $-13\,\mathrm{mm} < x < -9\,\mathrm{mm}$ . This observation likely occurs in response to a particle interaction in the hadronic shower. A particle gets scattered in layer 17, then travels backward through the EPICAL-2 and gets absorbed in layer 10.

## Selection criteria:

To ensure that the EPICAL-2 contains a single electromagnetic shower, an event has to fulfill several selection criteria, which are adopted from [Rog23a]. Only events with a beam impact position situated inside the fiducial region are selected. Since the beam impact position is undefined for events with 0 or multiple clusters in layer 0, those events are rejected in this analysis. The  $N_{\rm Hit}$  distribution is parametrized by a Gaussian parameterization, and the following condition is imposed on an event to be selected for this

| E  (GeV) | $l_{ m ss}$ | $R_{ m Hit}^{ m r<2mm}$ |         | $\sigma_{ m Hit} \ ( m mm)$ |         | $f_{18}$ |         | $f_{14}$ |
|----------|-------------|-------------------------|---------|-----------------------------|---------|----------|---------|----------|
| 20       | $\leq 3$    | > 0.424                 | < 0.570 | > 3.609                     | < 5.418 | > 0.111  | < 0.697 | > 0.165  |
| 40       | $\leq 3$    | > 0.436                 | < 0.551 | > 3.792                     | < 5.257 | > 0.111  | < 0.615 | > 0.12   |
| 60       | $\leq 3$    | > 0.450                 | < 0.544 | > 3.972                     | < 5.097 | > 0.091  | < 0.602 | > 0.09   |
| 80       | $\leq 3$    | > 0.441                 | < 0.564 | > 3.729                     | < 5.243 | > 0.079  | < 0.638 | > 0.07   |

Table 4.3: Overview of the criteria an event has to fulfill in order to be selected.

analysis:

$$\mu - 5 \cdot \sigma < N_{\text{Hit}} < \mu + 5 \cdot \sigma \tag{4.9}$$

 $N_{\rm Hit}$  refers to the number of pixel hits in an event, and  $\mu$ ,  $\sigma$  are the mean and width of the Gaussian parameterization. This condition rejects most of the hadron and muon events because they have fewer pixel hits than electron events due to the different development of hadronic showers compared to electromagnetic showers. Additionally, further selections have been made based on several shower characterizing parameters defined in the following:

- 1. The layer  $l_{\rm ss}$  of shower start is defined as the layer before the number  $N_{\rm Clus}^{r=0.5{\rm mm}}$  of clusters inside a cylinder of radius 0.5 mm around the beam impact position satisfies  $N_{\text{Clus}}^{r=0.5\text{mm}} \geq 2$  for three consecutive layers.
- 2. The fraction  $R_{\rm Hit}^{\rm r<2mm}$  of hits in the shower core is defined as:

$$R_{\rm Hit}^{\rm r<2mm} = \frac{N_{\rm Hit}^{\rm r<2mm}}{N_{\rm Hit}} \tag{4.10}$$

 $N_{\rm Hit}^{\rm r<2mm}$  is the number of hits inside a cylinder of radius 2 mm around the beam impact position and  $N_{\rm Hit}$  is the total number of hits in an event.

3. The spread  $\sigma_{\text{Hit}}$  of pixel hits in the x-y-projection of the EPICAL-2 is defined as:

$$\sigma_{\rm Hit} = \sqrt{\sigma_{\rm x}^2 + \sigma_{\rm y}^2} \tag{4.11}$$

 $\sigma_{\rm x}$  and  $\sigma_{\rm y}$  are the standard deviations of the lateral pixel hit distribution in X- and Y-direction.

4. The forward to total ratios  $f_{14}$  and  $f_{18}$  of pixel hits are defined as:

$$f_{14} = \frac{N_{\text{Hit}}^{14}}{N_{\text{Hit}}} \tag{4.12}$$

$$f_{14} = \frac{N_{\text{Hit}}^{14}}{N_{\text{Hit}}}$$

$$f_{18} = \frac{N_{\text{Hit}}^{18}}{N_{\text{Hit}}}$$
(4.12)

 $N_{\rm Hit}^{14}$  and  $N_{\rm Hit}^{18}$  denote the number of hits up to layers 4 and 8, respectively.

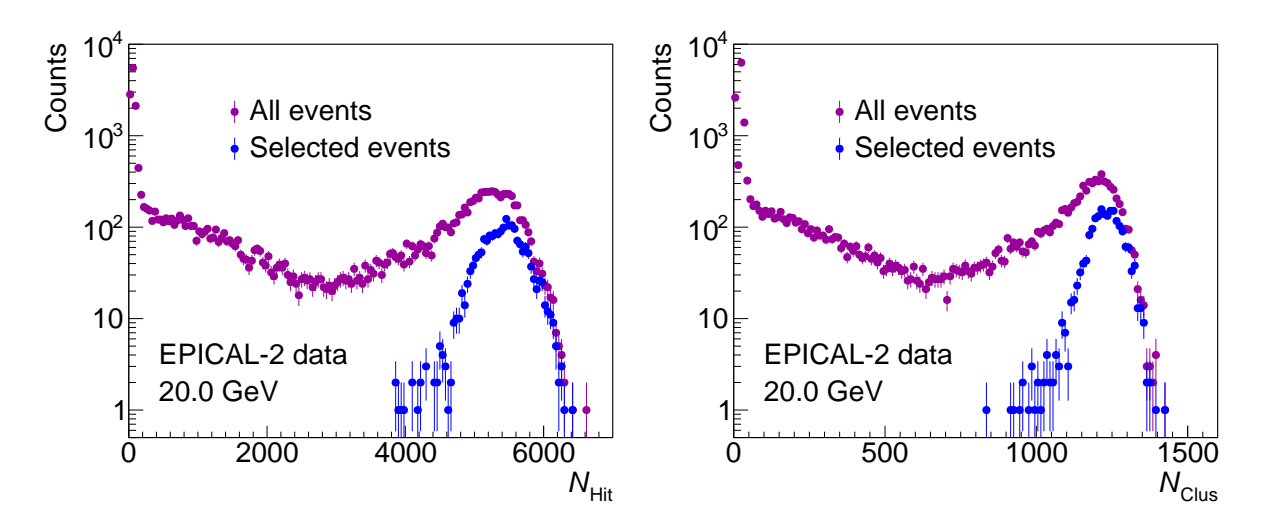


Figure 4.4: Distributions of  $N_{\text{Hit}}$  (left) and  $N_{\text{Clus}}$  (right) for all events and selected events of electrons with an average energy of 20 GeV.

Table 4.3 presents an overview of the conditions an event must fulfill to be selected in this analysis.

## Selection results:

Figure 4.4 shows the  $N_{\rm Hit}$ - and  $N_{\rm Clus}$ -distributions for all events and selected events of electrons with an average energy of 20 GeV. The distributions of all events show a peak at  $N_{\rm Hit} < 300$  and  $N_{\rm Clus} < 75$ . This peak consists of events of particles traversing the EPICAL-2 without showering. Right of that peak, the distributions show a broad continuum consisting of electron- and hadron-events with showers partially contained in the EPICAL-2's volume. The distributions show a Gaussian-shaped peak at  $N_{\rm Hit} \approx 5500$  and  $N_{\rm Clus} \approx 1250$ . This peak is composed of electron events with a single shower contained in the EPICAL-2's volume. The distributions of the selected events feature only the electron peak with a tail towards low  $N_{\rm Hit}$ - and  $N_{\rm Clus}$ -values. Except for this tail, the hadron and muon background is suppressed. With the event selection, the hadron contamination can be reduced to below 0.7 %, estimated by applying the event selection to simulations of electrons, hadrons, and muons. Therefore, the influence of hadron events on the performance of the EPICAL-2 is negligible in the selected data sample.

## Layer of shower start:

The algorithm to determine the layer  $l_{\rm ss}$  of shower start has been developed in the scope of this work and is presented in the following. With the definition of  $l_{\rm ss}$ , in most events,  $l_{\rm ss}$  corresponds to the layer in the EPICAL-2, after which the shower development starts. Due to the three-consecutive-layer requirement, the  $l_{\rm ss}$  can only be defined up to layer 20. Figure 4.5 shows the  $l_{\rm ss}$  distributions for the data and simulations of electrons, pions, kaons, protons, and muons with an energy of 20 GeV. For the electron simulation, the distribution shows a maximum in layer 0 and then decreases by three orders of magnitude

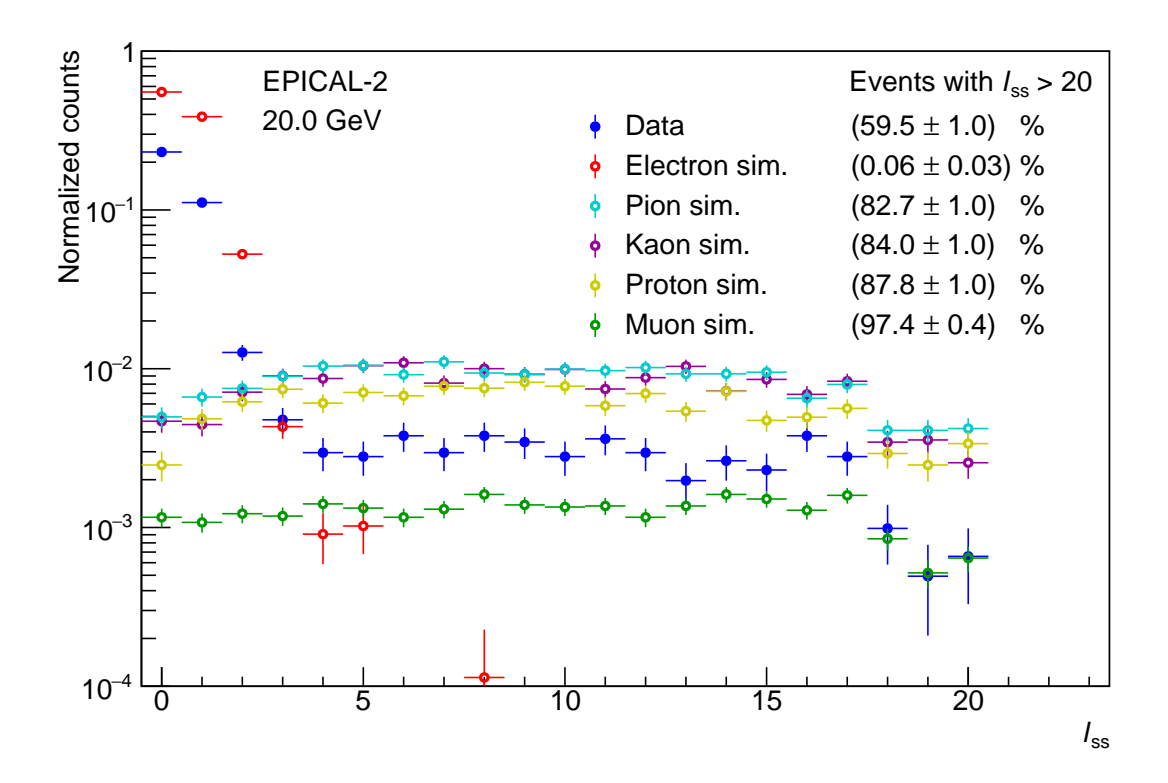


Figure 4.5:  $l_{ss}$  distributions for data and simulations of electrons, pions, kaons, protons, and muons at an energy of 20 GeV.

until layer 4 because most electrons develop a shower in the first layers of the EPICAL-2, due to the radiation length of tungsten corresponding approximately to the thickness of one tungsten absorber in the EPICAL-2.

The  $l_{\rm ss}$  distributions for all the hadron simulations are similar. The distributions for the hadron simulations increase by a factor of two from layers 0 to 3. From layers 3 to 17, the distributions for the hadron simulations are flat between values of  $10^{-2}$  and  $5 \cdot 10^{-3}$ . The flat behavior of the  $l_{\rm ss}$  distributions for hadrons is expected because the nuclear absorption length of tungsten is 99.46 mm [gro23] as discussed in section 1.1.2. This is greater than the 60 mm of tungsten in the first 20 layers of the EPICAL-2. In total, between 82 % and 88 % of all hadrons traverse the EPICAL-2 without inducing a shower.

The  $l_{ss}$  distribution for muons from layers 0 to 17 is flat at a value of approximately  $10^{-3}$ , which results in over 97 % of muon events without a reconstructed  $l_{ss}$ .

The  $l_{\rm ss}$  distribution of the data shows a peak at layer 0 and decreases by two orders of magnitude until layer 4. This behavior can be expected from electron events. From layers 4 to 17, the distribution from the data is flat at  $3 \cdot 10^{-3}$  with approximately 60% of all events without a reconstructed  $l_{\rm ss}$ , which is caused by hadron and muon events. A noteworthy feature in the  $l_{\rm ss}$  distributions for muons, hadrons, and data is the step-like structure between layers 17 and 18, where the distribution decreases by about 50% due to one sensor in layer 21 being disabled, causing the inability to reconstruct  $l_{\rm ss}$  beyond layer 17 in half the EPICAL-2.

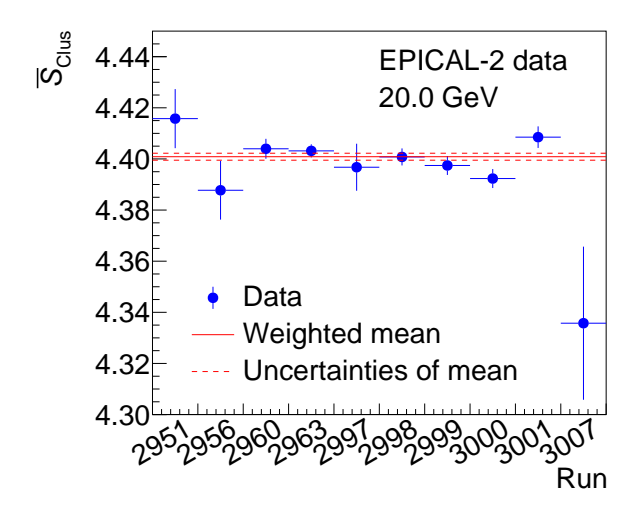


Figure 4.6: Average cluster size for each run, where electrons with an average energy of 20 GeV have been measured.

The difference in the behavior of the  $l_{ss}$  for electrons, muons, and hadrons in the early layers is exploited in the event selection to identify electron events.

# 4.5 Run quality analysis

The EPICAL-2's performance is not influenced by changes in the data-taking conditions. This is verified in a so-called run quality analysis performed in the scope of this thesis. The verification of a consistent behavior of the EPICAL-2 has been performed for the DESY data and is presented in [Keu21]. In the following, the verification of a consistent behavior of the EPICAL-2 across all runs of the same energy for the CERN-SPS data without backbias voltage is presented. Four observables that characterize the EPICAL-2's behavior have been compared between runs for a given primary-electron energy: the average cluster size  $\bar{S}_{\text{Clus}}$ , the mean  $\mu_{\text{Hit}}$  detector response for pixel hits, the mean  $\mu_{\text{Clus}}$  detector response for clusters and the maximum  $t_{\text{max}}$  of the longitudinal shower profile.

## 4.5.1 Cluster size

Figure 4.6 shows the average cluster size  $\bar{S}_{\text{Clus}}$  exemplary for each run at a beam energy of 20 GeV as well as the mean  $\langle \bar{S}_{\text{Clus}} \rangle$  over all runs, weighted by the number of selected events per run, and the statistical uncertainty of the weighted mean.  $\bar{S}_{\text{Clus}}$  fluctuates around the weighted mean within the corresponding statistical uncertainties for each run. Amongst all analyzed runs,  $\bar{S}_{\text{Clus}}$  for run 3007 deviated furthest from the weighted mean. It is possible that this deviation results from statistical fluctuations due to the low statistics in this run. The average cluster size  $\bar{S}_{\text{Clus}}$  for the other test-beam energies is presented in Appendix A.

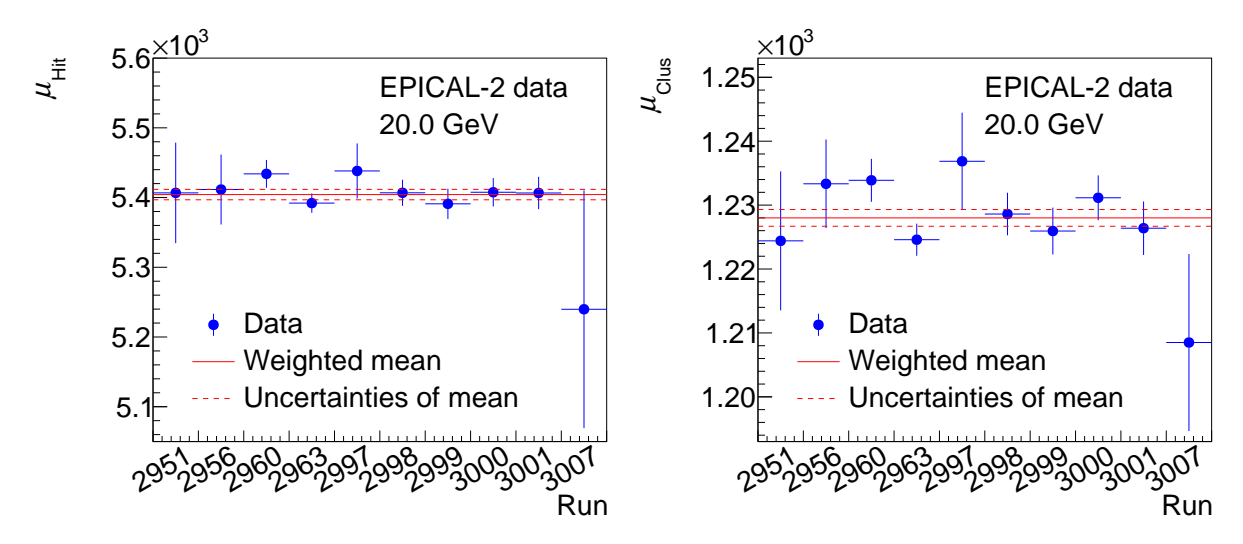


Figure 4.7: Mean pixel hit (left) and cluster (right) detector response for each run, where electrons with an average energy of 20 GeV have been measured.

# 4.5.2 Detector response

Figure 4.7 presents the mean pixel hit (cluster) detector response  $\mu_{\rm Hit}$  ( $\mu_{\rm Clus}$ ) exemplary for each run at a beam energy of 20 GeV and the weighted mean over all runs. Both observables fluctuate around their respective mean within their statistical uncertainties. It is noteworthy, that  $\mu_{\rm Hit}$  and  $\mu_{\rm Clus}$  are correlated. This is especially visible in run 3007, where both  $\mu_{\rm Hit}$  and  $\mu_{\rm Clus}$  are below the mean value. This correlation is plausible because the number of hits and clusters are proportional, with the average cluster size as a proportionality constant. The mean hit (cluster) detector response  $\mu_{\rm Hit}$  ( $\mu_{\rm Clus}$ ) for the other test-beam energies is presented in Appendix B and C.

# 4.5.3 Longitudinal shower maximum

The longitudinal shower profile is defined as the number of pixel hits as a function of the layer number in the EPICAL-2. To determine the maximum  $t_{\text{max}}$  of the longitudinal shower profile, a parameterization of the longitudinal shower profile with the gamma distribution  $f_{\text{gamma}}(x; \alpha, \theta)$  is performed.  $f_{\text{gamma}}(x; \alpha, \theta)$  is defined as [ROO23]:

$$f_{\text{gamma}}(x; \alpha, \theta) = \frac{1}{\Gamma(\alpha)\theta^{\alpha}} x^{\alpha - 1} e^{\frac{x}{\theta}}$$
(4.14)

 $\Gamma(\alpha)$  refers to the so-called gamma function,  $\alpha$ , and  $\theta$  are free parameters. From  $\alpha$ , and  $\theta$  the maximum of the parameterization, referred to as  $t_{\text{max}}$ , can be calculated as follows [Wik23b]:

$$t_{\text{max}} = (\alpha - 1)\theta \tag{4.15}$$

Figure 4.8 (left) depicts the longitudinal shower profile for the data at a beam energy of 20 GeV and the corresponding parameterization with  $f_{\text{gamma}}(x; \alpha, \theta)$ . In layer 21, the

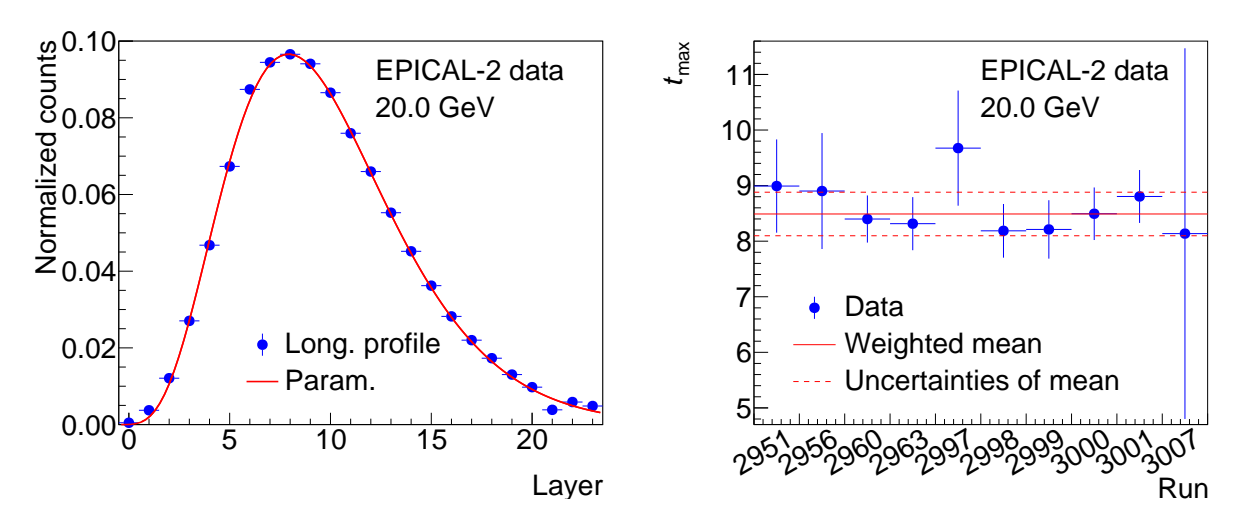


Figure 4.8: Longitudinal shower profile with gamma distribution parameterization (left) from electrons with an average energy of 20 GeV and the maximum of the longitudinal shower profile (right) for each run, where electrons with an average energy of 20 GeV have been measured.

profile is decreased by about  $50\,\%$  compared to the parameterization, which is caused by a disabled sensor in this layer.

Figure 4.8 (right) shows  $t_{\text{max}}$  exemplary for each run at a beam energy of 20 GeV and the weighted mean of all runs. The fluctuations of  $t_{\text{max}}$  for the different runs are compatible with the mean within their statistical uncertainties. The longitudinal shower maximum  $t_{\text{max}}$  for the other test-beam energies is presented in Appendix D.

The observables  $\bar{S}_{\text{Clus}}$ ,  $\mu_{\text{Hit}}$ ,  $\mu_{\text{Clus}}$ , and  $t_{\text{max}}$ , fluctuate around their respective weighted mean values within their statistical uncertainties. This verifies that changes in the conditions during the data taking had no statistically significant impact on the EPICAL-2's behavior.

# Chapter 5

# Results

In the scope of this thesis, the EPICAL-2's performance is analyzed in three separate studies: back-bias voltage variations, radial cuts, and leakage. Before discussing these studies, this chapter introduces two effects, saturation, and angular cluster enlargement, that are necessary to understand the presented results. Furthermore, a measure for the linearity of the EPICAL-2 is introduced.

# 5.1 Saturation and angular cluster-enlargement

#### **Saturation:**

Digital pixel calorimeters like the EPICAL-2 are subject to so-called saturation effects: At sufficiently high charged-particle density per sensor area, the increase in the number of pixel hits and clusters is not proportional to the number of charged particles traversing the sensor, as multiple charged particles contribute to the same pixel hit. In the EPICAL-2, saturation is strongest in a cylinder with a few mm radius around the beam impact position. The influence of saturation increases with the primary-electron energy since the number of charged particles in an electromagnetic shower and, thus, the density of charged particles per sensor area increases with the primary-electron energy. Cluster merging, as described in section 4.2, may be induced by saturation. Therefore, usually, saturation affects observables based on clusters more than those based on pixel hits.

# Angular cluster-enlargement:

A charged particle traversing a sensor in the EPICAL-2 under an angle with respect to the z-axis will liberate more charge carriers in the epitaxial layer than a charged particle traversing the sensor perpendicularly as its path through the epitaxial layer is longer. Therefore, particles traversing the sensor at an angle will induce larger clusters compared to particles traversing the sensor perpendicularly. This effect is referred to as angular cluster-enlargement. The angular cluster-enlargement increases with distance from the beam impact position in the lateral direction. The influence of angular cluster-

enlargement decreases with the primary-electron energy due to the average momentum in the longitudinal direction of shower particles increasing with the primary-electron energy. Response observables based on pixel hits are influenced more than ones based on clusters, as angular cluster-enlargement only influences the cluster size, not their number.

#### 5.2 Measure of linearity

The linearity of the EPICAL-2 is an important performance characteristic. In this work, the measure  $\lambda$  of linearity is used to quantify the linearity of the EPICAL-2.  $\lambda$  is a modified version of the coefficient  $r^2$  of determination [Wik24], which is a measure for the goodness of a parameterization.  $\lambda$  and  $r^2$  are related as follows:

$$\lambda = 1 - r^2 \tag{5.1}$$

To determine  $\lambda$ , first, the detector response  $\mu_{\text{Hit,Clus}}$  as a function of the primary-electron energy E is parametrized with the following linear function:

$$f(E) = a \cdot E \tag{5.2}$$

The parameter a denotes the slope of the linear function. The measure  $\lambda$  is calculated as follows [Wik24]:

$$\lambda = \frac{S_{\text{res}}}{S_{\text{tot}}} \tag{5.3}$$

$$\lambda = \frac{S_{\text{res}}}{S_{\text{tot}}}$$

$$S_{\text{res}} = \sum_{i} (\mu_{i} - f(E_{i}))^{2}$$

$$(5.3)$$

$$S_{\text{tot}} = \sum_{i} (\mu_{i} - \bar{\mu})^{2}$$
 (5.5)

For a certain datapoint i,  $\mu_i$  and  $E_i$  are the corresponding number of pixel hits or clusters and primary-electron energy.  $\bar{\mu}$  is the mean of  $\mu_i$  over all datapoints. A value of  $\lambda = 0$ would indicate perfect linearity of the EPICAL-2, and larger values of  $\lambda$  indicate deviations from an exactly linear behavior.

#### 5.3 Back-bias voltage variations

A back-bias voltage  $V_{\rm BB}$  changes the behavior of the sensors in the EPICAL-2 as described in section 2.1.3. The purpose of the analysis presented in this section is to study the influence of back-bias voltage of the sensors on the EPICAL-2's performance: The performance of the EPICAL-2 in data taken with  $V_{\rm BB}=0\,{\rm V}$  is compared to data taken with  $V_{\rm BB} = 3 \, \rm V$ . As described in section 4.1, during the test-beam campaign with the EPICAL-2 at CERN-SPS, data was recorded with both  $V_{\rm BB} = 0 \, \text{V}$  and  $V_{\rm BB} = 3 \, \text{V}$  applied to all sensors in even-numbered layers of the EPICAL-2 for primary-electron energies of 20, 40, and 60 GeV.

Due to the design of the EPICAL-2,  $V_{\rm BB} \neq 0$  is only possible in every even-numbered layer. Therefore, all odd-numbered layers of the EPICAL-2 are excluded from this analysis. The exclusion of all odd-numbered layers will result in a decrease in the detector response by a factor of approximately two.

As mentioned in section 4.1, the sensor on the left side of layer 2 of the EPICAL-2 was disabled during the measurements with  $V_{\rm BB}=3\,\rm V$ . To ensure comparability of the data sets with  $V_{\rm BB}=0$  and  $V_{\rm BB}=3\,\rm V$ , the sensor on the left side of layer 2 of the EPICAL-2 is excluded from this analysis.

The excluded sensor mentioned above has an influence on several observables used for the event selection described in section 4.4.2. Therefore, a modified event-selection process is employed for this analysis: Only events with a single cluster located inside the fiducial area of layer 0 of the EPICAL-2 are selected as described in section 4.4.2. Additionally, for each data set, the mean  $\mu_{\text{Hit}}$  and standard deviation  $\sigma_{\text{Hit}}$  of the distribution of the number  $N_{\text{Hit}}$  of pixel hits is calculated. Events that fulfill the following condition are selected:

$$\mu_{\text{Hit}} - 5 \cdot \sigma_{\text{Hit}} \le N_{\text{Hit}} \le \mu_{\text{Hit}} + 5 \cdot \sigma_{\text{Hit}}$$
 (5.6)

The clustering described in section 4.2 and the corrections described in section 4.3, except the calibration, are applied for this study. The calibration, which can improve the EPICAL-2's performance, is not applied for this study since the calibration factors cannot be determined for sensors that are operated with  $V_{\rm BB}=3\,\rm V$  due to no cosmic muons having been measured with that setting.

The influence of back-bias voltage on the following three performance-characterizing observables is studied: the mean cluster size  $\bar{S}_{\text{Clus}}$ , the detector response  $\mu_{\text{Hit,Clus}}$  for pixel hits and clusters, and the energy resolution for pixel hits and clusters.

# 5.3.1 Average cluster size

Figure 5.1 (left) shows the distribution of the cluster size  $S_{\text{Clus}}$  for measurements of electrons at the energies of 20, 40 and 60 GeV with a back-bias voltage of  $V_{\text{BB}} = 0 \text{ V}$  and  $V_{\text{BB}} = 3 \text{ V}$  applied to the sensors in the EPICAL-2. All distributions have a similar shape: Over 70% of all clusters have a cluster size  $S_{\text{Clus}} \leq 4$ . For  $S_{\text{Clus}} > 4$ , as the cluster size increases, the number of clusters decreases. Notable differences between the distributions of the data recorded with  $V_{\text{BB}} = 3 \text{ V}$  compared to  $V_{\text{BB}} = 0 \text{ V}$  is an increase in the number of clusters with  $2 \leq S_{\text{Clus}} \leq 5$ , with the largest increase (approximately 20%) being observed at  $S_{\text{Clus}} = 4$ . For  $S_{\text{Clus}} > 5$  the number of clusters is decreased by up to 35% in the data set with  $V_{\text{BB}} = 3 \text{ V}$  compared to the data set with  $V_{\text{BB}} = 0 \text{ V}$ . Figure 5.1 (right) shows the average cluster size  $\bar{S}_{\text{Clus}}$  as a function of the primary-electron energy E for measurements with a back-bias voltage of  $V_{\text{BB}} = 0 \text{ V}$  and  $V_{\text{BB}} = 3 \text{ V}$  applied

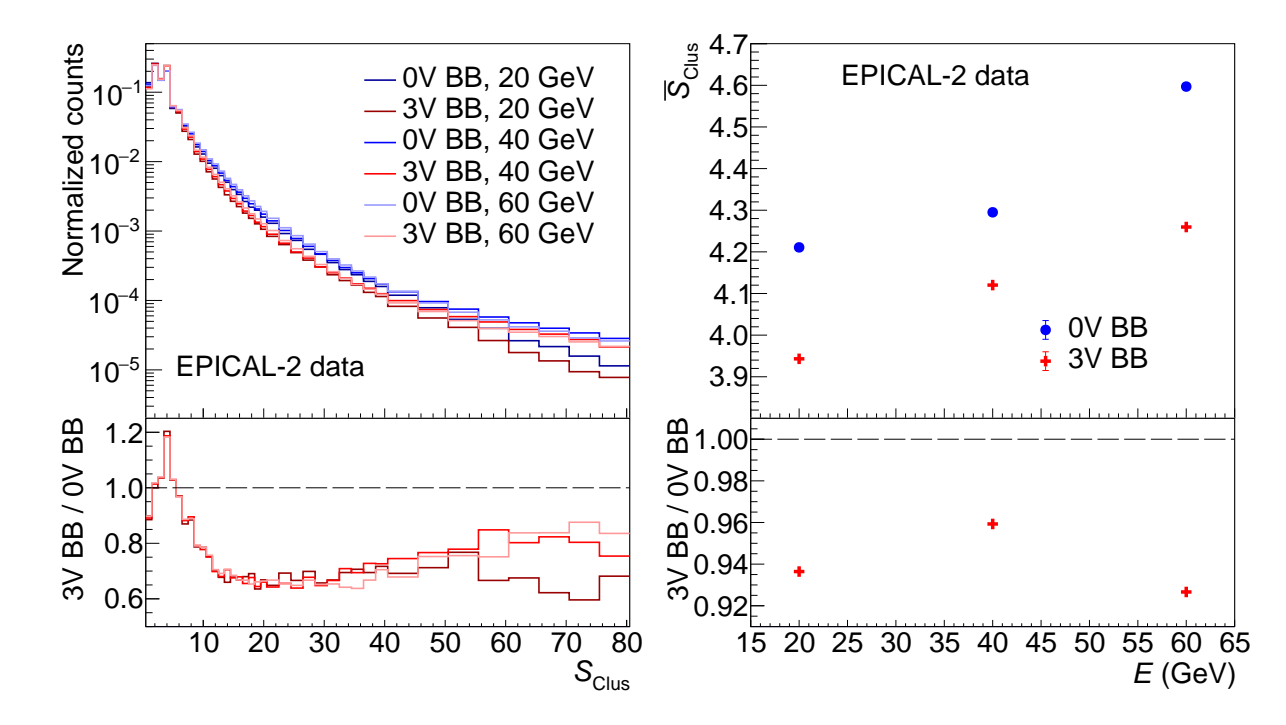


Figure 5.1: Distribution of the cluster size for the primary-electron energies of 20, 40 and  $60 \,\mathrm{GeV}$  (left) and mean cluster size as a function of the primary-electron energy (right) for a back-bias voltage setting of  $V_{BB} = 0 \,\mathrm{V}$  and  $V_{BB} = 3 \,\mathrm{V}$ .

to the sensors in the EPICAL-2. Over the measured energy range,  $\bar{S}_{\text{Clus}}$  increases with E by approximately 0.4 pixel hits for the data set with  $V_{\text{BB}} = 0 \, \text{V}$  and approximately 0.3 pixel hits for the data set with  $V_{\text{BB}} = 3 \, \text{V}$ . The data set with  $V_{\text{BB}} = 3 \, \text{V}$  features an up to 8% smaller average cluster size than the data set with  $V_{\text{BB}} = 0 \, \text{V}$ .

The increase in clusters with  $2 \le S_{\rm Clus} \le 5$  and decrease in clusters with  $S_{\rm Clus} > 5$  present in the data set with  $V_{\rm BB} = 3\,\rm V$  compared to the data set with  $V_{\rm BB} = 0\,\rm V$  observed in figure 5.1 (left), results in a decrease of the average cluster size observed in figure 5.1 (right), and can be explained as follows: With  $V_{\rm BB} = 3\,\rm V$  the depletion region of the collection implants in the sensors of the EPICAL-2 is enlarged compared to  $V_{\rm BB} = 0\,\rm V$ , as described in sections 1.3.1 and 2.1.3. Therefore, the mean distance a free charge carrier inside the epitaxial layer of the sensors in the EPICAL-2 can travel before it reaches a collection implant is reduced. Thus, the area over which the charge carriers spread inside the epitaxial layer gets smaller, resulting in reduced charge sharing between the pixels in the EPICAL-2 and, therefore, a smaller average cluster size in the data set with  $V_{\rm BB} = 3\,\rm V$  compared to  $V_{\rm BB} = 0\,\rm V$ . Additionally, saturation and cluster merging is likely supressed with  $V_{\rm BB} = 3\,\rm V$  compared to  $V_{\rm BB} = 0\,\rm V$ .

# 5.3.2 Detector response and linearity

Figure 5.2 (left) shows the mean detector response  $\mu_{\text{Hit}}$  for pixel hits and the mean detector response  $\mu_{\text{Clus}}$  for clusters as a function of the primary-electron energy E for the data

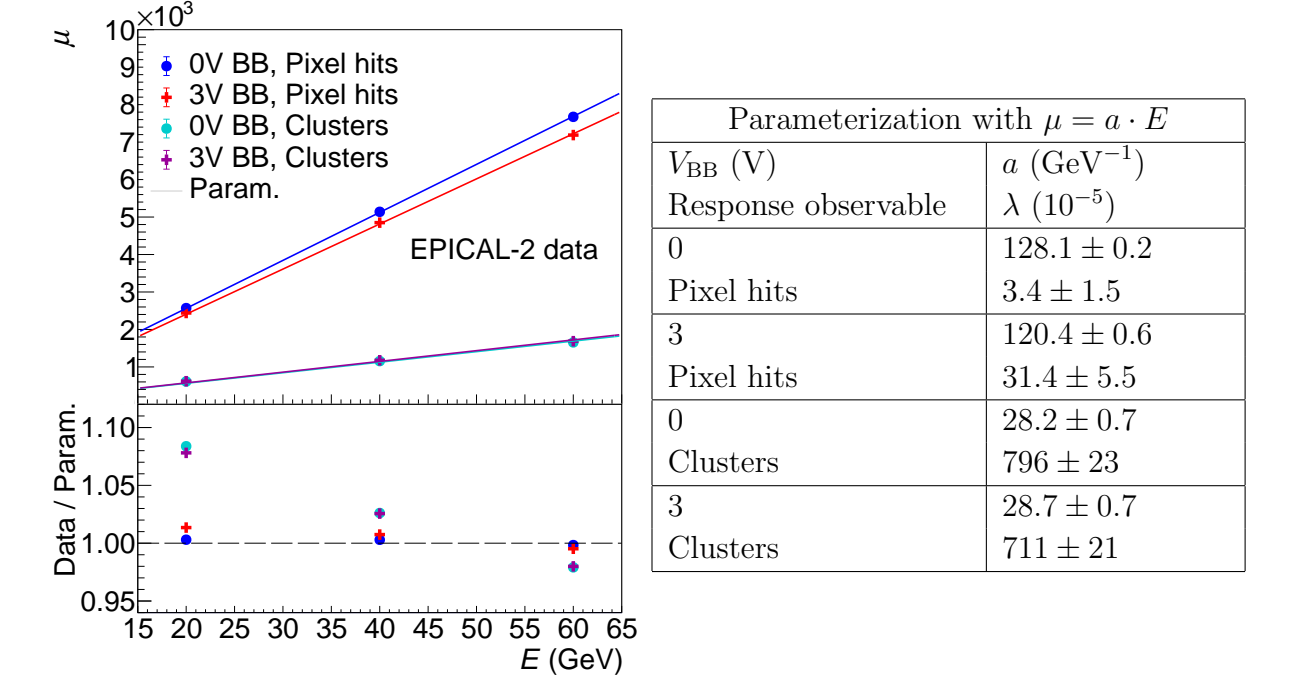


Figure 5.2: Mean detector response for hits and clusters as a function of the primaryelectron energy for a back-bias voltage setting of  $V_{BB} = 0 \text{ V}$  and  $V_{BB} = 3 \text{ V}$  with linear parameterizations (left) and table presenting an overview of the parameters a of the linear parameterizations and the corresponding measures  $\lambda$  of linearity (right).

set with  $V_{BB} = 0 V$  and the data set with  $V_{BB} = 3 V$  as well as parametrizations of  $\mu_{Hit}$  and  $\mu_{Clus}$  with a linear function. Figure 5.1 (right) shows a table presenting an overview of the slope a and the measure  $\lambda$  of linearity.

 $\mu_{\rm Hit}$  increases linearly with E with a slope of  $(128.1 \pm 0.2)\,{\rm GeV}^{-1}$  for  $V_{\rm BB} = 0\,{\rm V}$  and a slope of  $(120.4 \pm 0.6)\,{\rm GeV}^{-1}$  for  $V_{\rm BB} = 3\,{\rm V}$ . The difference in the slope of approximately 6.4% between the data sets with  $V_{\rm BB} = 0\,{\rm V}$  and  $V_{\rm BB} = 3\,{\rm V}$  can be explained by the reduction of the cluster size described in section 5.3.1: The clusters in the data set with  $V_{\rm BB} = 3\,{\rm V}$  show on average between 4% and 8% fewer pixel hits than in the data set with  $V_{\rm BB} = 0\,{\rm V}$ , therefore, the mean detector response for pixel hits is reduced.

Since the value of  $\lambda$  for  $V_{BB}=0\,V$  is approximately one order of magnitude smaller than for  $V_{BB}=3\,V$  it follows that the data set with  $V_{BB}=0\,V$  shows better linearity than the data set with  $V_{BB}=3\,V$ .

Similar to  $\mu_{\rm Hit}$ , the detector response  $\mu_{\rm Clus}$  for clusters increases linearly with E with a slope of  $(28.2\pm0.7)\,{\rm GeV^{-1}}$  for  $V_{\rm BB}=0\,{\rm V}$  and a slope of  $(28.7\pm0.7)\,{\rm GeV^{-1}}$  for  $V_{\rm BB}=3\,{\rm V}$ . It follows that the change in the back-bias voltage has no significant effect on  $\mu_{\rm Clus}$ . This is plausible because back-bias voltage is expected to only affect cluster size, not their number, except for a minor increase in the data set with  $V_{\rm BB}=3\,{\rm V}$  since clusters are less likely to merge. However, the effect of reduced cluster merging on  $\mu_{\rm Clus}$  is smaller than the statistical uncertainties in the measurements presented here.

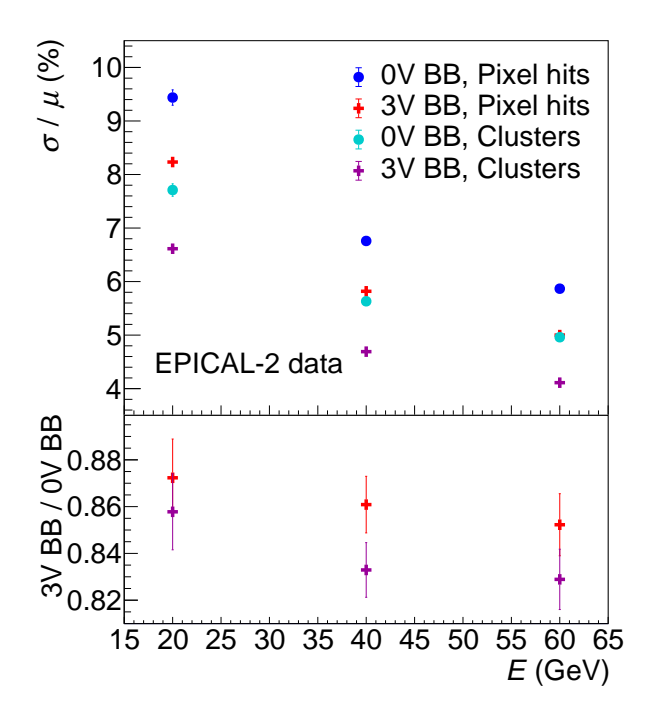


Figure 5.3: Energy resolution for pixel hits and clusters as a function of the primary-electron energy for a back-bias voltage setting of  $V_{BB} = 0 V$  and  $V_{BB} = 3 V$ .

The value of  $\lambda$  for  $V_{BB}=0\,V$  is approximately 12% larger than for  $V_{BB}=3\,V$ , indicating a slight improvement of the EPICAL-2's linearity for clusters with  $V_{BB}=3\,V$  compared to  $V_{BB}=0\,V$ .

# 5.3.3 Energy resolution

Figure 5.3 shows the energy resolution for pixel hits and clusters as a function of the primary-electron energy E for the data sets with  $V_{BB} = 0 \, V$  and with  $V_{BB} = 3 \, V$ . As explained in section 1.2, for an electromagnetic calorimeter like the EPICAL-2, a reduction of the energy resolution with approximately  $\sigma/\mu \propto 1/\sqrt{E}$  is expected. Such a reduction is observed for the energy resolution for both pixel hits and clusters and for both  $V_{BB} = 0 \, V$  and  $V_{BB} = 3 \, V$ . For both back-bias voltage settings, the energy resolution for clusters is between 16 % to 20 % better than for pixel hits as the number of pixel hits resulting from a single charged shower particle is subject to statistical fluctuations, which translate to fluctuations in the number of pixel hits and thus worsen the energy resolution for pixel hits. However, these fluctuations have no effect on the energy resolution for clusters.

For pixel hits, the energy resolution with  $V_{BB} = 3 \, V$  is improved by up to 15 % compared to the energy resolution with  $V_{BB} = 0 \, V$ . A similar effect is observed for clusters, where the energy resolution with  $V_{BB} = 3 \, V$  is improved by up to 17 % compared to the energy resolution with  $V_{BB} = 0 \, V$ . The improvement of the energy resolution with  $V_{BB} = 3 \, V$  compared to  $V_{BB} = 0 \, V$  can be explained as follows: Saturation effects are subject to statistical fluctuations that worsen the energy resolution for pixel hits and clusters. Due to

# Outer radial cut Excluded area Included area Cut radius rout Beam impact position

Right sensor

Left sensor

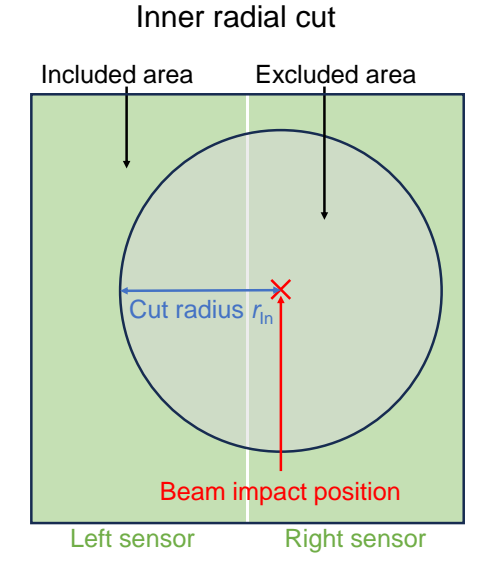


Figure 5.4: Illustration of the included and excluded area on the sensors in the EPICAL-2 for the inner and outer radial cut.

the reduced cluster size and, therefore, reduced number of pixel hits in the data set with  $V_{BB}=3\,\mathrm{V}$  compared to  $V_{BB}=0\,\mathrm{V}$ , at a comparable charged particle density, it is less likely that multiple charged particles contribute to the same pixel hits or clusters. This means saturation, and thus the statistical fluctuations resulting from saturation, are reduced in the data set with  $V_{BB}=3\,\mathrm{V}$  compared to  $V_{BB}=0\,\mathrm{V}$  and the resolution improves.

## Back-bias voltage variations - summary

The study of the influence of back-bias voltage on the performance of the EPICAL-2 showed the following: The back-bias voltage worsens the linearity for pixel hits while it slightly improves the linearity for clusters. The energy resolution can be improved by up to 15% for pixel hits and up to 17% for clusters.

# 5.4 Radial cuts

Excluding the pixel hits and clusters in the shower core or near the edge of the EPICAL-2, which can be accomplished by so-called radial cuts, could positively influence the performance. In the analysis presented in this section, the influence of radial cuts on the EPICAL-2's performance is studied.

Two different radial cuts are investigated: an outer radial cut and an inner radial cut. Figure 5.4 illustrates the difference between the cuts. When applying the outer radial cut, every pixel hit (cluster) whose center is located inside a cylinder with radius  $r_{\text{Out}}$  around the beam impact position contributes to the detector response. When applying

the inner radial cut, every pixel hit (cluster) whose center is located outside a cylinder with radius  $r_{\text{In}}$  around the beam impact position contributes to the detector response. Here again, the influence of the radial cuts on the following performance characterizing observables is studied: The mean cluster size  $\bar{S}_{\text{Clus}}$ , the detector response  $\mu_{\text{Hit,Clus}}$  for pixel hits and clusters, the linearity, and the energy resolution. In this section, rather than the detector response and energy resolution, the normalized detector response  $\mu_{\text{Hit,Clus}}^{\text{Norm}}$  and the normalized energy resolution  $\rho_{\text{Clus,Clus}}^{\text{Norm}}$  are discussed, which are calculated as follows:

$$\mu_{\mathrm{Hit,Clus}}^{\mathrm{Norm}} = \frac{\mu_{\mathrm{Hit,Clus}}}{E}$$
 (5.7)

$$\mu_{\text{Hit,Clus}}^{\text{Norm}} = \frac{\mu_{\text{Hit,Clus}}}{E}$$

$$\rho_{\text{Hit,Clus}}^{\text{Norm}} = \frac{\sigma_{\text{Hit,Clus}} \cdot \sqrt{E}}{\mu_{\text{Hit,Clus}}}$$
(5.7)

 $\mu_{\rm Hit,Clus}$  refers to the mean detector response for pixel hits or clusters,  $\sigma_{\rm Hit,Clus}$  refers to the standard deviation of the detector response for pixel hits or clusters, and E is the primary-electron energy. These normalizations are chosen because, due to the number of shower particles increasing with E, the observables  $\mu_{\text{Hit,Clus}}$  and the energy resolution show the following proportionality on E:

$$\mu_{\rm Hit, Clus} \propto E$$
 (5.9)

$$\mu_{\text{Hit,Clus}} \propto E$$

$$\frac{\sigma_{\text{Hit,Clus}}}{\mu_{\text{Hit,Clus}}} \propto \frac{1}{\sqrt{E}}$$
(5.9)

The normalization is performed to improve the presentability of the observables and to highlight differences between the primary-electron energies that do not result from the number of shower particles increasing with E.

In the analysis presented in this section, clustering, corrections, and selections are applied to the test-beam data as described in section 4.2, section 4.3, and section 4.4.

#### 5.4.1 Outer radial cut

The study of the influence of an outer radial cut on the observables  $\bar{S}_{\text{Clus}}$ ,  $\mu_{\text{Hit}}^{\text{Norm}}$ ,  $\mu_{\text{Clus}}^{\text{Norm}}$ ,  $\lambda_{\rm Hit},~\lambda_{\rm Clus},~\rho_{\rm Hit}^{\rm Norm},$  and  $\rho_{\rm Clus}^{\rm Norm}$  is presented in this section. For the purpose of this study, the cut radius  $r_{\text{Out}}$  is varied in a range from  $1 \text{ mm} \leq r_{\text{Out}} \leq 15 \text{ mm}$  in 1 mm increments.

## Mean cluster size:

Figure 5.5 shows the mean cluster size  $\bar{S}_{\text{Clus}}$  as a function of the cut radius  $r_{\text{Out}}$  for different primary-electron energies. For  $r_{\text{Out}} > 3 \,\text{mm}$ , the mean cluster size behaves similarly for all primary-electron energies E: An increase of  $\bar{S}_{Clus}$  between 2% to 4% is observed, likely due to angular cluster-enlargement. As discussed in section 5.1, angular cluster-enlargement increases the further away from the beam-impact position a cluster is located. Therefore, when  $r_{\text{Out}}$  gets smaller, more enlarged clusters are excluded, and the average cluster size decreases. For  $r_{\text{Out}} < 3 \,\text{mm}$  the behaviour of  $\bar{S}_{\text{Clus}}$  differs between

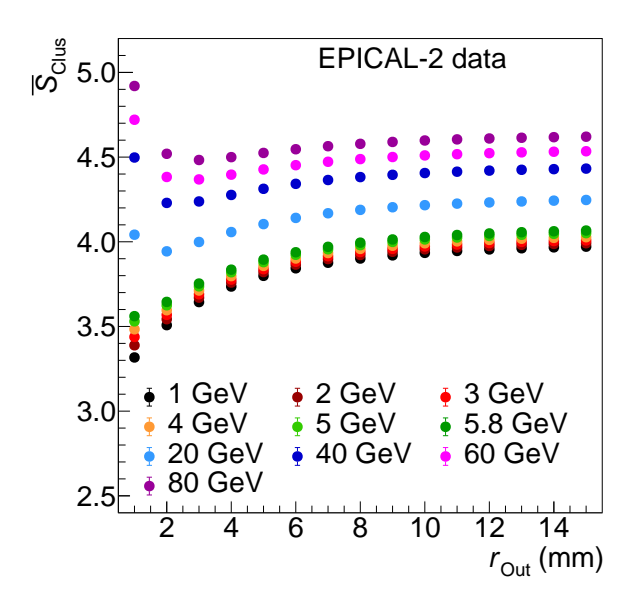


Figure 5.5: Average cluster size as a function of the outer cut radius for different primaryelectron energies.

 $E \leq 5.8\,\mathrm{GeV}$  and  $E \geq 20\,\mathrm{GeV}$ : For  $E \leq 5.8\,\mathrm{GeV}$  the mean cluster size increases with  $r_\mathrm{Out}$ . The explanation for this behaviour is the same as for  $r_\mathrm{Out} > 3\,\mathrm{mm}$ . For  $E \geq 20\,\mathrm{GeV}$   $\bar{S}_\mathrm{Clus}$  decreases with  $r_\mathrm{Out}$  until a primary-electron energy specific minimum is reached. The behavior of  $\bar{S}_\mathrm{Clus}$  for  $r_\mathrm{Out} < 3\,\mathrm{mm}$  can be explained via cluster merging, which gets more likely with increasing E and decreasing distance from the beam-impact position. Merged clusters are typically larger than unmerged clusters.

## Detector response and linearity:

Figure 5.6 (top left) and (top right) shows the normalized detector responses  $\mu_{\rm Hit,Clus}^{\rm Norm}$  for pixel hits and clusters as a function of the cut radius  $r_{\text{Out}}$  for different primary-electron energies. Both  $\mu_{\rm Hit}^{\rm Norm}$  and  $\mu_{\rm Clus}^{\rm Norm}$  increase with  $r_{\rm Out}$  until they saturate at a primaryelectron energy specific value. Even though both observables are normalized to E, an ordering depending on the primary-electron energy is observed:  $\mu_{\rm Hit,Clus}^{\rm Norm}$  decreases with E. The separation of the different primary-electron energies regarding the observable  $\mu_{\mathrm{Hit}}^{\mathrm{Norm}}$  is approximately 3 times smaller than for  $\mu_{\mathrm{Clus}}^{\mathrm{Norm}}$ . This is explainable by two effects: saturation and longitudinal leakage. Saturation reduces the mean detector response because multiple charged shower particles contribute to the same pixel hits or clusters, as explained in section 5.1. Since saturation increases with the primary-electron energy, the normalized detector response decreases with E. Saturation also induces cluster merging, which further reduces the mean detector response for clusters. Therefore, the difference between the primary-electron energies is larger for  $\mu_{\text{Clus}}^{\text{Norm}}$  than for  $\mu_{\text{Hit}}^{\text{Norm}}$ . An effect that also reduces the mean detector response is longitudinal leakage, which is further discussed in section 5.5. Longitudinal leakage also increases with the primary-electron energy and, therefore, contributes to the separation of the normalized detector response between the

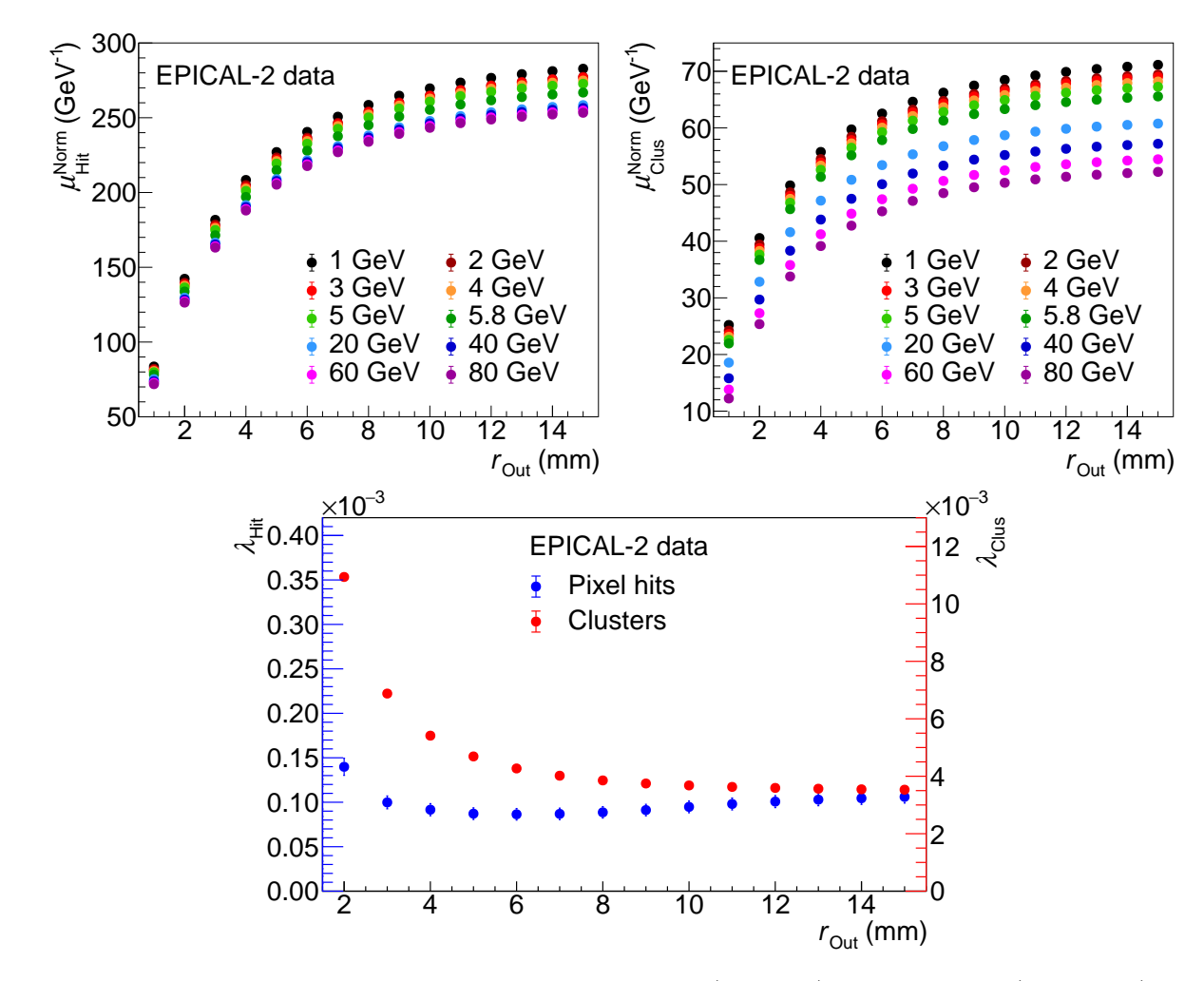


Figure 5.6: Mean detector response for pixel hits (top left) and clusters (top right) as a function of the outer cut radius for different primary-electron energies. Measure of linearity (bottom) for pixel hits and clusters as a function of the outer cut radius.

different primary-electron energies.

Figure 5.6 (bottom) shows the measure  $\lambda_{\rm Hit,Clus}$  of linearity for pixel hits and clusters as a function of the cut radius  $r_{\rm Out}$ . For pixel hits,  $\lambda_{\rm Hit}$  decreases with  $r_{\rm Out}$  until reaching a minimum at  $r_{\rm Out}=6$  mm. After the minimum,  $\lambda_{\rm Hit}$  increases with  $r_{\rm Out}$ . Therefore, an outer radial cut can benefit the linearity of the EPICAL-2 when studying pixel hits. The improvement of the linearity is likely caused by the linearity-harming effect of angular cluster-enlargement being suppressed by an outer radial cut. For clusters,  $\lambda_{\rm Clus}$  decreases with  $r_{\rm Out}$  until it converges to  $\lambda_{\rm Clus}\approx 3.5\cdot 10^{-3}$  for  $r_{\rm Out}>12$  mm. It follows that the application of an outer radial cut does not improve the linearity of clusters since the above-mentioned angular cluster-enlargement, which gets suppressed by an outer radial cut, has no influence on the detector response for clusters.

## Energy resolution:

Figure 5.7 (left) shows the normalized energy resolution  $\rho_{\text{Hit}}^{\text{Norm}}$  for pixel hits as a function of the cut radius  $r_{\text{Out}}$  for different primary-electron energies. For all E, the behaviour of

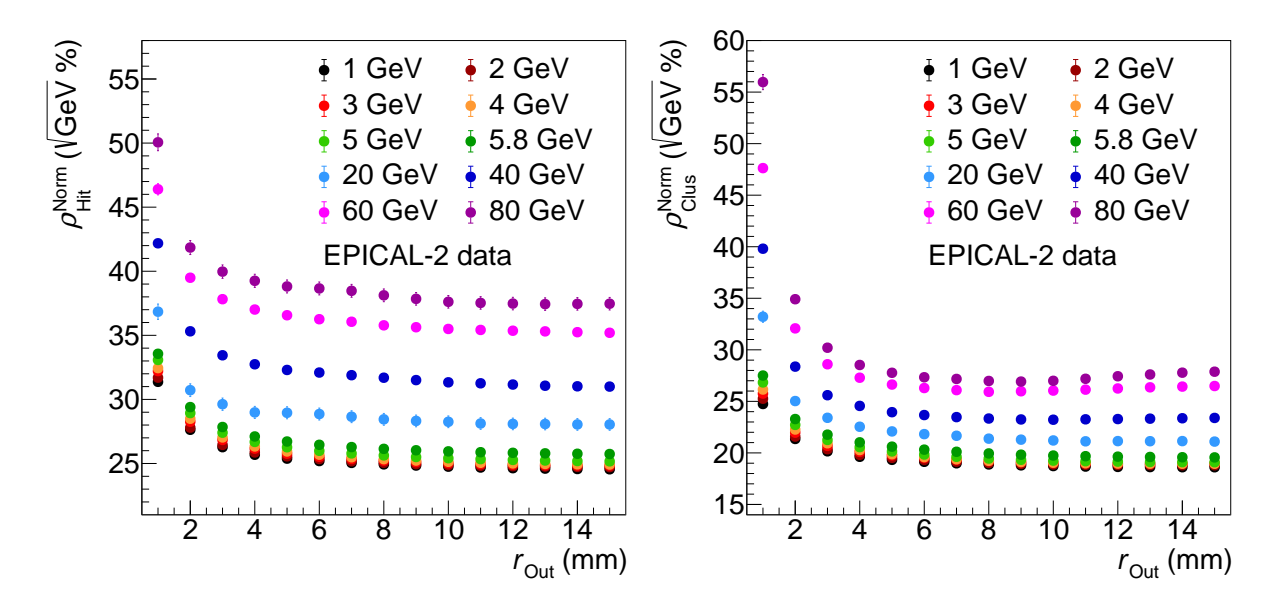


Figure 5.7: Energy resolution for pixel hits (left) and clusters (right) as a function of the outer cut radius for different primary-electron energies.

 $\rho_{\rm Hit}^{\rm Norm}$  is similar:  $\rho_{\rm Hit}^{\rm Norm}$  improves with  $r_{\rm Out}$ . It follows that an outer radial cut does not benefit the energy resolution for pixel hits. A noteworthy feature is the primary-electron energy ordering of  $\rho_{\rm Hit}^{\rm Norm}$ :  $\rho_{\rm Hit}^{\rm Norm}$  worsens with increasing E, which is likely caused by saturation: As mentioned in section 5.1, saturation increases with energy, and, as described in section 5.3.3, saturation worsens the energy resolution.

Figure 5.7 (right) shows the normalized energy resolution  $\rho_{\text{Clus}}^{\text{Norm}}$  for clusters as a function of the cut radius  $r_{\text{Out}}$  for different primary-electron energies. Similar to  $\rho_{\text{Hit}}^{\text{Norm}}$ , a primary-electron energy ordering of  $\rho_{\text{Clus}}^{\text{Norm}}$  is observed. For  $E \leq 40\,\text{GeV}$   $\rho_{\text{Clus}}^{\text{Norm}}$  decreases with  $r_{\text{Out}}$ . For  $E \geq 60\,\text{GeV}$  a minimum of  $\rho_{\text{Clus}}^{\text{Norm}}$  at  $r_{\text{Out}} = 8\,\text{mm}$  is present:  $\rho_{\text{Clus}}^{\text{Norm}}$  is approximately 4% better at the minimum than at  $r_{\text{Out}} = 15\,\text{mm}$ . The improvement in the resolution via an outer radial cut can be explained as follows: The distance of the beam-impact position to the edges of the EPICAL-2 in the lateral plane is subject to statistical fluctuations. Since leakage depends on the distance of the beam-impact position to the edges of the EPICAL-2, these statistical fluctuations translate to variations in the detector response and, therefore, worsen the energy resolution of the EPICAL-2. The effects of the edges of the EPICAL-2 are suppressed by an outer radial cut. Therefore, it is possible to improve the energy resolution for clusters by up to 4% through the use of an outer radial cut.

### Outer radial cut - summary:

An outer radial cut has the potential to improve the linearity for pixel hits but not for clusters. The energy resolution for clusters for  $E \geq 60 \,\text{GeV}$  can also be improved by an outer radial cut.

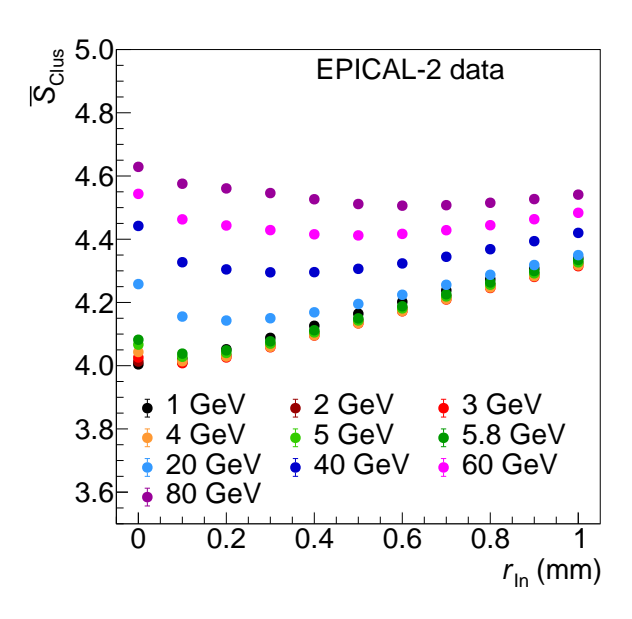


Figure 5.8: Average cluster size as a function of the inner cut radius for different primaryelectron energies.

## 5.4.2 Inner radial cut

A study of the influence of an inner radial cut on the observables  $\bar{S}_{\text{Clus}}$ ,  $\mu_{\text{Hit}}^{\text{Norm}}$ ,  $\mu_{\text{Clus}}^{\text{Norm}}$ ,  $\lambda_{\text{Hit}}$ ,  $\lambda_{\text{Clus}}$ ,  $\rho_{\text{Hit}}^{\text{Norm}}$ , and  $\rho_{\text{Clus}}^{\text{Norm}}$  is presented in this section. For the purpose of this study, the cut radius  $r_{\text{In}}$  is varied in a range from  $0 \text{ mm} \leq r_{\text{In}} \leq 4 \text{ mm}$  in 0.1 mm increments for  $0 \text{ mm} \leq r_{\text{In}} \leq 1 \text{ mm}$  and 1 mm increments for  $1 \text{ mm} < r_{\text{In}} \leq 4 \text{ mm}$ .

# Mean cluster size:

Figure 5.8 shows the mean cluster size  $\bar{S}_{\text{Clus}}$  as a function of the cut radius  $r_{\text{In}}$  for different primary-electron energies.  $\bar{S}_{\text{Clus}}$  decreases with  $r_{\text{In}}$  until a primary-electron energy specific minimum is reached, after which  $\bar{S}_{\text{Clus}}$  increases with  $r_{\text{In}}$ . With increasing E, the minimum of  $\bar{S}_{\text{Clus}}$  shifts towards higher  $r_{\text{In}}$ : At  $E=1\,\text{GeV}$  the minimum is observed at  $r_{\text{In}}=0.1\,\text{mm}$  while at  $E=80\,\text{GeV}$  the minimum is observed at  $r_{\text{In}}=0.6\,\text{mm}$ .

The behavior of  $\bar{S}_{\text{Clus}}$  under variation of  $r_{\text{In}}$  can be explained by cluster merging and angular cluster-enlargement as follows: The likelihood of clusters merging increases the closer clusters are located to the beam impact position. Therefore, when  $r_{\text{In}}$  increases, the average cluster size decreases since merged clusters, which are typically larger than unmerged clusters, are excluded. The increase of  $\bar{S}_{\text{Clus}}$  after the minimum occurs because clusters close to the beam impact position, which are likely not subject to angular cluster-enlargement, are excluded by an inner radial cut. This leads to a higher contribution of angularly enlarged clusters located far from the beam impact position, which leads to an increase of  $\bar{S}_{\text{Clus}}$ .

The minimum is likely located at a value of  $r_{\text{In}}$  at which most merged clusters are excluded while preserving most clusters that are not subject to angular cluster-enlargement.

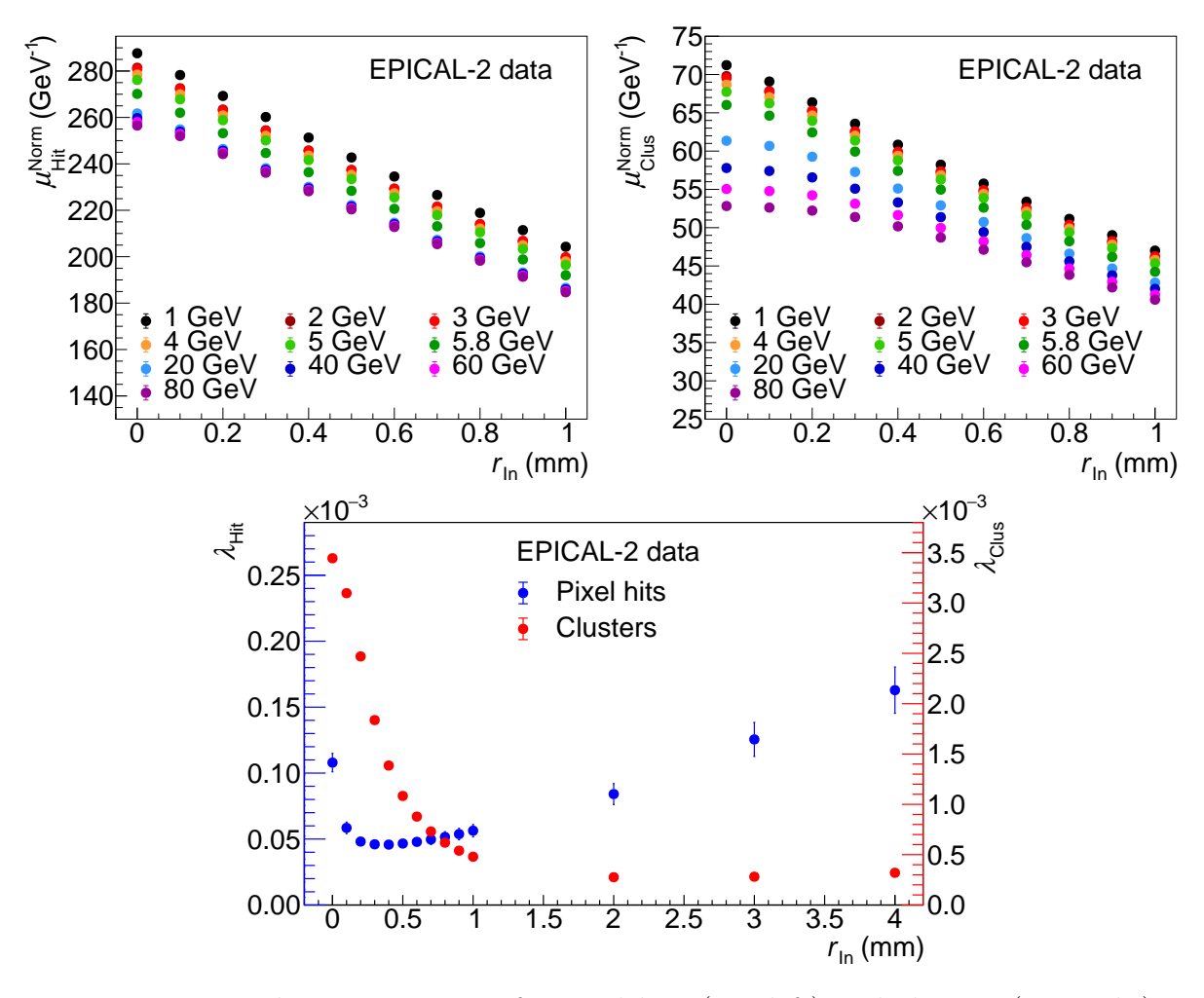


Figure 5.9: Mean detector response for pixel hits (top left) and clusters (top right) as a function of the inner cut radius for different primary-electron energies. Measure of linearity (bottom) for pixel hits and clusters as a function of the inner cut radius.

The minimum shifts towards higher values  $r_{\text{In}}$  because the probability of clusters merging increases with E, while angular cluster-enlargement decreases with E.

## Detector response and linearity:

Figure 5.9 (top left) and (top right) show the normalized detector responses  $\mu_{\rm Hit,Clus}^{\rm Norm}$  for pixel hits and clusters as a function of the cut radius  $r_{\rm In}$  for different primary-electron energies.  $\mu_{\rm Hit}^{\rm Norm}$  decreases approximately linearly with  $r_{\rm In}$  with a slope of approximately  $-80\,{\rm GeV^{-1}mm^{-1}}$  for all E. A similar approximately linear decrease with a slope of  $-25\,{\rm GeV^{-1}mm^{-1}}$  is observed for  $\mu_{\rm Clus}^{\rm Norm}$  for  $E \le 5.8\,{\rm GeV}$ . For  $E \ge 20\,{\rm GeV}$  the behaviour of  $\mu_{\rm Clus}^{\rm Norm}$  differs from  $E \le 5.8\,{\rm GeV}$ : At  $r_{\rm In} \le 0.1\,{\rm mm}$  almost no decrease of  $\mu_{\rm Clus}^{\rm Norm}$  is present. At  $r_{\rm In} > 0.6\,{\rm mm}$  the decrease of  $\mu_{\rm Clus}^{\rm Norm}$  converges towards a linear decrease with a slope of approximately  $-14\,{\rm GeV^{-1}mm^{-1}}$ . The difference in the behavior of  $\mu_{\rm Clus}^{\rm Norm}$  between  $E \le 5.8\,{\rm GeV}$  and  $E \ge 20\,{\rm GeV}$  can be explained by cluster merging: Due to the high density of clusters near the beam impact position at  $E \ge 20\,{\rm GeV}$ , likely multiple clusters are merged. Therefore, the number of clusters in a certain area near the beam

impact position is likely smaller than the number of charged shower particles traversing the same area. This is different for  $E \leq 5.8\,\mathrm{GeV}$ , where cluster merging is less likely to occur, and the number of clusters in a certain area is likely similar to the number of charged shower particles traversing the same area. Therefore, the normalized number of clusters near the beam impact position for  $E \geq 20\,\mathrm{GeV}$  is lower than for  $E \leq 5.8\,\mathrm{GeV}$ .

Figure 5.9 (bottom) shows the measure  $\lambda_{\rm Hit,Clus}$  of linearity for pixel hits and clusters as a function of the cut radius  $r_{\rm In}$ . For pixel hits,  $\lambda_{\rm Hit}$  decreases by more than a factor of 2 until reaching a minimum at  $r_{\rm In}=0.3\,{\rm mm}$ . After the minimum  $\lambda_{\rm Hit}$  increases with  $r_{\rm In}$ . The improvement of the linearity at  $r_{\rm In}=0.3\,{\rm mm}$  can be explained as follows: Since the effect of saturation on the mean detector response increases with the primary-electron energy, saturation leads to deviations from a linear increase of the detector response as a function of E. Therefore, saturation worsens the linearity. As described in section 5.1, saturation occurs most likely close to the beam impact position. An inner radial cut with  $r_{\rm In}=0.3\,{\rm mm}$  excludes pixel hits near the beam impact position and, therefore, suppresses the effect of saturation. It follows that by applying an inner radial cut of  $r_{\rm In}=0.3\,{\rm mm}$ , the linearity of the mean detector response for pixel hits can be improved.

For clusters,  $\lambda_{\text{Clus}}$  decreases by approximately one order of magnitude until reaching a minimum at  $r_{\text{In}} = 2 \, \text{mm}$ . After the minimum  $\lambda_{\text{Clus}}$  increases with  $r_{\text{In}}$ . Similar to pixel hits, this behavior can be explained by the suppression of saturation by an inner radial cut. The improvement of the linearity and the value of  $r_{\text{In}}$  at which the best linearity is achieved is approximately 5 times larger for clusters than for pixel hits because saturation has a stronger effect on clusters than on pixel hits due to saturation-induced cluster merging. It follows that the application of an inner radial cut can benefit the linearity of the detector response for clusters.

## Energy resolution:

Figure 5.10 (left) and (right) show the normalized energy resolution  $\rho_{\rm Hit,Clus}^{\rm Norm}$  for pixel hits and clusters as a function of the cut radius  $r_{\rm In}$  for different primary-electron energies. For all primary-electron energies,  $\rho_{\rm Hit,Clus}^{\rm Norm}$  increases with  $r_{\rm In}$ . Due to pixel hits and clusters being excluded by an inner radial cut, for each event the detector response is reduced. This increases the relative fluctuations of the detector response between the events, which leads to worse energy resolution. Therefore, neither for pixel hits nor for clusters can the energy resolution of the EPICAL-2 be improved by the application of an inner radial cut.

## Inner radial cut - summary:

An inner radial cut has the potential to improve the linearity of the EPICAL-2 for both pixel hits and clusters. The energy resolution worsens with an inner radial cut.

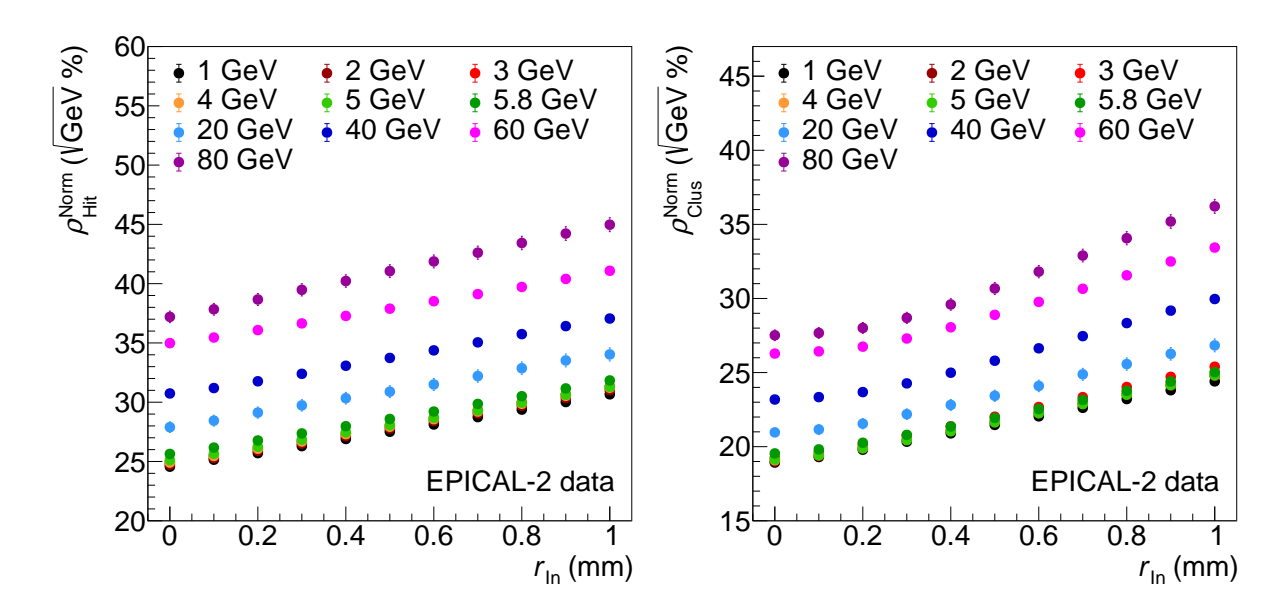


Figure 5.10: Energy resolution for pixel hits (left) and clusters (right) as a function of the inner cut radius for different primary-electron energies.

### 5.5 Leakage

Leakage of shower particles out of the volume of the EPICAL-2 influences the performance. An enlarged version of the EPICAL-2, called EPICAL-2L, is simulated to study the influence of leakage in this thesis. Since longitudinal leakage is expected to depend on the primary-electron energy E, simulations beyond the test-beam energies from  $E=0.2\,\mathrm{GeV}$  to  $E=1000\,\mathrm{GeV}$  are analyzed. To study leakage, the following performance-characterizing observables are compared between the EPICAL-2 simulation and the EPICAL-2L simulation: the mean cluster size  $\bar{S}_{\mathrm{Clus}}$ , the detector response  $\mu_{\mathrm{Hit,Clus}}$  for pixel hits and clusters, the measure  $\lambda_{\mathrm{Hit,Clus}}$  of linearity, and the energy resolution  $\sigma_{\mathrm{Hit,Clus}}/\mu_{\mathrm{Hit,Clus}}$  for pixel hits and clusters.

In the following, in addition to the total leakage, the longitudinal leakage and lateral leakage are studied. To accomplish this, two different cuts are applied to simulation data of the EPICAL-2L: a longitudinal cut and a lateral cut. With the longitudinal cut applied, every pixel hit and cluster beyond layer 23 is excluded, effectively giving the EPICAL-2L the same length as the EPICAL-2. Therefore, the effects of leakage in only the lateral direction can be studied. With the lateral cut applied, every pixel hit and cluster outside the following region is excluded, effectively giving the EPICAL-2L the same lateral dimensions as the EPICAL-2:  $1536 \le \text{column} \le 2560 \text{ and } -512 \le \text{row} \le 512$ . Therefore, the effects of leakage in only the longitudinal direction can be studied. Via the application of both cuts, the consistent behavior of the EPICAL-2 and EPICAL-2L simulations can be verified for each observable studied.

In the analysis presented in this section, no corrections or selections are necessary since, in the simulation, the dimensions of the EPICAL-2 and EPICAL-2L are exact, the behavior

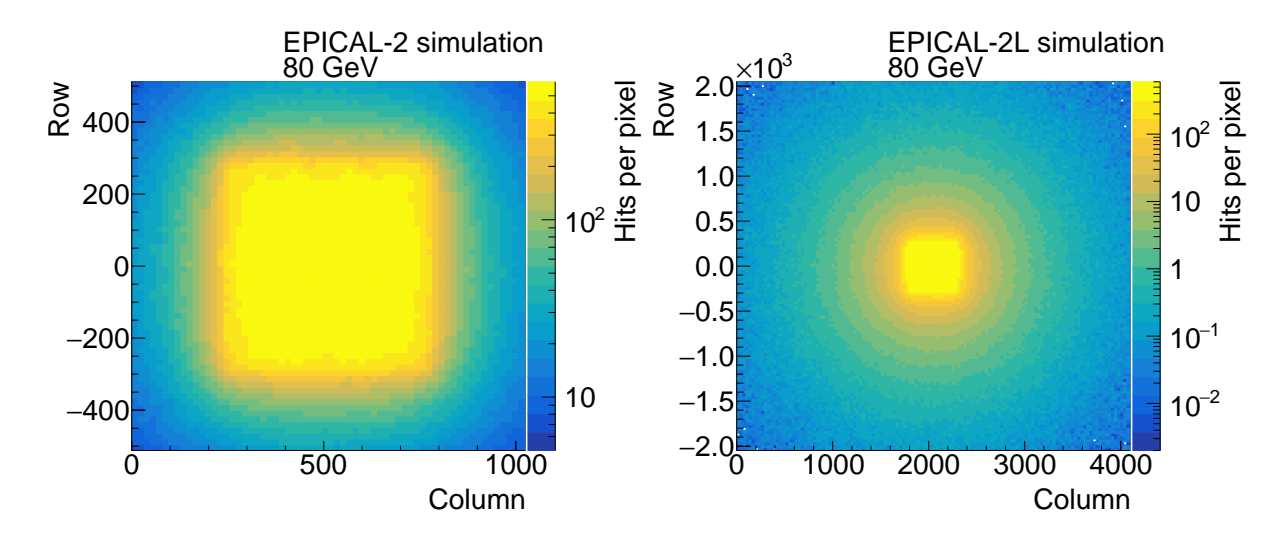


Figure 5.11: Number of pixel hits integrated over all events and layers of the EPICAL-2 (left) and the EPICAL-2L (right) as a function of column and row for simulations with a primary-electron energy of 80 GeV.

is consistent across all pixels in the EPICAL-2 and EPICAL-2L and clean data samples of single-electron events are present. For this analysis, pixel hits are clustered as described in section 4.2.

#### 5.5.1 Pixel-hit profiles of the EPICAL-2 and EPICAL-2L

In preparation for the studies of the influence of leakage on the detector performance, the distribution of pixel hits in the lateral and longitudinal direction of the EPICAL-2 and EPICAL-2L are studied.

Figure 5.11 (left) shows the number of pixel hits as a function of column and row, referred to as a hitmap, integrated over all events and layers of the EPICAL-2 simulation with a primary-electron energy of 80 GeV. In the center of the EPICAL-2, a square-shaped area with approximately 600 hits per pixel is measured. This area corresponds to the  $16 \times 16 \text{ mm}^2$  area over which the primary electrons are distributed in the simulation as described in section 3.1. Towards the edges of the hitmap, the number of hits per pixel decreases by approximately one order of magnitude compared to the center of the hitmap. Towards the corners of the hitmap, the number of hits per pixel decreases by up to two orders of magnitude compared to the center of the hitmap.

Figure 5.11 (right) shows the hitmap integrated over all events and all layers of the EPICAL-2L simulation with a primary-electron energy of 80 GeV. Like in the Hitmap for the EPICAL-2, in the center of the EPICAL-2L, the square-shaped area with up to 600 hits per pixel, resulting from the beam profile, is present. Compared to the center of the hitmap, the number of hits per pixel decreases by approximately three orders of magnitude towards the edges of the hitmap and by up to five orders of magnitude towards the corners of the hitmap.

Figure 5.12 shows the number of pixel hits per pixel column of the EPICAL-2 and

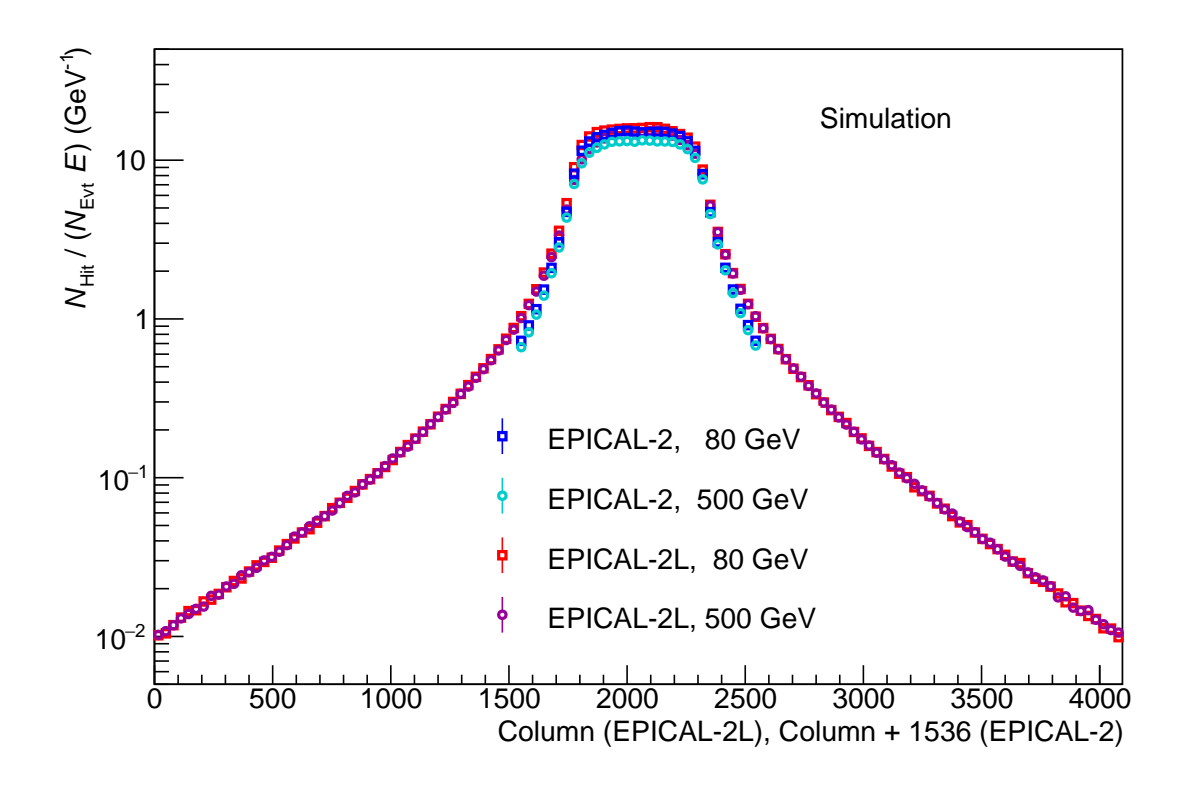


Figure 5.12: Normalized number of pixel hits as a function of the column in the EPICAL-2 and EPICAL-2L for simulations with a primary-electron energy of 80 GeV and 500 GeV.

EPICAL-2L, which corresponds to the projection of the hitmap on the row axis, for simulations with a primary-electron energy E of 80 and 500 GeV, normalized on the number  $N_{\rm Evt}$  of events and the primary-electron energy E. In figure 5.12, a constant of 1536 is added to the column of the EPICAL-2 for presentational purposes so that the center of the EPICAL-2 and EPICAL-2L align in the plot.

The distributions for the EPICAL-2 at  $80\,\mathrm{GeV}$  and  $500\,\mathrm{GeV}$  behave similarly: They show an approximately 512-column wide plateau centered at column 2048, which results from the beam profile. Towards the edges of the EPICAL-2, both distributions decrease approximately by one order of magnitude. A noteworthy difference between the distributions for the EPICAL-2 at  $80\,\mathrm{GeV}$  and  $500\,\mathrm{GeV}$  is that, despite the normalization on E, they do not align perfectly: The distribution for  $500\,\mathrm{GeV}$  shows approximately  $12\,\%$  fewer pixel hits per event and E. This is due to deviations from linearity, likely caused by two effects: First, as mentioned in section 5.4.2, saturation decreases the normalized detector response, which corresponds to the integral over the distribution shown in figure 5.12. Since saturation is more likely at higher energies, the distribution for  $500\,\mathrm{GeV}$  shows fewer pixel hits per event and E than the distribution for  $80\,\mathrm{GeV}$ . Second, longitudinal leakage also decreases the detector response. Since longitudinal leakage increases with the primary-electron energy because the shower maximum shifts towards later layers, this also contributes to the difference between the distributions for  $80\,\mathrm{GeV}$  and  $500\,\mathrm{GeV}$ .

Both the distribution at 80 GeV and 500 GeV for the EPICAL-2L show a plateau simi-

lar to the distributions for the EPICAL-2 and drop by about three orders of magnitude towards the edges of the EPICAL-2L. A difference in the number of pixel hits per event and E between the distribution for 80 GeV and 500 GeV, similar to what is observed for the EPICAL-2, is also present in the EPICAL-2L, but only for 1600 < column < 2500. Outside that range, the distributions for the EPICAL-2L are the same within statistical uncertainties. This can be explained as follows: Near the center of the EPICAL-2L, saturation causes a difference between the distributions for 80 GeV and 500 GeV as it is the case for the EPICAL-2. Since saturation is mostly relevant near the beam impact position, as mentioned in 5.1, outside the range 1600 < column < 2500, saturation becomes insignificant. Therefore, the distributions are the same in that range. In the case of the EPICAL-2L, longitudinal leakage is likely not contributing to the difference between the distributions for  $80 \, \text{GeV}$  and  $500 \, \text{GeV}$ , since longitudinal leakage is expected to be negligible in the EPICAL-2L.

For the EPICAL-2, the decrease in the number of pixel hits is steeper than for the EPICAL-2L. Thus, even in an area corresponding to the active area of the EPICAL-2, the EPICAL-2L behaves differently. Shower particles leaving the EPICAL-2 are unlikely to reenter its volume since there is no material despite air outside the EPICAL-2's volume. For the EPICAL-2L, this is different. The tungsten absorbers of the EPICAL-2L laterally extend outside an area corresponding to that of the EPICAL-2. The additional tungsten enables the scattering of shower particles back into a volume that corresponds to the size of the EPICAL-2. These backscattered particles induce additional pixel hits inside that volume, causing the observed difference between the distributions of the EPICAL-2 and EPICAL-2L.

Figure 5.13 shows the number of pixel hits per layer of the EPICAL-2 and EPICAL-2L for simulations with a primary-electron energy of 80 GeV and 500 GeV, normalized on the number  $N_{\rm Evt}$  of events and the primary-electron energy E. All distributions increase until a maximum is reached, and then they decrease approximately exponentially. For both the EPICAL-2 and EPICAL-2L simulations, the maximum shifts from layer 10 to layer 12 when comparing  $E=80\,{\rm GeV}$  to  $E=500\,{\rm GeV}$ . The distributions for the EPICAL-2 decrease in the range from the maximum until layer 23 by approximately one order of magnitude for 80 GeV and by a factor of 4 for 500 GeV. Both the distributions for 80 GeV and 500 GeV for the EPICAL-2L decrease in the range from the maximum until layer 95 by approximately six orders of magnitude.

Past the maximum, for both distributions of the EPICAL-2 the observed decrease is steeper than for the EPICAL-2L. The explanation for this behavior is similar to the explanation for the difference of the distributions in the lateral direction: The absorbers in the additional layers of the EPICAL-2L enable the backscattering of shower particles into the volume before layer 23, where they can induce additional pixel hits.

It follows from the observation in figure 5.12 and figure 5.13 that the EPICAL-2L behaves differently inside the volume corresponding to that of the EPICAL-2 due to backscattering

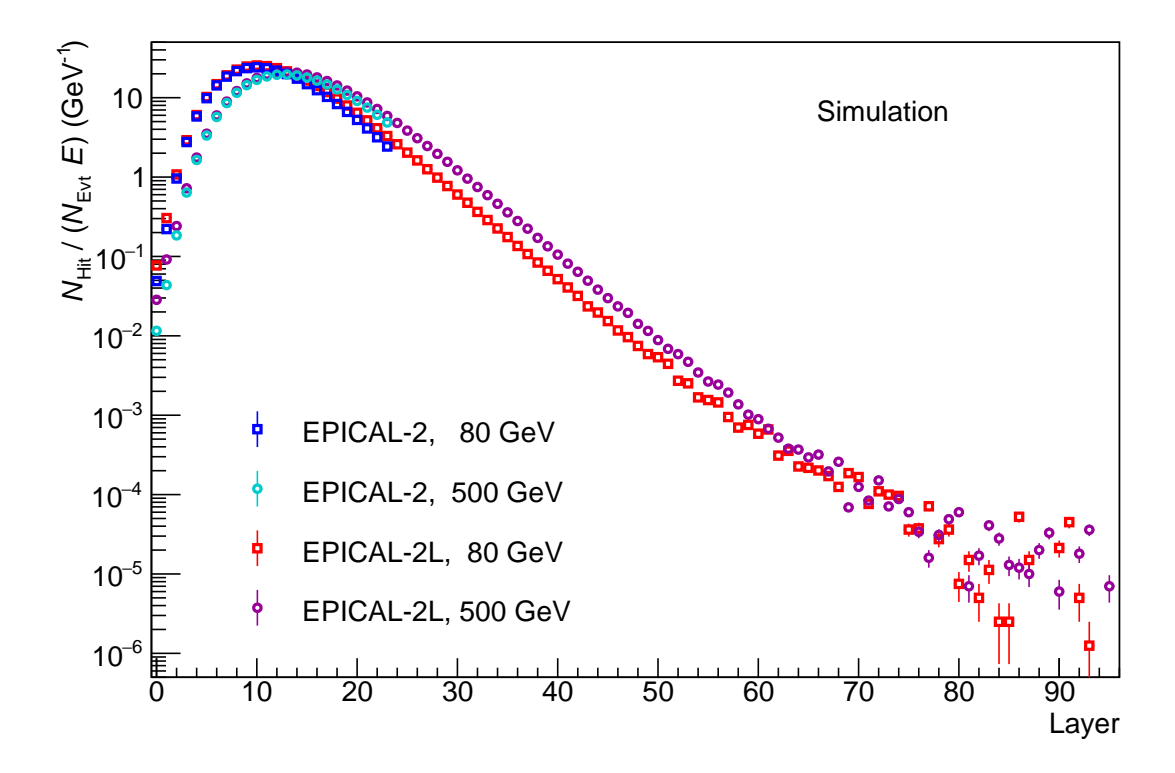


Figure 5.13: Normalized number of pixel hits as a function of the layer in the EPICAL-2 and EPICAL-2L for simulations with a primary-electron energy of 80 GeV and 500 GeV.

of shower particles. Since this difference could influence the results presented in the following, it is important to verify the compatibility of the two detectors for each performance observable studied by applying both longitudinal and lateral cuts to the EPICAL-2L simultaneously: By applying both cuts the EPICAL-2L has effectively the same size as EPICAL-2 and any difference in the performance observables could be caused by the above explained backscattering.

#### 5.5.2 Average cluster size

Figure 5.14 shows the mean cluster size  $\bar{S}_{\text{Clus}}$  as a function of the primary-electron energy E in simulations of the EPICAL-2 and EPICAL-2L with different cut settings applied to the EPICAL-2L. For the EPICAL-2 and all cut settings for the EPICAL-2L,  $\bar{S}_{\text{Clus}}$  increases with E.  $\bar{S}_{\text{Clus}}$  for the EPICAL-2 and the EPICAL-2L with both cuts applied behave the same within statistical uncertainties. Therefore, backscattering of shower particles has no effect on the observable  $\bar{S}_{\text{Clus}}$  in the EPICAL-2L. For  $E \leq 80\,\text{GeV}$ ,  $\bar{S}_{\text{Clus}}$  in the EPICAL-2L simulation with the lateral cut and the EPICAL-2 simulation are the same within statistical uncertainties. The EPICAL-2 simulation shows up to 2.5% smaller  $\bar{S}_{\text{Clus}}$  than the EPICAL-2L simulations with the longitudinal cut and without cuts, likely because angular cluster-enlargement is increased for a laterally extended EPICAL-2. For

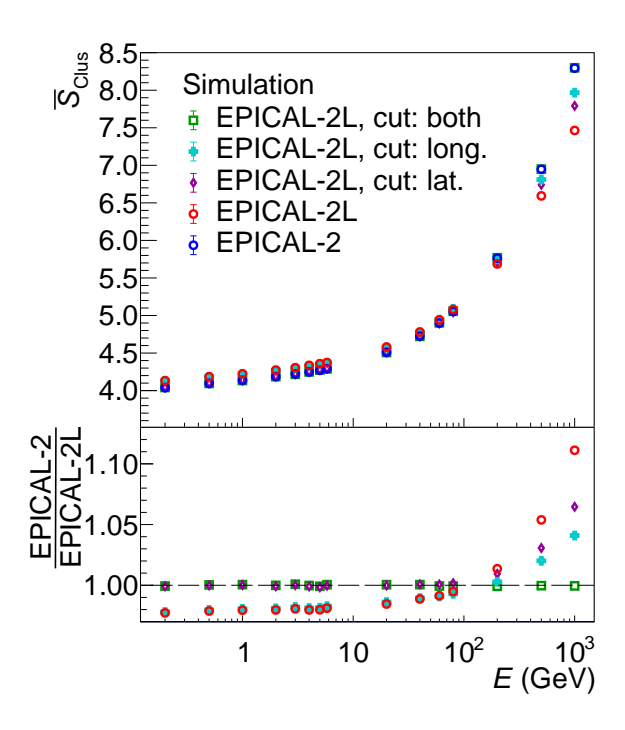


Figure 5.14: Mean cluster size as a function of the primary-electron energy in simulations of the EPICAL-2 and EPICAL-2L with different cut settings applied to the EPICAL-2L.

 $E \geq 200\,\mathrm{GeV}$ , in the EPICAL-2 simulation,  $\bar{S}_{\mathrm{Clus}}$  is decreased by up to 10 % compared to the EPICAL-2L simulation with the longitudinal cut, the lateral cut, and without cuts, likely because the influence of cluster merging on  $\bar{S}_{\mathrm{Clus}}$  is reduced when enlarging the EPICAL-2 in either longitudinal or lateral direction since almost all merged clusters are located inside the volume of the EPICAL-2. Therefore, the observables discussed in the following likely also show signs of cluster merging being less influential in an enlarged EPICAL-2.

#### 5.5.3 Detector response and linearity

Figure 5.15 shows the detector response  $\mu_{\rm Hit}$  for pixel hits (left) and detector response  $\mu_{\rm Clus}$  for clusters (right) as a function of the primary-electron energy E in simulations of the EPICAL-2 and EPICAL-2L with different cut settings applied to the EPICAL-2L, and corresponding linear parameterizations. The parameterizations have been performed in a range from  $0.2\,{\rm GeV} \le E \le 5.8\,{\rm GeV}$ , since in this range, longitudinal leakage is expected to be negligibly small (< 1 %). For both pixel hits and clusters, the detector responses of the EPICAL-2 and the EPICAL-2L with both cuts applied are the same within statistical uncertainties. Therefore, backscattering has no significant effect on the observables  $\mu_{\rm Hit}$  and  $\mu_{\rm Clus}$  in the EPICAL-2L. The comparison of  $\mu_{\rm Hit,Clus}$  between the EPICAL-2 and the EPICAL-2L with the longitudinal cut applied is a measure for the leakage in the lateral direction: For pixel hits, the leakage in the lateral direction is constant at approximately 8 % across all E, which is plausible since the shower spread in the lateral direction is

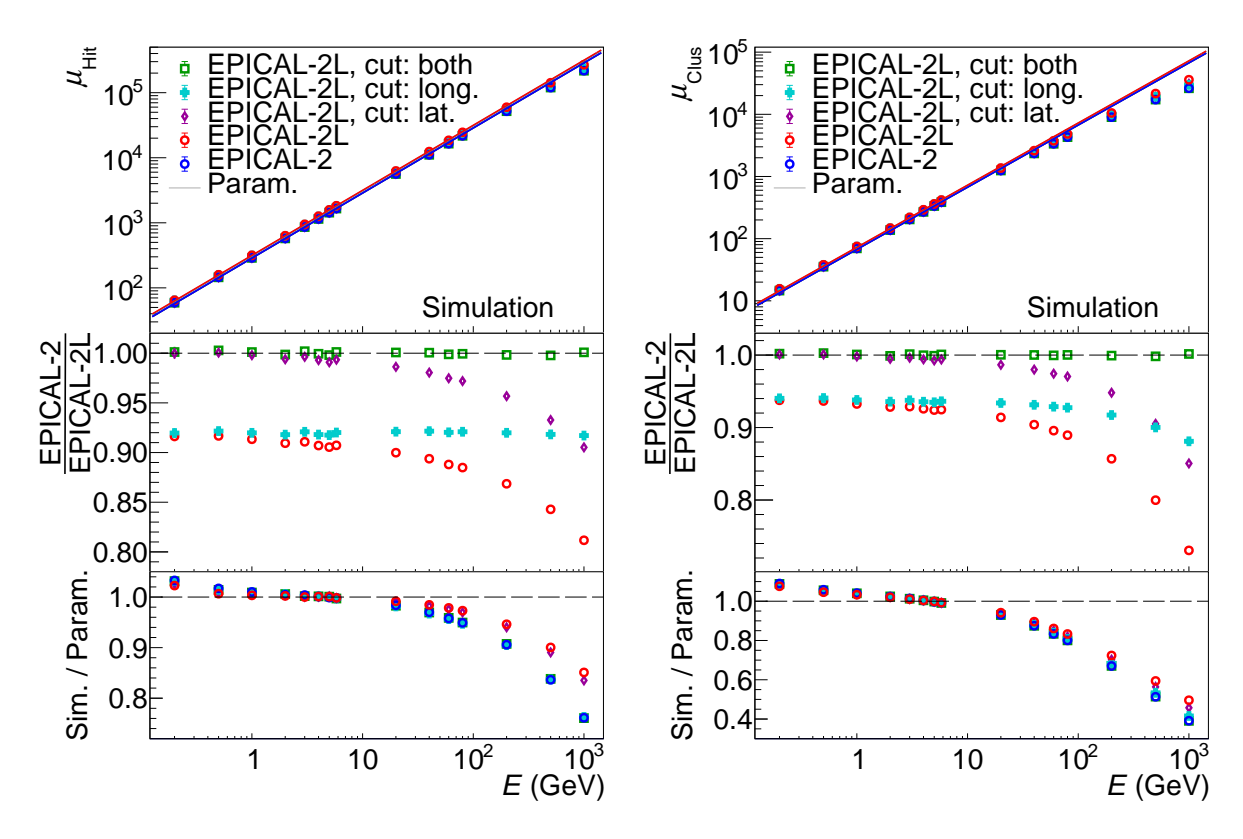


Figure 5.15: Detector response for pixel hits (left) and clusters (right) as a function of the primary-electron energy in simulations of the EPICAL-2 and EPICAL-2L with different cut settings applied to the EPICAL-2L.

expected to be independent of the primary-electron energy as described in section 1.1. For clusters, the leakage in the lateral direction is constant at approximately 6% for  $E \leq 80\,\mathrm{GeV}$  and increases to approximately 12% at  $E = 1000\,\mathrm{GeV}$ . The comparison of  $\mu_{\mathrm{Hit,Clus}}$  between the EPICAL-2 and the EPICAL-2L with the lateral cut applied is a measure for the leakage in the longitudinal direction: At  $E = 0.2\,\mathrm{GeV}$  almost no longitudinal leakage is present for both pixel hits and clusters. The longitudinal leakage increases with E to up to 10% for pixel hits and 15% for clusters at  $E = 1000\,\mathrm{GeV}$ . It follows that longitudinal leakage is primary-electron energy dependent, which is expected since the maximum  $t_{\mathrm{max}}$  of the longitudinal shower profile shifts towards higher layer numbers with increasing primary-electron energy ( $t_{\mathrm{max}} \propto \ln(E)$ ) as described in section 1.1. The comparison of  $\mu_{\mathrm{Hit,Clus}}$  between the EPICAL-2 and the EPICAL-2L without cuts applied yields the total leakage, which corresponds to the superposition of the leakage in the lateral and longitudinal directions. The total leakage increases with the primary-electron energy with a maximum leakage of approximately 19% for pixel hits and 27% for clusters at  $E = 1000\,\mathrm{GeV}$ .

Table 5.1 presents an overview of the parameter a and the measure  $\lambda_{\text{Hit,Clus}}$  of linearity for pixel hits and clusters in simulations of the EPICAL-2 and EPICAL-2L with different cut settings applied to the EPICAL-2L. For pixel hits, the EPICAL-2 and EPICAL-2L with the longitudinal cut, and both cuts applied have similar linearity. The elongated versions

| Parameterization with $\mu = a \cdot E$ |           |              |                       |                     |  |  |  |
|---|-----------|--------------|-----------------------|---------------------|--|--|--|
| Response Detector                       |           | Cut          | $a (\text{GeV}^{-1})$ | $\lambda (10^{-3})$ |  |  |  |
| observable                              |           |              |                       |                     |  |  |  |
| Pixel hits                              | EPICAL-2  | -            | $224 \pm 4$           | $101.1 \pm 0.8$     |  |  |  |
|   | EPICAL-2L | -            | $273 \pm 3$           | $31.8 \pm 0.2$      |  |  |  |
|   | EPICAL-2L | Both         | $224 \pm 4$           | $101.4 \pm 0.9$     |  |  |  |
|   | EPICAL-2L | Longitudinal | $244 \pm 4$           | $99.5 \pm 0.9$      |  |  |  |
|   | EPICAL-2L | Lateral      | $245 \pm 3$           | $40.3 \pm 0.3$      |  |  |  |
| Clusters                                | EPICAL-2  | -            | $28.7 \pm 1.4$        | $2383 \pm 7$        |  |  |  |
|   | EPICAL-2L | -            | $38.1 \pm 1.2$        | $1074 \pm 3$        |  |  |  |
|   | EPICAL-2L | Both         | $28.7 \pm 1.4$        | $2387 \pm 7$        |  |  |  |
|   | EPICAL-2L | Longitudinal | $32.3 \pm 1.4$        | $1970 \pm 6$        |  |  |  |
|   | EPICAL-2L | Lateral      | $33.0 \pm 1.2$        | $1440 \pm 4$        |  |  |  |

Table 5.1: Overview of the parameters a and the measure  $\lambda$  of linearity for pixel hits and clusters in simulations of the EPICAL-2 and EPICAL-2L with different cut settings applied to the EPICAL-2L.

of the EPICAL-2, which are the EPICAL-2L with the lateral cut applied and without cuts, feature better linearity for pixel hits than the unelongated versions. This is due to leakage in the longitudinal direction being primary-electron energy dependent and, therefore, harming the linearity of the EPICAL-2. For clusters, the EPICAL-2 and EPICAL-2L with both cuts applied feature the same linearity within statistical uncertainties. The linearity of the EPICAL-2L with the lateral cut applied is better than the linearity of the EPICAL-2, likely because the linearity harming effect of cluster merging is less influential in the enlarged versions of the EPICAL-2. The EPICAL-2L with the lateral cut applied and without cuts features better linearity than the unelongated versions of the EPICAL-2 because, same as for pixel hits, leakage in the longitudinal direction is reduced.

It follows that, in total, leakage decreases the detector response of the EPICAL-2 by between 8% and 19% for pixel hits and between 6% and 27% for clusters. It is also shown that leakage worsens the linearity: The measure of linearity increases by approximately a factor of 3 for pixel hits and 2.3 for clusters due to leakage.

#### 5.5.4 Energy resolution

Figure 5.16 shows the energy resolution  $\sigma_{\text{Hit}}/\mu_{\text{Hit}}$  for pixel hits (left) and energy resolution  $\sigma_{\text{Clus}}/\mu_{\text{Clus}}$  for clusters (right) as a function of the primary-electron energy E in simulations of the EPICAL-2 and EPICAL-2L with different cut settings applied to the EPICAL-2L. The energy resolution of the EPICAL-2 for both pixel hits and clusters improves with E for  $E < 200 \,\text{GeV}$ . For  $E > 200 \,\text{GeV}$ , the energy resolution worsens with E, which is likely caused by two effects: saturation and longitudinal leakage. As discussed in section 5.3, saturation has a negative effect on the energy resolution, which increases

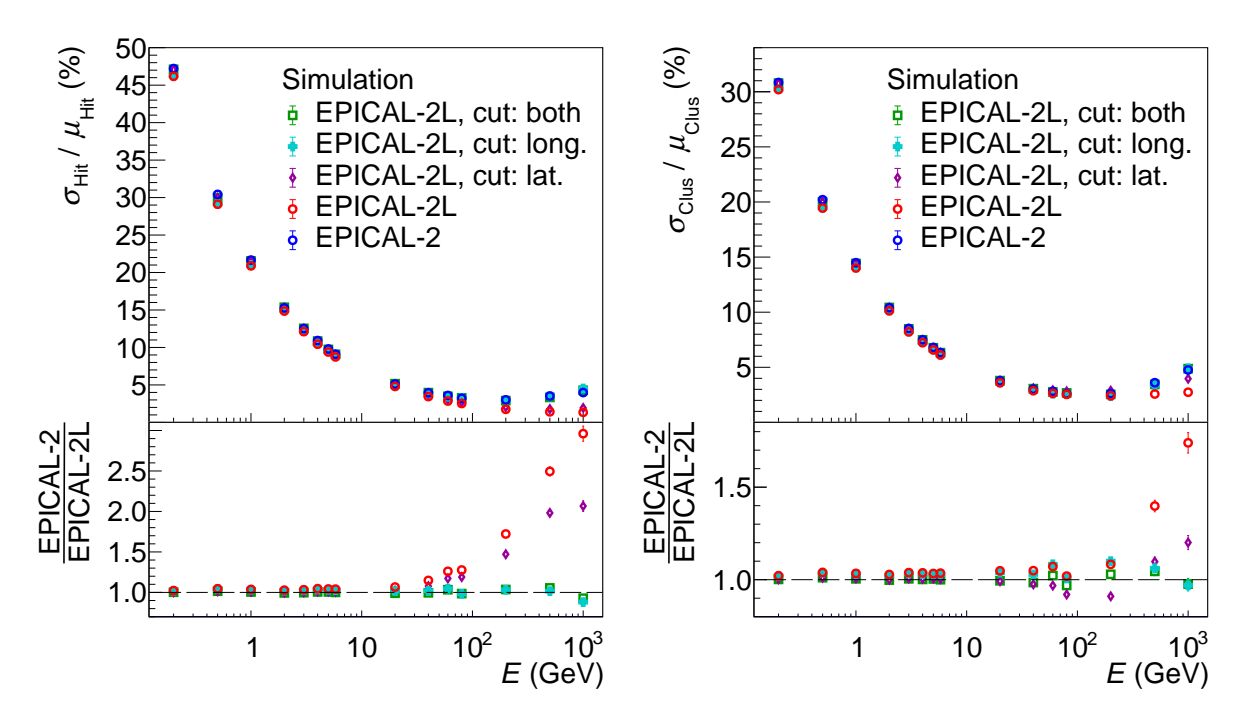


Figure 5.16: Energy resolution for pixel hits (left) and clusters (right) as a function of the primary-electron energy in simulations of the EPICAL-2 and EPICAL-2L with different cut settings applied to the EPICAL-2L.

with E. Therefore, at  $E>200\,\mathrm{GeV}$  saturation causes the energy resolution to worsen with increasing E. The amount of longitudinal leakage likely fluctuates between events, which has a negative effect on the energy resolution. Longitudinal leakage also increases with E since the longitudinal shower maximum shifts towards later layers. Therefore, longitudinal leakage likely also contributes to the worsening of the energy resolution with E for  $E>200\,\mathrm{GeV}$ .

The same behavior of the energy resolution is also observed in the EPICAL-2L simulations, except for pixel hits in the EPICAL-2L simulation with the lateral cut and without cuts. There, the energy resolution for  $E > 200 \,\text{GeV}$  saturates at approximately 1.5%.

The EPICAL-2L simulation with both cuts applied features the same energy resolution as the EPICAL-2 within statistical uncertainties for both pixel hits and clusters, proving that backscattering has no influence on the energy resolution of the EPICAL-2L.

For  $E \leq 40\,\mathrm{GeV}$ , the energy resolution for pixel hits and clusters is up to 5% worse for the EPICAL-2 compared to the EPICAL-2L with the longitudinal cut applied. For  $E > 40\,\mathrm{GeV}$ , this behavior cannot be observed due to larger statistical fluctuations of the energy resolution for  $E > 40\,\mathrm{GeV}$  compared to  $E \leq 40\,\mathrm{GeV}$ . For pixel hits, the EPICAL-2L with the lateral cut applied shows the same energy resolution as the EPICAL-2 within statistical uncertainties for  $E \leq 5.8\,\mathrm{GeV}$ . For  $E \geq 20\,\mathrm{GeV}$  the energy resolution for pixel hits of the EPICAL-2 compared to the EPICAL-2L with the lateral cut applied worsens with  $E = 1000\,\mathrm{GeV}$ . In the EPICAL-2, the energy resolution for pixel hits is up to 5% worse than in the EPICAL-2L without cuts

for  $E \leq 5.8\,\mathrm{GeV}$ . For  $E \geq 20\,\mathrm{GeV}$ , the energy resolution for pixel hits worsens with E by up to  $200\,\%$  in the EPICAL-2 compared to the EPICAL-2L without cuts. The improvement of the energy resolution for pixel hits in the elongated versions compared to the unelongated versions of the EPICAL-2 is likely caused by fluctuations in longitudinal leakage being suppressed.

For clusters, the energy resolution of the EPICAL-2L with the lateral cut applied and the EPICAL-2 are the same within statistical uncertainties for  $E \leq 20\,\mathrm{GeV}$ . However, for  $40\,\mathrm{GeV} \leq E \leq 200\,\mathrm{GeV}$ , the energy resolution for clusters of the EPICAL-2 compared to the EPICAL-2L with the lateral cut applied improves by up to  $10\,\%$  before worsening by up to  $15\,\%$  for  $E \geq 500\,\mathrm{GeV}$ . The improvement of the energy resolution for  $40\,\mathrm{GeV} \leq E \leq 200\,\mathrm{GeV}$  observed in the EPICAL-2 compared to the EPICAL-2L with the lateral cut applied has currently no explanation and requires further study. The energy resolution for clusters for  $E \leq 80\,\mathrm{GeV}$  is up to  $5\,\%$  worse in the EPICAL-2 compared to the EPICAL-2L without cuts. For  $E \geq 200\,\mathrm{GeV}$ , the energy resolution for clusters in the EPICAL-2 compared to the EPICAL-2L without cuts worsens with  $E \in 80\,\%$ . As for pixel hits, this likely results from the fluctuation of longitudinal leakage.

It follows that leakage harms the energy resolution of the EPICAL-2 at primary-electron energies up to  $80\,\text{GeV}$  by approximately  $5\,\%$  and for primary-electron energies higher than  $80\,\text{GeV}$  by up to  $200\,\%$  for pixel hits and  $80\,\%$  for clusters.

#### Leakage - summary

During this study, it is found that leakage affects the performance of the EPICAL-2: Leakage lowers the linearity of the EPICAL-2 for both pixel hits and clusters. The EPICAL-2 has approximately 5% worse energy resolution at low energies due to leakage. At high energies, this increases up to 200% for pixel hits and 80% for clusters.

A digital pixel calorimeter in a large-scale high-energy physics experiment would likely feature a larger design than the EPICAL-2, and, therefore, less leakage. Hence, even better performance can be anticipated in large-scale digital pixel calorimeters.

Back-bias voltage and radial cuts are shown to potentially increase the performance of the EPICAL-2. Therefore, by using back-bias voltage and radial cuts in a digital pixel calorimeter of a large-scale experiment, which would also feature low leakage, its performance could be optimized.

Radial cuts could also be applied to optimize the performance in future studies regarding the EPICAL-2. Additional studies of the EPICAL-2, such as analyzing its position resolution or exploring its ability for particle identification, are expected to reveal even more ways to enhance the performance of digital pixel calorimeters and deepen our understanding of this innovative technology.

### Summary and outlook

This thesis discusses multiple studies investigating the digital pixel calorimeter prototype EPICAL-2. An analysis of the EPICAL-2's performance in test-beam data and simulation considering back-bias voltage, radial cuts, and leakage is conducted.

This work presents the EPICAL-2's implementation in the Allpix<sup>2</sup> pixel detector simulation framework. In addition to the EPICAL-2, an enlarged version called EPICAL-2L is simulated.

Subsequently, the the necessary data analysis steps of clustering of pixel hits, corrections, event selection, as well as a run quality analysis are described.

This thesis presents the results of studies on the EPICAL-2's performance. The influence of back-bias voltage is analyzed by comparing test-beam data taken with a back-bias voltage of  $V_{\rm BB}=0\,\rm V$  and  $V_{\rm BB}=3\,\rm V$ . Back-bias voltage is found to decrease the linearity when studying pixel hits while slightly improving the linearity for clusters. Applying the back-bias voltage improves the energy resolution of the EPICAL-2 by up to 15 % for pixel hits and up to 17 % for clusters.

Two cuts with variable radius are defined to examine the effect of radial cuts on the performance, referred to as the outer radial cut and the inner radial cut. It is found that an outer radial cut has the potential to improve the linearity for pixel hits and the energy resolution for clusters at primary-electron energies above 60 GeV. An inner radial cut can enhance the linearity for both pixel hits and clusters.

The influence of leakage is studied by comparing the performance in the EPICAL-2 simulation to the EPICAL-2L simulation. Leakage in the lateral and longitudinal directions can be studied separately by applying multiple cuts to EPICAL-2L. Longitudinal leakage is found to worsen the linearity of the EPICAL-2 when studying pixel hits. For clusters, both lateral and longitudinal leakage decrease the linearity. Leakage was also found to worsen the energy resolution at primary-electron energies above  $80\,\text{GeV}$  by up to  $65\,\%$  for pixel hits and up to  $40\,\%$  for clusters. However, a digital pixel calorimeter in a large-scale high-energy physics experiment would probably be larger than the EPICAL-2, and show less leakage. Therefore, even better performance can be anticipated in digital pixel calorimeters of large-scale experiments.

Based on the analyses presented in this thesis, there are several further studies that could be conducted. The application of radial cuts is planned for future publications regarding the EPICAL-2. Therefore, the radial cuts studied in the scope of this thesis are to be

optimized for the best possible performance results. A further promising study could analyze the position resolution of the EPICAl-2 with the goal of improving its ability to distinguish between closely spaced electromagnetic showers. The measurement of electrons with the EPICAL-2 can be expanded to measurements of hadrons and muons with two primary objectives: to explore the possibility of particle identification with a digital pixel calorimeter and to obtain information about the development of hadronic showers. Digital pixel calorimeters are a promising new concept in high-energy physics and other fields of research. The results presented in this thesis highlight several methods in which the performance of a digital pixel calorimeter can be improved and, therefore, could contribute to their development. Additional research on the EPICAL-2 has the potential to enhance the understanding of digital pixel calorimeters and further improve their performance.

## Appendix

#### Appendix A: run quality analysis of the mean cluster size

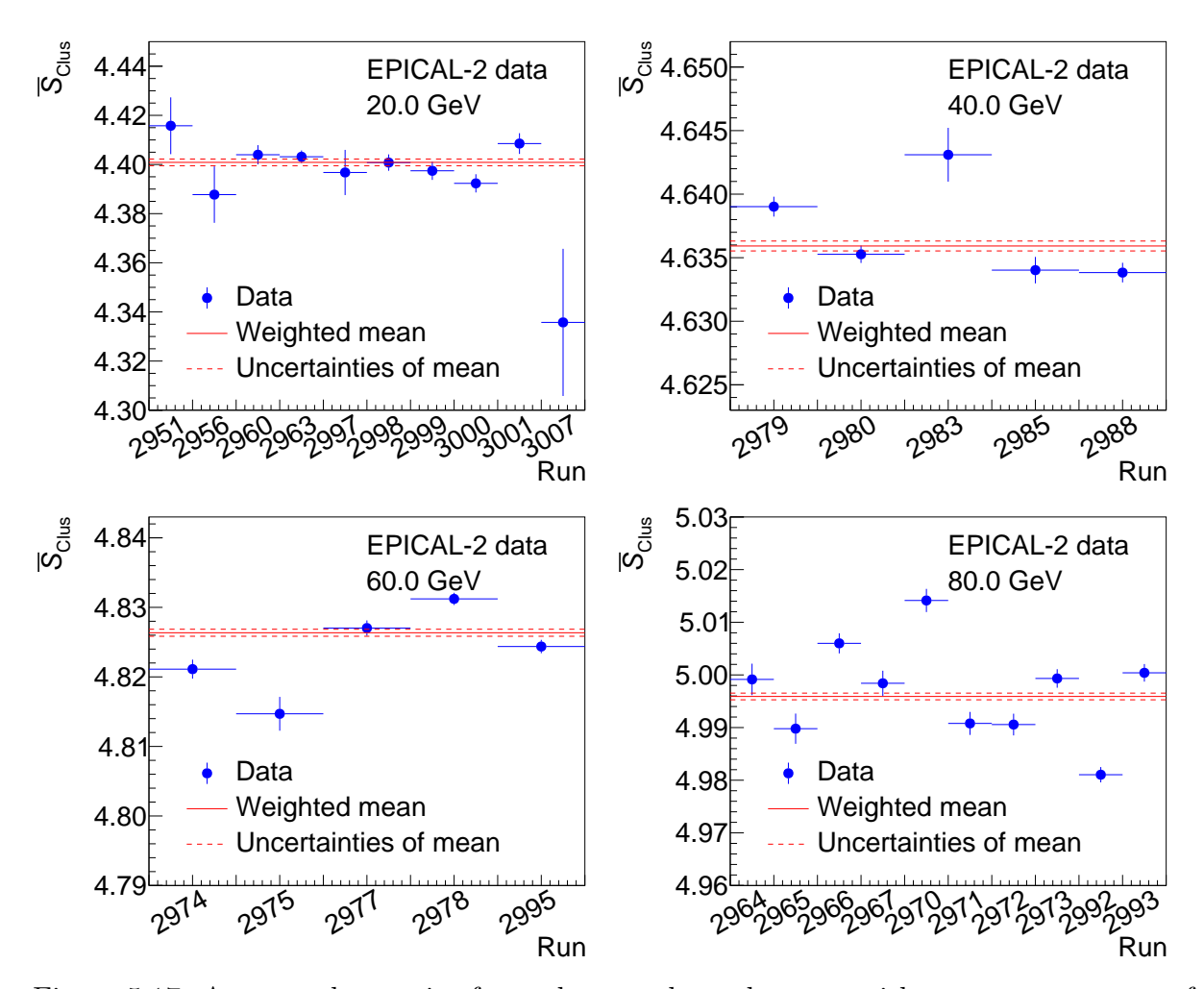


Figure 5.17: Average cluster size for each run, where electrons with an average energy of  $20\,\mathrm{GeV}$  (top left),  $40\,\mathrm{GeV}$  (top right),  $60\,\mathrm{GeV}$  (bottom left), and  $80\,\mathrm{GeV}$  (bottom right) have been measured.

# Appendix B: run quality analysis of the mean detector response for pixel hits

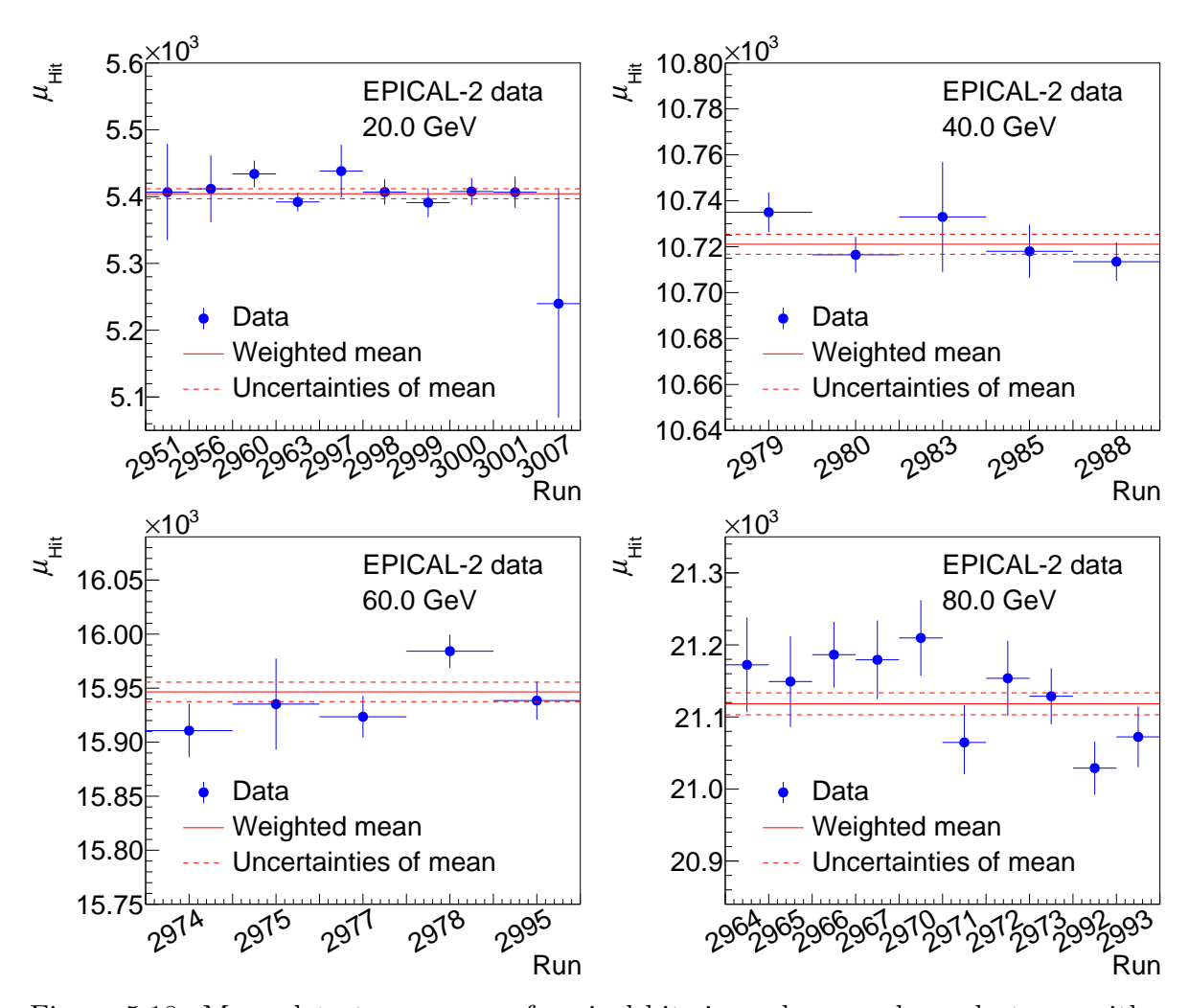


Figure 5.18: Mean detector response for pixel hits in each run, where electrons with an average energy of  $20\,\mathrm{GeV}$  (top left),  $40\,\mathrm{GeV}$  (top right),  $60\,\mathrm{GeV}$  (bottom left), and  $80\,\mathrm{GeV}$  (bottom right) have been measured.

## Appendix C: run quality analysis of the mean detector response for clusters

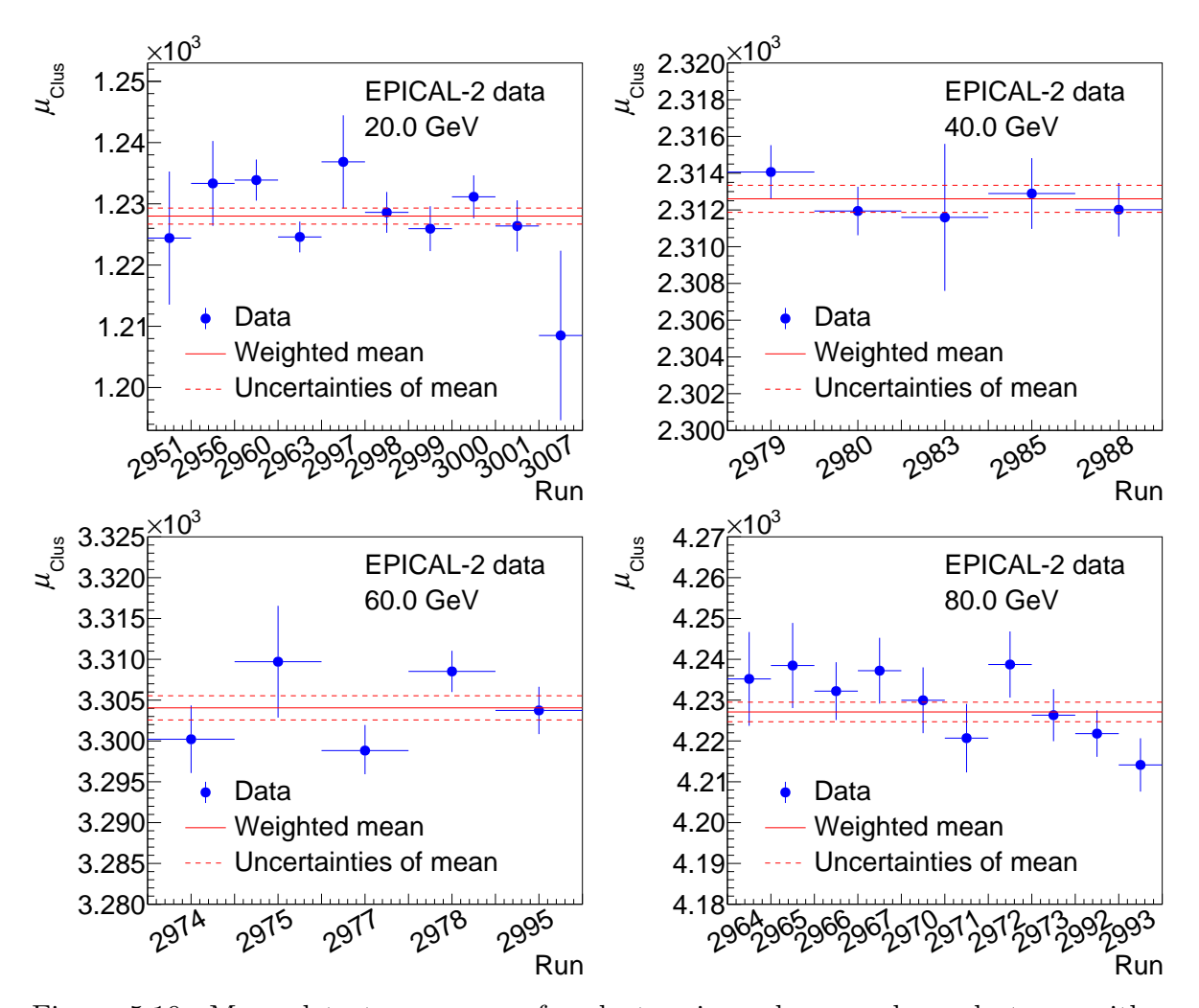


Figure 5.19: Mean detector response for clusters in each run, where electrons with an average energy of  $20\,\mathrm{GeV}$  (top left),  $40\,\mathrm{GeV}$  (top right),  $60\,\mathrm{GeV}$  (bottom left), and  $80\,\mathrm{GeV}$  (bottom right) have been measured.

# Appendix D: run quality analysis of the longitudinal shower maximum

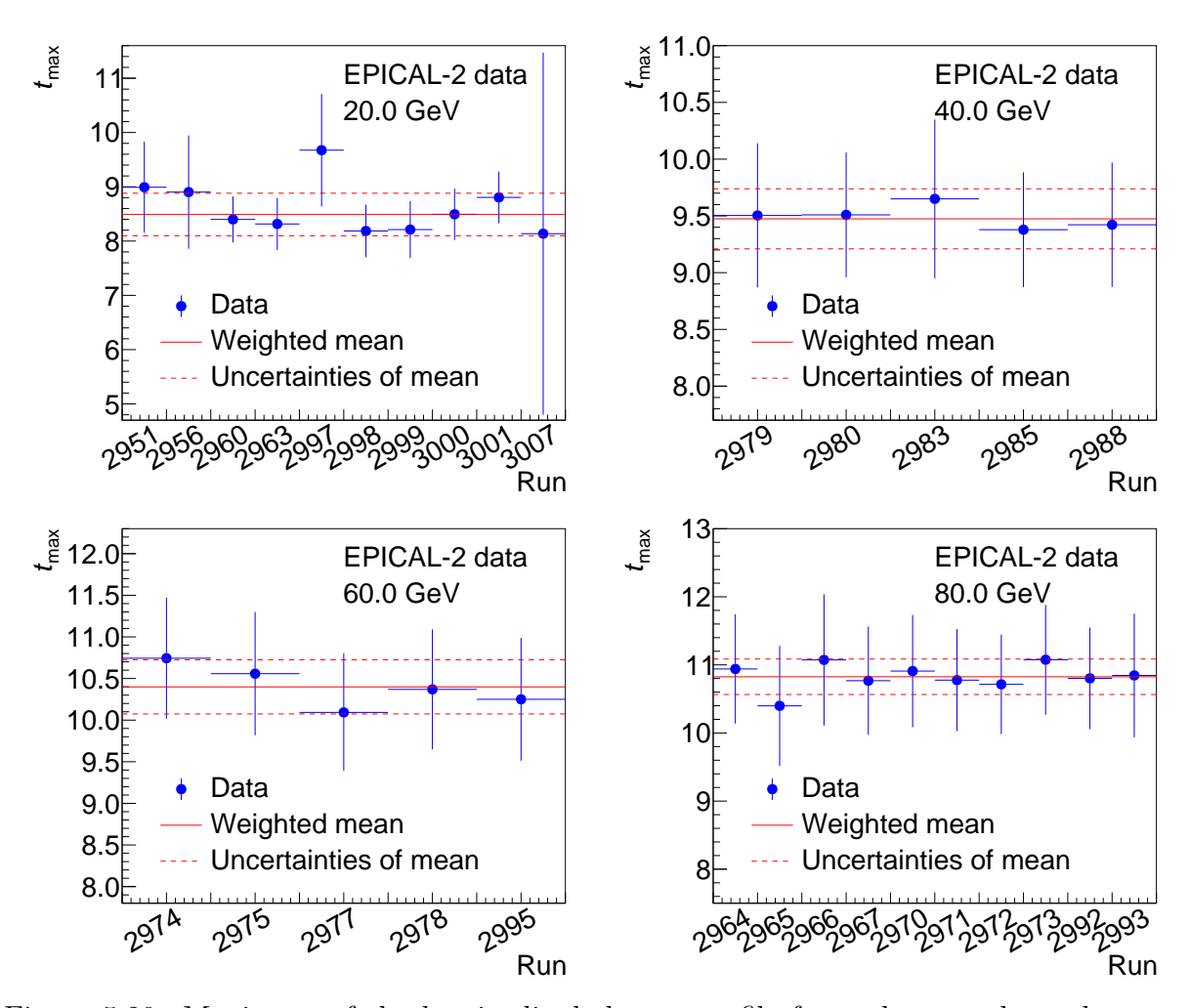


Figure 5.20: Maximum of the longitudinal shower profile for each run, where electrons with an average energy of  $20\,\mathrm{GeV}$  (top left),  $40\,\mathrm{GeV}$  (top right),  $60\,\mathrm{GeV}$  (bottom left), and  $80\,\mathrm{GeV}$  (bottom right) have been measured.

### **Bibliography**

- [Ago03] S. Agostinelli et. al. "Geant4—a simulation toolkit". In: Nuclear Instruments and Methods in Physics Research Section A: Accelerators, Spectrometers, Detectors and Associated Equipment 506.3 (July 2003), pp. 250–303. DOI: 10.1016/S0168-9002(03)01368-8.
- [Alm20] J. Alme et. al. "A High-Granularity Digital Tracking Calorimeter Optimized for Proton CT". In: Frontiers in Physics 8 (Oct. 2020). DOI: 10.3389/fphy. 2020.568243.
- [Alm23] J. Alme et. al. "Performance of the electromagnetic pixel calorimeter prototype EPICAL-2". In: *Journal of Instrumentation* 18.01 (Jan. 2023), P01038. DOI: 10.1088/1748-0221/18/01/P01038.
- [BR97] R. Brun and F. Rademakers. "ROOT An object oriented data analysis framework". In: Nuclear Instruments and Methods in Physics Research Section A: Accelerators, Spectrometers, Detectors and Associated Equipment 389.1 (Apr. 1997), pp. 81–86. DOI: 10.1016/S0168-9002(97)00048-X.
- [Cac08] M. Cacciari et. al. "The anti-kt jet clustering algorithm". In: Journal of High Energy Physics 2008.04 (Apr. 2008), p. 063. DOI: 10.1088/1126-6708/2008/ 04/063.
- [Die19] R. Diener et. al. "The DESY II test beam facility". In: Nuclear Instruments and Methods in Physics Research Section A: Accelerators, Spectrometers, Detectors and Associated Equipment 922 (Apr. 2019), pp. 265–286. DOI: 10.1016/j.nima.2018.11.133.
- [Est96] M. Ester et. al. "A density-based algorithm for discovering clusters in large spatial databases with noise". In: *Proceedings of 2nd International Conference on Knowledge Discovery and Data Mining* CONF-960830-TRN: 96:005928-0038 (Dec. 1996). URL: https://www.osti.gov/biblio/421283.
- [GR19] A. Gerbershagen and B. Rae. The H6 Secondary Beam Line of EHN1/SPS. 2019. URL: https://sba.web.cern.ch/sba/BeamsAndAreas/H6/H6\_presentation.html (visited on 12/20/2023).

- [gro23] Particle data group. Atomic and nuclear properties of materials: Tungsten (W). 2023. URL: https://pdg.lbl.gov/2011/AtomicNuclearProperties/HTML\_PAGES/074.html (visited on 10/27/2023).
- [Keu21] J. Keul. "Studie zur Detektorantwort und Datenqualität des ALICE-FoCal-Prototyps EPICAL-2". Bachelor thesis. Johann Wolfgang Goethe Universität Frankfurt am Main, 2021. URL: http://www.ikf.physik.uni-frankfurt.de/~buschin/thesis/Bachelorarbeit\_Johannes\_Keul.pdf.
- [Krö21] J. Kröger. "Characterisation of a High-Voltage Monolithic Active Pixel Sensor Prototype for Future Collider Detectors". PhD thesis. Universität Heidelberg, 2021. DOI: 10.11588/heidok.00030657.
- [KW20] H. Kolanoski and N. Wermes. *Particle Detectors*. Oxford university press, 2020.
- [Lee18] S. Lee et. al. "On the limits of the hadronic energy resolution of calorimeters". In: Nuclear Instruments and Methods in Physics Research Section A: Accelerators, Spectrometers, Detectors and Associated Equipment 882 (Feb. 2018), pp. 148–157. DOI: 10.1016/j.nima.2017.10.087.
- [Mag16] M. Mager. "ALPIDE, the Monolithic Active Pixel Sensor for the ALICE ITS upgrade". In: Nuclear Instruments and Methods in Physics Research Section A: Accelerators, Spectrometers, Detectors and Associated Equipment 824 (July 2016), pp. 434–438. DOI: 10.1016/j.nima.2015.09.057.
- [Pei18] T. Peitzmann et. al. "The FoCal prototype—an extremely fine-grained electromagnetic calorimeter using CMOS pixel sensors". In: *Journal of Instrumentation* 13.1 (Jan. 2018), P01014. DOI: 10.1088/1748-0221/13/01/P01014.
- [RK19] V. Raskina and F. Křížek. "Characterization of Highly Irradiated ALPIDE Silicon Sensors". In: *Universe* 5.4 (Apr. 2019). DOI: 10.3390/universe5040091.
- [RL01] P. Roldan and P. Lecoq. Quality control and preparation of the PWO crystals for the electromagnetic calorimeter of CMS. 2001. URL: https://www.researchgate.net/figure/Schematic-development-of-an-electromagnetic-shower\_fig9\_254468999 (visited on 01/08/2024).
- [Rog23a] T. S. Rogoschinski. "Performance of the Electromagnetic Pixel Calorimeter EPICAL-2 and Soft-Photon Background Studies in ALICE 3". PhD thesis. Johann Wolfgang Goethe Universität Frankfurt am Main, 2023.
- [Rog23b] T. S. Rogoschinski. Private communication. 2023.
- [ROO23] ROOT. Probability Density Functions (PDF). 2023. URL: https://root.cern.ch/doc/v608/group\_PdfFunc.html (visited on 10/31/2023).
- [Sch23] J. Schöngarth. Private communication. 2023.

- [Spa18] S. Spannagel et. al. "Allpix2: A modular simulation framework for silicon detectors". In: Nuclear Instruments and Methods in Physics Research Section A: Accelerators, Spectrometers, Detectors and Associated Equipment 901 (Sept. 2018), pp. 164–172. DOI: 10.1016/j.nima.2018.06.020.
- [Twi21] CERN Twiki. FoCalTestBeam2021Photos. 2021. URL: https://twiki.cern.ch/twiki/bin/view/ALICE/FoCalTestBeam2021Photos (visited on 02/21/2024).
- [Wik23a] Wikipedia. Diode. 2023. URL: https://de.wikipedia.org/wiki/Diode#: ~:text=Eine%20Diode%20ist%20ein%20elektronisches,eine%20Durchla% 20ssrichtung%20und%20eine%20Sperrrichtung.&text=Das%20Verhalten% 20wurde%201874%20von,auf%20Halbleitern%20(Bleisulfid)%20entdeckt. (visited on 01/17/2024).
- [Wik23b] Wikipedia. Gamma distribution. 2023. URL: https://en.wikipedia.org/wiki/Gamma\_distribution (visited on 10/31/2023).
- [Wik23c] Wikipedia. p-n junction. 2023. URL: https://en.wikipedia.org/wiki/P-n\_junction (visited on 06/30/2023).
- [Wik24] Wikipedia. Coefficient of determination. 2024. URL: https://en.wikipedia.org/wiki/Coefficient\_of\_determination (visited on 02/16/2024).
- [Win18] i. Wingerter-Seez. "Particle Physics Instrumentation". In: CERN Yellow Reports: School Proceedings 2 (Apr. 2018), pp. 295–314. DOI: 10.23730/CYRSP-2017-002.295.
- [Wor22] R. L. Workman et. al. Particle Physics Booklet. Particle data group, 2022.
- [Yua21] S. Yuan et. al. The charge sensitivity calibration of the upgraded ALICE Inner Tracking System. 2021. URL: https://cds.cern.ch/record/2790475?ln=de (visited on 01/17/2024).

## Acknowledgements

First of all, I would like to express my gratitude to Prof. Dr. Henner Büsching for giving me the opportunity to work on this thesis in his research group and for his valuable guidance throughout my research.

Furthermore, I would like to thank Prof. Dr. Christoph Blume for making the second review of this thesis.

Special thanks go to Tim Rogoschinski for expertly guiding my work and providing useful feedback on my thesis.

Additionally, I would like to thank Prof. Dr. Thomas Peitzmann and Prof. Dr. Nigel Watson, who, with their expert knowledge, gave great suggestions for my work.

During my studies, my colleagues from the high-energy physics group in Frankfurt created a pleasant work environment, for which I am thankful. I would like to express my gratitude to Joshua König, Marvin Hemmer, Mario Krüger, Jan Schöngarth, and Maria Calmon Behling for affording valuable feedback on my thesis.

Last but not least, I want to express my appreciation to my family for their financial and moral support throughout my physics studies and during the work on my master thesis.

## Eigenständigkeitserklärung

Erklärung nach §39 (15) Prüfungsordnung 2020 für den BAMA-Studiengang Physik

Hiermit erkläre ich, dass ich die Arbeit selbstständig und ohne Benutzung anderer als der angegebenen Quellen und Hilfsmittel verfasst habe. Alle Stellen der Arbeit, die wörtlich oder sinngemäß aus Veröffentlichungen oder aus anderen fremden Texten entnommen wurden, sind von mir als solche kenntlich gemacht worden. Ferner erkläre ich, dass die Arbeit nicht - auch nicht auszugsweise - für eine andere Prüfung verwendet wurde.

| $\bigcirc$ rt | Datum  | Frankfurt am Mair | den 04 03 2024     | Unterschrift: |  |
|---------------|--------|-------------------|--------------------|---------------|--|
| $o_1$         | Davam. | Transfer and Man  | i, ucii 04.00.2024 | CHICESCHIII.  |  |